Seismic structure of the St. Paul Fracture Zone and Late Cretaceous to Mid Eocene oceanic crust in the equatorial Atlantic Ocean near 18°W

Kevin Growe[1,1,1], Ingo Grevemeyer[1,1,1], Satish Chandra Singh[2,2,2], Milena Marjanovic[2,2,2], Emma PM Gregory[2,2,2], Cord Papenberg[3,3,3], Venkata Abhishikth Vaddineni[2,2,2], Laura Gómez de la Peña[4,4,4], and Zhikai Wang[2,2,2]

[1]GEOMAR Helmholtz Centre for Ocean Research Kiel
[2]Institut De Physique Du Globe De Paris
[3]Geomar, Kiel, Germany
[4]GEOMAR Helmholtz Centre of Ocean Research

November 30, 2022

Abstract

Plate tectonics characterize transform faults as conservative plate boundaries where the lithosphere is neither created nor destroyed. In the Atlantic, both transform faults and their inactive traces, fracture zones, are interpreted to be structurally heterogeneous, representing thin, intensely fractured, and hydrothermally altered basaltic crust overlying serpentinized mantle. This view, however, has recently been challenged. Instead, transform zone crust might be magmatically augmented at ridge-transform intersections before becoming a fracture zone. Here, we present constraints on the structure of oceanic crust from seismic refraction and wide-angle data obtained along and across the St. Paul fracture zone near 18°W in the equatorial Atlantic Ocean. Most notably, both crust along the fracture zone and away from it shows an almost uniform thickness of 5-6 km, closely resembling normal oceanic crust. Further, a well-defined upper mantle refraction branch supports a normal mantle velocity of 8 km/s along the fracture zone valley. Therefore, the St. Paul fracture zone reflects magmatically accreted crust instead of the anomalous hydrated lithosphere. Little variation in crustal thickness and velocity structure along a 200 km long section across the fracture zone suggests that distance to a transform fault had negligible impact on crustal accretion. Alternatively, it could also indicate that a second phase of magmatic accretion at the proximal ridge-transform intersection overprinted features of starved magma supply occurring along transform faults.

1 **Seismic structure of the St. Paul Fracture Zone and Late Cretaceous to Mid**
2 **Eocene oceanic crust in the equatorial Atlantic Ocean near 18°W**
3

4 Kevin Growe[1,2] , Ingo Grevemeyer[1], Satish C. Singh[2], Milena Marjanović[2], Emma P. M. Gregory[2], Cord Papenberg[1],
5 Venkata Vaddineni[2], Laura Gómez de la Peña[1], and Zhikai Wang[2]
6

7 [1]GEOMAR Helmholz Centre for Ocean Research Kiel

8 [2]Université de Paris, Institut de Physique du Globe de Paris; CNRS, Paris, France

9

10 Corresponding author: Kevin Growe (kevin.growe93@web.de)

11 **Key Points:**

12 • Seismic structure along the St. Paul fracture zone reflects magmatically accreted oceanic
13 crust

14 • Oceanic crust across St. Paul shows only small thickness variations, lacking evidence for
15 regional crustal thinning near fracture zones

16 • Magmatic nature of crust supports a mechanism where transform crust is augmented
17 before being turned into a fracture zone

18 **Abstract**

19 Plate tectonics characterize transform faults as conservative plate boundaries where the
20 lithosphere is neither created nor destroyed. In the Atlantic, both transform faults and their
21 inactive traces, fracture zones, are interpreted to be structurally heterogeneous, representing thin,
22 intensely fractured, and hydrothermally altered basaltic crust overlying serpentinized mantle.
23 This view, however, has recently been challenged. Instead, transform zone crust might be
24 magmatically augmented at ridge-transform intersections before becoming a fracture zone. Here,
25 we present constraints on the structure of oceanic crust from seismic refraction and wide-angle
26 data obtained along and across the St. Paul fracture zone near 18°W in the equatorial Atlantic
27 Ocean. Most notably, both crust along the fracture zone and away from it shows an almost
28 uniform thickness of 5-6 km, closely resembling normal oceanic crust. Further, a well-defined
29 upper mantle refraction branch supports a normal mantle velocity of 8 km/s along the fracture
30 zone valley. Therefore, the St. Paul fracture zone reflects magmatically accreted crust instead of
31 the anomalous hydrated lithosphere. Little variation in crustal thickness and velocity structure
32 along a 200 km long section across the fracture zone suggests that distance to a transform fault
33 had negligible impact on crustal accretion. Alternatively, it could also indicate that a second
34 phase of magmatic accretion at the proximal ridge-transform intersection overprinted features of
35 starved magma supply occurring along the St. Paul transform fault.

36

37 **Plain Language Summary**

38 Transform faults represent plate boundaries where two plates move past each other without
39 producing new or destroying the existing lithosphere. Most of the Atlantic transform faults and
40 their inactive traces, fracture zones, were characterized by fractured and altered, thin-crust
41 overlying serpentinized mantle rocks. However, recent results reveal that the crust beneath
42 fracture zones may not be as thin and challenge the standard view, introducing a mechanism of
43 secondary magma supply at the intersection between the ridge axis and transform fault. Here, we
44 present results from seismic experiments at the St. Paul fracture zone near 18°W in the
45 equatorial Atlantic. Our results suggest that the subsurface of the St. Paul fracture zone is
46 represented by a nearly uniform crustal thickness of 5-6 km and an upper mantle with a velocity
47 of 8 km/s. Both observations argue for a crust of magmatic origin and the absence of strong
48 alteration of the upper mantle. Collectively, constant crustal thickness and little variation in
49 seismic velocities along the profile crossing the fracture zone suggest that the crustal formation
50 process does not vary as a function of distance from the fracture zone. Alternatively, secondary
51 magma supply at the ridge-transform intersection could overprint any anomalous formation
52 conditions.

53 **1 Introduction**

54 　　　Plate tectonics separates Earth' surface into rigid plates (McKenzie, 1967; Morgan,
55 1968), and deformation or relative motion between plates reveals three different types of oceanic
56 plate boundaries: (i) constructive plate boundaries at mid-ocean ridges (MOR) where new
57 seafloor is created, (ii) destructive plate boundaries at subduction zones where the oceanic
58 lithosphere is transferred into the mantle and recycled, and (iii) conservative plate boundaries
59 and hence transform faults (TF) where the lithosphere is neither created nor destroyed as plates

60 move past each other (Morgan, 1968). In ocean basins, transform faults offset MOR by tens to
61 several hundreds of kilometers (Searle et al., 1994), splitting them into first-order spreading
62 segments (Macdonald et al., 1988). They are long-lived features, and in the equatorial Atlantic,
63 the largest transform faults, namely Chain, Romanche, and St. Paul, can be followed along their
64 inactive traces, called fracture zones (FZ), towards the margins of the Atlantic Ocean (Wilson,
65 1965). Fracture zones are prominent linear features on the ocean floor that were identified and
66 named before plate tectonics linked them to seafloor spreading (Menard, 1955; 1967).

67   Oceanic crust formed along a spreading ridge is generally believed to remain largely
68 unchanged as it is moved by plate motion away from the active plate boundary. Its structure can
69 be best described with respect to a layered structure, where the crust is divided into two main
70 distinct lithologic layers exhibiting different seismic properties (e.g., Raitt, 1963). The upper
71 crust (layer 2) consists of pillow basalts overlaying a basaltic sheeted dike complex (e.g., Vine &
72 Moores, 1972) and reveals high velocity gradients of 1-2 s^{-1} and velocities from 3-5 km/s just
73 below the basement to 6.3-6.8 km/s at a depth of 1-2 km below the basement (e.g., Grevemeyer
74 et al., 2018; White et al. 1992; Whitmarsh, 1978). The mid- and lower crust (layer 3) instead
75 consist of plutonic, mostly gabbroic, rocks and has low velocity gradients of 0.1-0.2 s^{-1} and
76 velocities from ~6.6 km/s at the top of the layer to 7.2 km/s at its base (e.g., Carlson & Miller,
77 2004; Vine & Moores, 1972). The thickness of layer 3 is much more variable than the thickness
78 of layer 2 such that variations in crustal thickness in several studies are related to thickness
79 variations of layer 3 (e.g., Mutter & Mutter, 1993).

80   It has long been recognized that oceanic crust varies along spreading segments, with the
81 thickest crust formed at a segment center away from major ridge crest discontinuities and the
82 thinnest crust at segment ends or transform faults (e.g., Macdonald et al., 1988; Tolstoy et al.,
83 1993). Along fast-spreading ridges, thickness variations are generally less than one kilometer
84 (e.g., Canales et al., 2003). At slow- and ultraslow-spreading ridges, crust of ~7-9 km thickness
85 may occur at segment centers and decrease to only 4-6 km at segment ends (e.g., Canales et al.,
86 2000; Dannowski et al., 2011; Grevemeyer et al., 2018; Niu et al., 2015). These along-axis
87 thickness variations can be best explained by focused mantle upwelling at segment centers and
88 lateral melt transport, suggesting that mantle upwelling is intrinsically plume-like (3-D) beneath
89 a slow-spreading ridge but more sheet-like (2-D) beneath a fast-spreading ridge (Bell & Buck,
90 1992; Lin & Morgan, 1992).

91   Along-axis changes in oceanic crustal architecture suggest that the end of spreading
92 segments and hence transform faults represent the magmatically starved end-member of the
93 oceanic crust (e.g., Detrick et al., 1993; White et al., 1984) where the principal orientation of
94 tectonic stresses rotate by tens of degrees over a very short distance (Morgan & Parmentier,
95 1984), changing from normal faulting at the spreading axis to strike-slip along the transform
96 (e.g., Sykes, 1967). In the Pacific, the crustal structure at transform faults reveals a drop of
97 seismic P-wave velocity in the active strike-slip fault, indicating the presence of high porosities
98 along the tectonically active fault trace (Roland et al., 2012). However, it shows little evidence
99 for reduced melt supply as crustal thickness across the fast-slipping transforms indicates only a
100 small reduction, which is in the order of several hundreds of meters (Roland et al., 2012). In
101 contrast, some transform faults in the Atlantic exhibit thin crust ~4-5 km thick (e.g., Ambos &
102 Hussong, 1986; Detrick et al., 1982; Whitmarsh & Calvert, 1986) along transform valleys which
103 is 1-2 km thinner when compared to the neighboring normal oceanic crust (e.g., Grevemeyer et
104 al., 2018; van Avendonk et al., 2017; White et al., 1992). The above observations led to the

105 conclusion that lithosphere along transform faults and fracture zones might be intensely
106 fractured, faulted, and composed of hydrothermally altered basaltic and gabbroic rocks overlying
107 ultramafics that might be extensively serpentinized (Detrick et al., 1993; White et al., 1984).

108   A recent study suggests that the crust beneath the Chain fracture zone in the equatorial
109 Atlantic region has a nearly normal crustal thickness (Marjanović et al., 2020). This observation
110 has been independently supported using global bathymetric observations and numerical
111 simulation on transform fault tectonics (Grevemeyer et al., 2021) suggesting that crust is (i)
112 initially magmatically emplaced near a ridge-transform intersection (RTI), (ii) experiences
113 tectonic deformation, and extension while being moved along the transform fault and (iii) finally
114 it is augmented by the second stage of magmatism as it passes the opposing RTI. If correct, the
115 formation of crust at transform faults should occur in three distinctive phases, suggesting that the
116 structure of crust present below the valley of an active transform fault should differ profoundly
117 from crust found along its fracture zones.

118   Here, we use two seismic profiles shot in 2017 and 2018 with modern seismic refraction
119 and wide-angle equipment surveying the St. Paul fracture zone near 18°W in the equatorial
120 Atlantic region (Fig. 1). The seismic data are well-suited for seismic tomography to study the
121 structure along a 140 km-long roughly west-east running profile in the valley of the St. Paul
122 fracture zone and along a 300 km-long north-south trending profile crossing the fracture zone
123 and sampling the adjacent mature oceanic crust. The north-south striking profile is located
124 roughly 850 km east of the eastern RTI of the St. Paul TF, extends from ~0.8°N to ~4°N, crosses
125 the FZ at ~18°W/2°N and samples crustal ages of 70 Ma on the northern and ~45 Ma on the
126 southern plate segment. Itruns parallel to the trend of the Mid-Atlantic Ridge (MAR) and hence
127 should reveal features governed by changes in melt supply towards a transform fault and lateral
128 melt transport, which is expected to diminish when approaching transform faults (e.g., Lin et al.,
129 1990; Macdonald et al., 1988; White et al., 1984). The crustal and upper mantle velocity
130 structures are derived from a joint tomographic inversion of first arrival travel times and wide-
131 angle reflections from the crust-mantle boundary, providing high-resolution constraints on the
132 seismic velocity structure and crustal thickness along the fracture zone and the dependence of
133 crustal accretion as a function of distance to a fracture zone.

134 **2 Regional Setting of the St. Paul Fracture Zone and Study Area**

135   2.1 Regional Setting of the St.Paul Fracture Zone

136   The St. Paul fracture zone (SPFZ) is one of the major east-west striking equatorial
137 fracture zones of the Atlantic Ocean. At the active MAR, the St. Paul, Romanche and Chain
138 transform faults offset the ridge crest by ~1800 km, causing an age variation of 90 Myr over 400
139 km north-south distance (Müller et al., 2008). The active domain of the St. Paul transform fault
140 system offsets the MAR by ~600 km and can be subdivided into four strike-slip faults;
141 sandwiched in between are three short intra-transform spreading segments (Fig. 1a). Maia et al.
142 (2016) studied the northern TF segment and found a complex tectonic regime revealing a
143 transpressional zone exhuming deformed and serpentinized mantle rocks, triggered as a response
144 to a change of relative plate motion ∼11 Myr ago. The fossil trace of the transform fault, the
145 fracture zone can be followed using the vertical gravity gradient (Sandwell et al., 2014) across
146 the entire Atlantic Ocean, from the continental shore of Liberia in the east to the Amazonas Basin
147 in the west, resulting in a total length of ∼3000 km. For ages greater than 20 Myr (Mueller et al.,
148 2008) away from both RTI, the bathymetry data indicate the presence of only two fracture zone
149 valleys, suggesting that today's complex transform-fault-system developed roughly 20 Myr ago.
150 Using 2-D ultra-deep multichannel seismic reflection data, Mehouachi and Singh (2018) imaged
151 the lithosphere-asthenosphere boundary along a north-south striking line and revealed a
152 southward thinning of the lithosphere, mimicking the age contrast across the system of fracture
153 zones at ~18°W.

154

155   2.2 Study Area

156   Within our study area, ~800 km east from the active St. Paul transform fault system (Fig.
157 1a), the ~10 km wide northernmost St. Paul fracture zone valley (SPFZ-1) separates ~70 Ma
158 oceanic lithosphere in the north from 40-50 Ma lithosphere in the south (Müller et al., 2008).
159 Here, the valley is covered by sediments up to a kilometer thick, creating a smooth surface but
160 still forming a 200-300 m deep valley with respect to the surrounding ocean floor (Fig. 1c). Its
161 younger southern edge is flanked by significantly rougher bathymetry, revealing ridge-like
162 features aligned mostly perpendicular to the FZ that we interpret as overshooting ridges, as
163 observed near RTIs globally (e.g., Grevemeyer et al., 2021; Lonsdale, 1986; Marjanović et al.,
164 2020). The older northern flank of the FZ can be subdivided into two distinct domains (Fig 1c).
165 The north-western area to the west of the intersection of seismic profiles shows ridge- and dome-
166 like features mostly parallel to the fracture zone. In contrast, the north-eastern domain reveals a
167 rather smooth seafloor, except for a seamount-like structure located at the eastern limit of the
168 west-east striking seismic line LI-02.

169   The north-south striking seismic line IS-01 ran over a smooth seafloor of an almost
170   constant depth to the north of St. Paul, except for two ridge-like features near OBS 1 and OBS 5
171   (Fig 1b). The bathymetry to the south of SPFZ-1 is significantly rougher, showing east-west
172   trending ridge-like features separating SPFZ-1 from a second, parallel fracture zone valley in the
173   south (SPFZ-2) near OBS13. SPFZ-2 is related to the southernmost TF segment of the modern
174   active TF system of St. Paul (Fig. 1a). The seismic line is limited in the south by another FZ
175   parallel ridge south of SPFZ-2 and a deep basin just north of the Romanche TF (Fig. 1a, b).

176

178
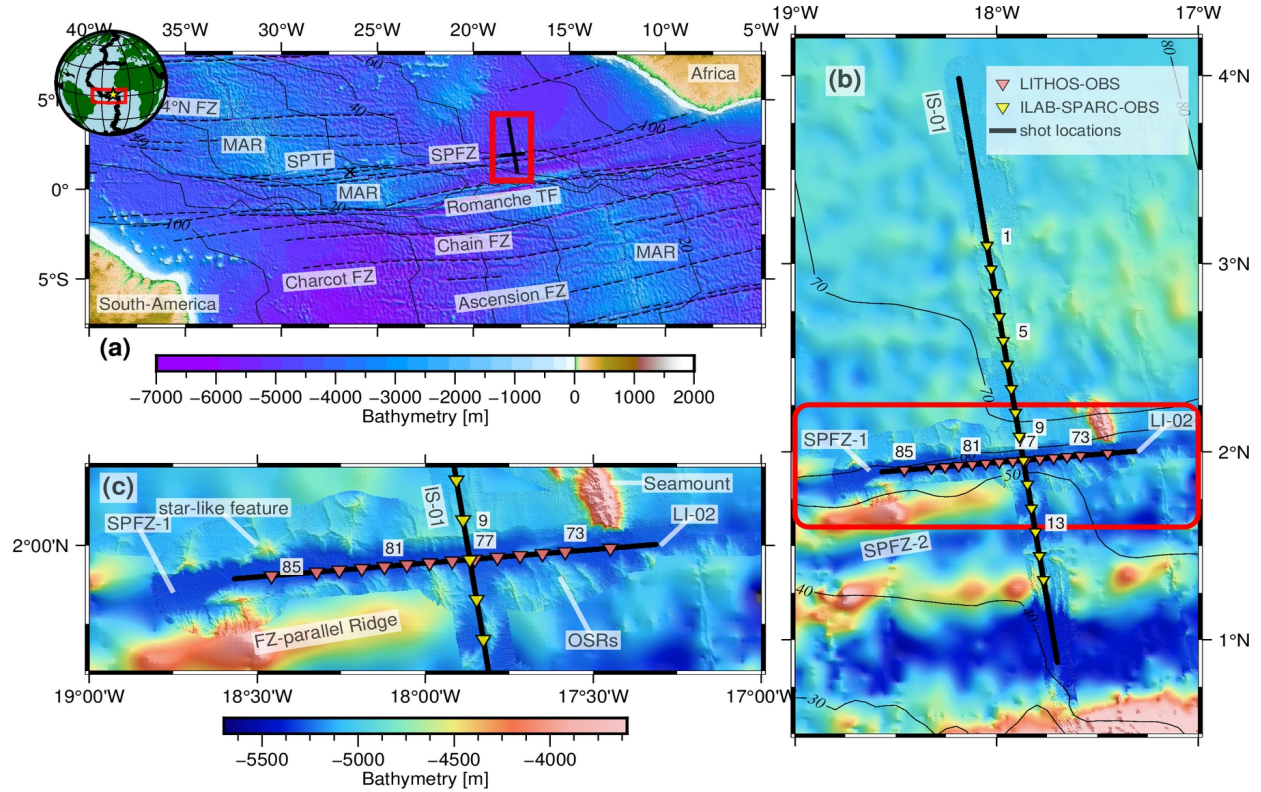
179 **Figure 1**: Regional and survey map in the equatorial Atlantic Ocean. **(a)** Bathymetric map showing
180 survey location and tectonic setting around the SPFZ. The bathymetry is from TOPEX satellite gravity
181 data (Sandwell et al., 2014). Thin labelled black lines denote crustal age after Müller et al. (2008) with an
182 interval of 20 Myrs. Dashed lines denote fracture zones mapped by Matthews et al. (2011). Plate
183 boundaries on inset globe are from Bird (2003) and yellow star indicates the survey location. The thick
184 black lines represent the two survey lines (LI-02 and IS-01). Red box marks the survey area shown in (b).
185 The black cross denotes the eastern RTI of the SPFZ. The main regional tectonic features are labeled (see
186 definition of acronyms at the end of the caption). **(b)** Survey area showing shot and OBS locations for
187 both seismic lines (note legend). Every fourth OBS is labeled. The bathymetry is combined with TOPEX
188 data and acquired shipboard high resolution multibeam echo-sounder data (LITHOS: 100x100 m; ILAB-
189 SPARC: 50x50 m). The crustal ages are indicated by thin black contours and labelled with an interval of
190 10 Myrs. The red box depicts the closeup map shown in (c). **(c)** Closeup of bathymetric map of the
191 surveyed transect of the SPFZ-1 using the same color scale as in (b). Prominent bathymetric features are
192 labeled. Remaining features are displayed as in (b). Acronyms: MAR - Mid-Atlantic Ridge, TF -
193 Transform Fault, SPTF - St.Paul Transform Fault, SPFZ - St.Paul Fracture Zone OSRs - Overshooting
194 Ridges.

195

3 Data Acquisition and Processing

197   In the framework of the Trans-Atlantic-iLAB and LITHOS projects, several OBS based
198 seismic refraction lines, as well as multichannel seismic reflection lines, were acquired during
199 three cruises in the central equatorial Atlantic Ocean from 2015-2018. In this study, we present
200 the results from the two seismic refraction and wide-angle profiles along and across the St. Paul
201 fracture zone, at 2°N/18° W, hereafter named as profiles LI-02 and IS-01 (see Supplementary
202 Figs S1 and S2). Profile IS-01 is coincident with the seismic reflection profile of Mehouachi and
203 Singh (2018).

204 3.1 Acquisition LI-02

205   Profile LI-02 was acquired during the LITHOS cruise onboard the German *R/V Maria S.*
206 *Merian* in December 2017, where 12 four-component ocean bottom seismometers (OBS) and
207 two one-component ocean bottom hydrophones (OBH) with a spacing of 7.5 - 15 km were
208 deployed within the fracture zone valley (Fig. 1c). For simplicity, we will refer to all receiver
209 types as OBS. A total of 875 shots were fired at 210 bars on a 142 km long east-west orientated
210 transect. A shot time interval of 90 s with a vessel speed of ∼3.5 knots led to an average spatial
211 shot interval of ∼160 m. The two airgun sub-arrays each consisted of six G-guns, provided a
212 total volume of 86 l, and were towed at a depth of 7.5 m. The OBS data were sampled at 250 Hz.
213 All instruments recorded good quality data containing crustal (Pg) and mantle (Pn) refraction
214 arrivals up to offsets of 90 km, and all but two OBS, OBS 82 and 85, also recorded wide-angle
215 reflections from the Moho (PmP) (Fig. 2). Pg and PmP arrivals could be picked mostly between
216 5-25 and 15-30 km offsets, respectively. Pn arrivals could be picked mostly up 60 km offset and
217 even up to 80-90 km for some record sections (see all record sections in Figures S1a-n in the
218 supplementary material). Since no streamer data were acquired along the profile, the basement
219 depth and the sediment structures were obtained by mirror imaging (Supplementary material Fig.
220 S3) of the hydrophone component of OBS receiver gathers (e.g., Grion et al., 2007).

221 3.2 Acquisition IS-01

222   Line IS-01 is the northernmost part of the north-south profile acquired during the ILAB-
223 SPARC cruise aboard the French *R/V Pourquoi Pas?* in 2018. The profile is in total 850 km-long,
224 crossing farther south the Romanche transform fault (~0°N) (Gregory et al., 2021) and the Chain
225 fracture zone (~2°S) (Marjanović et al., 2020). Here, we use the data from the northernmost 350
226 km of the line containing 15 four-component OBS with an average instrument spacing of 14.2
227 km. The OBS data were sampled at 250 Hz. Most OBS receiver gathers provide good quality
228 data where both refraction and wide-angle reflection arrivals can be identified with confidence
229 (Fig. 2). Pg and PmP arrivals were picked mostly between 5-25 and 15-35 km offset,
230 respectively. Pn arrivels could be picked mostly up 50 km offset (Fig. S2). A summary of the
231 acquisition parameters for the two refraction profiles is provided in Table S1.

232   A total of 1168 shots were fired at a pressure of 140 bars and at a source interval of 300
233 m. The larger shot interval was chosen to minimize the noise level in the water column for later
234 arrivals. Two sub-arrays containing eight G-guns each provided a total volume of 82 liters and
235 were towed at a depth of 10 m. Real-time source monitoring provided excellent conditions for a
236 well-tuned signal which is critical for such an experiment.

237   Simultaneously, a 6 km-long streamer containing 960 hydrophones, grouped with a
238 spacing of 6.25 m, was towed at a depth of 12 m to acquire multi-channel seismic (MCS) data
239 along the line. A basic processing sequence included bandpass filtering from 5-125 Hz, normal-
240 move out (NMO) based stacking, and migration with a constant velocity of 1.5 km/s, which
241 provided seismic images of the sediment cover and the depth of the igneous basement
242 (Supplementary material Fig. S4). Due to the large shot interval and consequently low fold, the
243 quality of the seismic image is poor below the basement. The MCS data were therefore mainly
244 used to constrain the depth and shape of the basement below the sediment cover. Thus, both
245 seafloor and basement were picked on the post-stack time-migrated section and converted to
246 depth for the tomographic travel time inversion using the acoustic velocity of water and a
247 constant velocity for sediments of 1.86 km/s derived as a mean from the semblance analysis of
248 the ultra-long streamer data (Marjanović et al., 2020). Additional constrains on the sedimentary
249 blanket along IS-01 are available for the coincident seismic profile of Mehouachi and Singh
250 (2018).

251 3.3 OBS Processing

252   The OBS data were corrected for the internal clock drift and were relocated using the
253   symmetry of the direct wave and a least-squares method (e.g., Creager & Dorman, 1982). The
254   acoustic sound speed profile of water was obtained by onboard Expendable Bathythermograph
255   (XBT) and World Ocean Circulation Experiment (WOCE) Conductivity/Temperature/Depth
256   (CTD) data. The OBS depth was further corrected to match the constrained seafloor depth and a
257   corresponding time shift was applied to the travel times. In this study, we only use the pressure
258   components of the OBSs. The processing of the OBS data was carried out with Seismic Unix
259   (Cohen & Stockwell, 2010) using the same sequence and parameters for both lines. A
260   Butterworth-bandpass filter from 4-20 Hz was applied to the OBS gathers to filter low and high
261   frequency noise. Moreover, a predictive deconvolution was applied to suppress some energy of
262   the bubble reverberations and to facilitate the identification of the wide-angle reflection events.
263   The shape and length of the wavelet, which is crucial for the performance of the predictive
264   deconvolution, was obtained using a trace autocorrelation methodology (Yilmaz, 2001).
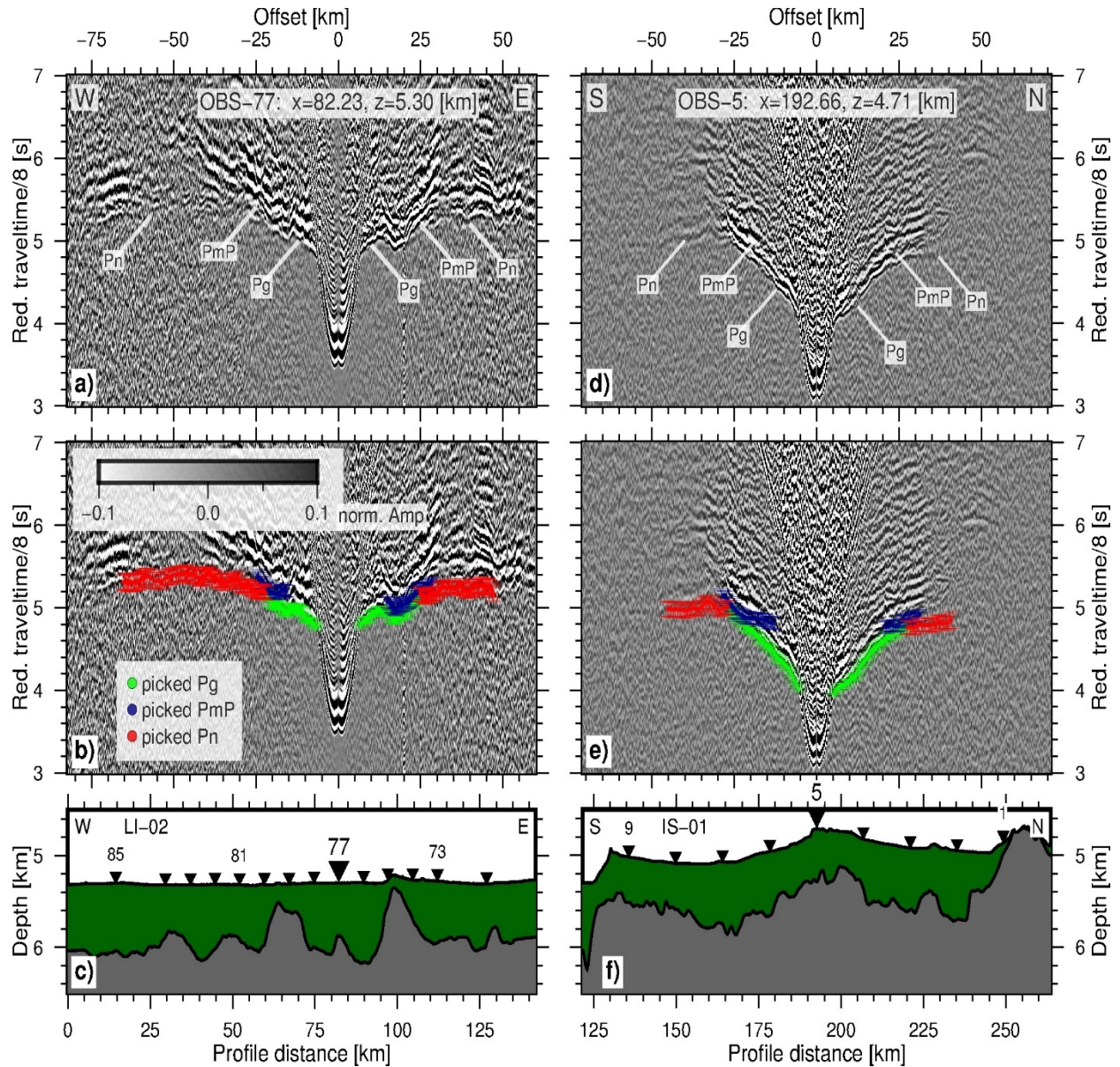
265 **Figure 2:** Record sections, labelled events and arrival picks for two selected OBS. **(a,d)** Processed
266 receiver gathers of OBS 77 (panel a; LI-02) and OBS 5 (panel c; IS-01) with labelled seismic events. The
267 travel time is reduced with 8 km/s. The amplitude is normalized by its maximum and clipped to 10 %.
268 The X and Z coordinate represent the along-profile-axis distance and the water depth of the OBS. **(b,e)**
269 The same record sections with travel time picks superimposed where colored dots and error bars illustrate
270 the picked arrivals for the three distinct seismic phases (Pg, PmP, Pn; see legend) and their individual pick
271 uncertainty. **(c,f)** Corresponding OBS locations (black inverse triangles), bathymetry and the sediment
272 thickness (green area) above the igneous basement (gray area). The OBS of the illustrated receiver gather
273 is highlighted. Every fourth OBS is labelled.

274 **4 Tomographic Traveltime Inversion**

275   For the tomographic inversion, a total of ∼10100 refracted first arrivals (Pg and Pn) and
276   ∼2700 wide-angle reflection arrivals (PmP) were manually picked on the 29 receiver gathers
277   (along both lines) and an offset-dependent uncertainty was assigned to each pick (e.g., Fig. 2).
278   The estimated uncertainties are 30-50 ms for Pg, 70 ms for PmP, and 80-110 ms for Pn arrivals.
279   Both the forward modeling and inversion were carried out using the package TOMO2D from
280   Korenaga et al. (2000). This code applies a hybrid scheme of the shortest path method from
281   Moser (1991) for calculating the least traveltimes between the grid nodes followed by a ray
282   bending method (Moser, 1992) to fine-tune these initial ray paths and minimize their travel
283   times. The ray bending is thereby conducted using a conjugate gradient method (Moser, 1992).
284   For the inverse problem the traveltime residuals for each raypath are equalized with
285   perturbations of the velocity and the reflector nodes with respect to a reference model, forming a
286   sparse linear system (Korenaga, 2000). Hereinafter, the linear system is normalized by data and
287   model covariance, regularized with smoothing and damping constraints (Korenaga, 2000) and
288   can be solved by the sparse matrix solver LSQR (Paige & Saunders, 1982).

289   The model domains were discretized into 726x141 (for line LI-02) and 1167x141 (for
290   line IS-01) cells with a horizontal node spacing of 200 and 300 m, respectively. The larger
291   horizontal node spacing for IS-01 was chosen due to the larger shot interval of 300 m. The
292   variable vertical node spacing increases with depth from 50 m at the seafloor to 250 m at the
293   bottom of the model. Initially, the horizontal and vertical correlation lengths, smoothing, and
294   damping weights that regularize the nonlinear inversion were tested and evaluated. Since the
295   seismic velocity generally varies more vertically than laterally, smaller vertical than horizontal
296   correlation lengths were used, which increased linearly with depth. Based on the smaller shot and
297   receiver spacing and hence the higher resolution, slightly smaller correlation lengths were used
298   for the line LI-02. Additionally, considering the lower uncertainties of Pg picks, we chose
299   smaller regulation weights for the Pg inversion than for the PmP and Pn inversion steps. A 1-D
300   velocity model of oceanic crust hung below the constrained sediment/basement interface (Fig. 3)
301   was used as a starting velocity model. All parameters of the discretization, forward modelling
302   and inversion are also listed in Table S2 in the supplementary material.

303   The inversion was carried out following a top-to-bottom approach. Hence, first, the near
304   offset Pg arrivals were inverted to constrain the shallower upper crust before adding the further
305   offset Pg arrivals and inverting again to obtain the velocity structure of the upper and
306   intermediate depths of the crust. Thereafter, the PmP reflection arrivals were added and inverted
307   with an initial flat Moho reflector with a predefined constant depth (on average 6 km below the
308   mean basement depth). The reflector is modeled as a floating reflector with only one degree of
309   freedom vertically, and is thus independent from the velocity nodes (Korenaga et al., 2000). A
310   depth kernel weighting factor, which controls the tradeoff between the velocity and the reflector
311   depth ambiguity from the PmP arrivals (Korenaga et al., 2000) was chosen to be 1 such that
312   velocity and reflector depth perturbation are equally weighted. Each iterative inversion stage in
313   the top-to-bottom approach is stopped by reaching a normalized target $\chi 2 \leq 1.2$ or when a
314   maximum number of iterations (eight for each Pg segment and PmP) is reached, which results in
315   an excellent fit to observed and calculated travel times (Fig. 4). The ray coverage in the model
316   domain is represented by the derivative weight sum (DWS; Toomey & Foulger, 1989), which
317   incorporates not only the number of rays going through each cell but also their individual path
318   length through the cell and their uncertainty.
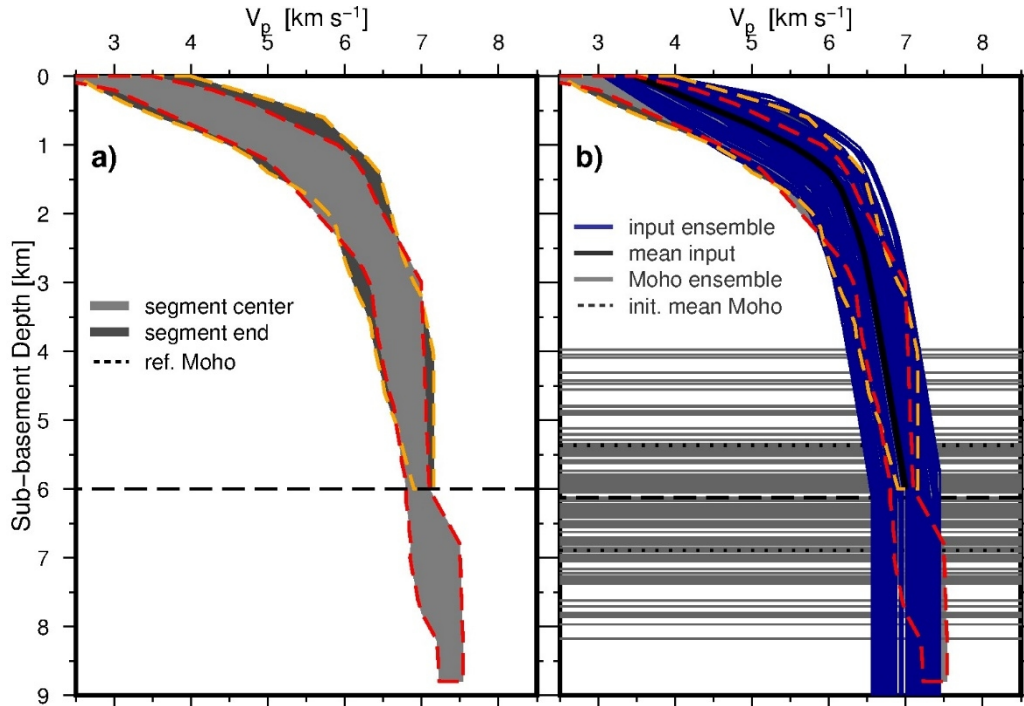
Figure 3: Velocity and Moho reflector input ensembles. **(a)** Reference velocity ensembles and crustal
thickness obtained for the central portion of the MAR segments (light grey, dashed orange frame) and the
segment ends (dark grey, dashed red frame) after Grevemeyer et al. (2018). **(b)** Randomized input
velocity (blue) and initial flat Moho (light grey) ensemble for Monte Carlo analysis. Solid, dashed, and
dotted black lines indicate the mean initial 1D-velocity-depth function, the mean initial flat Moho and its
standard deviation, respectively.

336   To minimize the bias from the initial model and to evaluate the model uncertainty, a
337 Monte Carlo analysis (MCA) was performed in which a set of 100 randomized starting velocity
338 models (e.g., Fig. 3) and a set of 100 initial flat Moho reflectors of various constant depths were
339 inverted and averaged to obtain the final crustal model and its standard deviation (see Appendix
340 1). For the MCA, the 100 1-D input velocity functions were randomized around a reference
341 velocity function for the Atlantic crust, which is derived as a mean from a compilation of
342 velocity-depth profiles from the Atlantic Ocean for ridge segment ends (Grevemeyer et al., 2018;
343 Fig. 3). The 100 initial flat reflectors were randomized around a flat Moho reflector 6 km below
344 the average basement depth.

345   After obtaining the final average crustal velocity model from the MCA, an initial velocity
346 model for the upper mantle was added and hung below the mean constrained Moho reflector. To
347 create the initial 1-D input velocity function for the upper mantle, we observed an apparent
348 velocity of 8 km/s in the Pn arrivals within the data, and reduced this slightly to 7.8 km/s at the
349 Moho depth. Below the Moho, the mantle velocity increase was defined subsequently by three
350 velocity gradients: 0.1 s-1 from 0 to 1 km, 0.05 s-1 from 1 to 5 km, and 0.04 s-1 from 5 km to the
351 model bottom. In the final stage of the entire cumulative inversion scheme, the picked Pn arrivals
352 were added, and all arrivals were inverted to obtain the final result that included the velocity in
353 the crust, the Moho reflector, the uppermost mantle (Figs 5 and 6). Due to the high uncertainty of
354 the Pn picks (80-110 ms) and a previously well constrained final crustal model, a normalized $\chi^2 \leq$
355 1.2 was thereby reached after only 2-3 iterations, despite larger damping weights in order to
356 avoid significant changes within the already constrained crust. The model error is estimated by
357 the computation of the RMS-fit and the normalized χ^2, which incorporates the data variance,
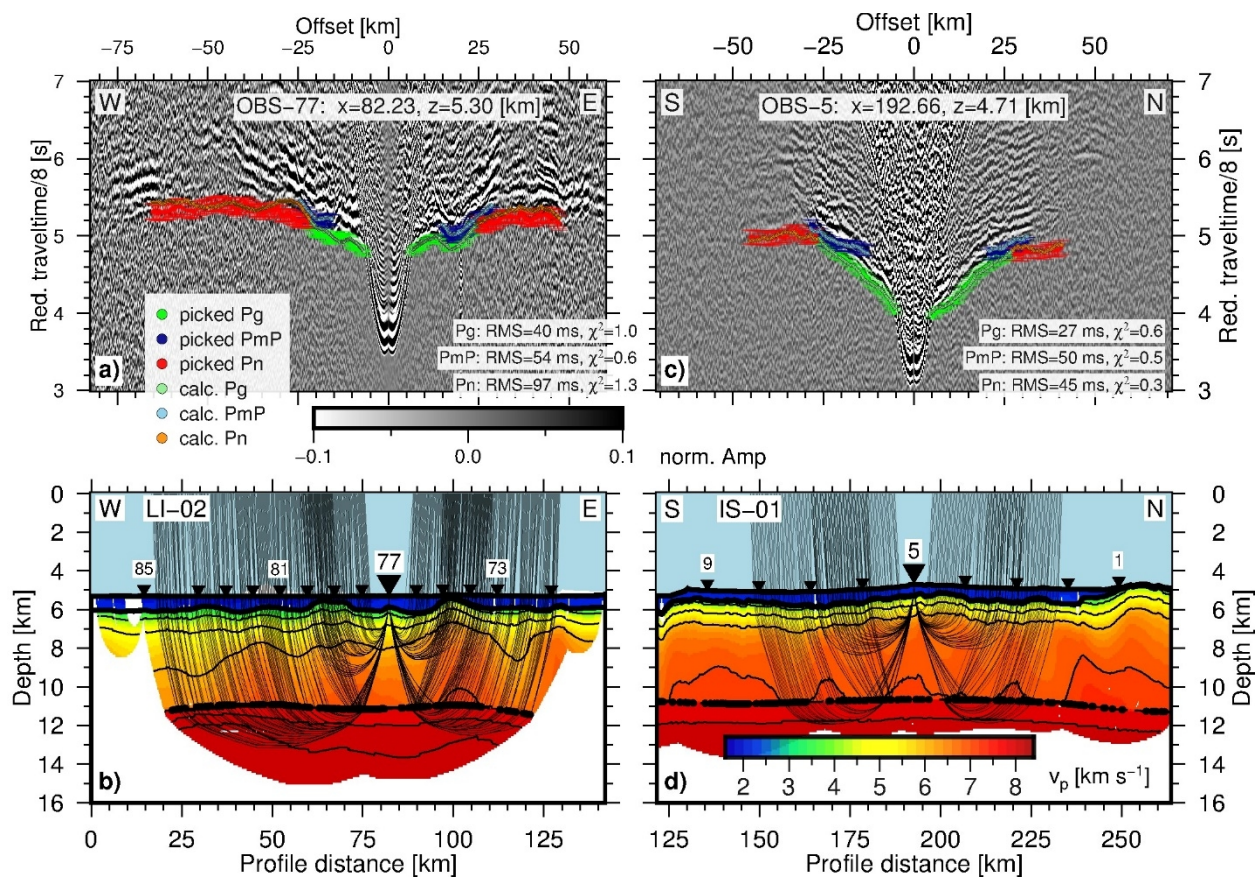358 represented by the individual pick uncertainty.

Figure 4: Traveltime fits and raypaths for two selected OBS. **(a,c)** Processed receiver gathers of OBS 77 (panel a) and OBS 5 (panel c) with picked and calculated travel times superimposed and **(b,d)** their corresponding ray paths superimposed on the final velocity models centered at OBS-5 (d) north of and OBS-77 (b) within the SPFZ-1. Thick black dots denote the modelled Moho reflection points, respectively. The velocity contour interval is 1.0 km/s for the crust, starting with 4 km/s, and 0.1 km/s for the mantle, starting at 8.0 km/s. The remaining elements are the same as in Figure 2.

To estimate the spatial resolution and the sensitivity of the inversion scheme with respect to the parametrization of the model space, we conducted multiple checkerboard tests with varying wavelengths and a velocity perturbation amplitude of 10 % (see Figs S6 and S7 in the Supplementary material). The results show that anomalies of 25 km horizontal and 5 km vertical diameter are well resolved with nearly full amplitude for both profiles. Anomalies of 15 km horizontal and 3 km vertical diameter are only relatively well resolved in the upper to intermediate crust. In particular, the low velocity anomalies are poorly recovered in the lower crust.

374   As our obtained Moho reflectors are rather flat and do not show much undulations we conducted
375   several regularization and resolution tests. To investigate the effect of the regularization on the
376   depth and the topography of the Moho, we significantly reduced the correlation length and the
377   smoothing and damping weights for the PmP inversion during the MCA (Table S3). As expected,
378   the results show more undulations, but with the reduction of the regularization we consequently
379   decrease the data fit to χ^2_{PmP}<1 and thus overfit the PmP-data. A comparison between the
380   resulting Mohos and the crustal thicknesses using different regularizations is presented in the
381   supplements (Figs S8 & S9). We further tested the resolution of our method in terms of the
382   combination of both an anomalous sinusoidal Moho reflector with two different wavelengths,
383   with an oscillating perturbation amplitude of 1 km, and gaussian velocity anomalies with a
384   perturbation amplitude of 10 %, placed above the Moho in the lower crust. The results show a
385   very good recovery of the velocity anomalies and a good recovery of the anomalous reflector for
386   perturbations with a wavelength of 70 km (Figs S10 and S11). Instead, the Moho perturbations
387   with a wavelength of 40 km are not resolved (Figs S12 and S13). We thus deduce that due to the
388   high uncertainties of the PmP picks we cannot resolve small scale undulations of the Moho
389   without introducing overfitting of the data. Hence, we favor the smoother Moho model with a
390   χ^2~1 that perfectly represents the data with respect to its uncertainties.

391   Finally, to test the sensitivity within the mantle we introduced gaussian anomalies with a
392   horizontal diameter of 50 km, a vertical diameter of 3 km and a perturbation amplitude of 5 %
393   (Figs S14 and S15) below the constrained Moho reflector. The results reveal that positive
394   anomalies in the mantle are well resolved up to a perturbation amplitude of 0.2-0.3 km/s.
395   Conversely, the negative anomalies are with amplitudes up to only 0.1 km/s significantly less
396   recovered. All results of the resolution tests are included in the supplementary material.

5 Tomographic Results

In the following paragraphs the results of the tomographic travel time inversion are presented separately for the two seismic lines: LI-02 running along the St. Paul fracture zone (Fig. 5) and IS-01 crossing the St. Paul fracture zone. Note, the results of line IS-01 running north-south (Fig. 6) are subdivided into the distinct areas of north of the SPFZ-1, crossing the SPFZ-1 and south of the SPFZ-1.

5.1 LI-02: Along the St.Paul Fracture Zone

5.1.1 LI-02: Crustal Seismic Structure along the St.Paul Fracture Zone

The crustal thickness along LI-02 varies from 4.8–5.6±0.3 km, resulting in a mean crust of 5.2 km (Tab. 1 and Fig. 7b). The velocities along the FZ, particularly in the western and central part of the profile, are remarkably lower in the upper and mid-crust with respect to the reference model (0.2-0.7 km/s; Fig A1). Along most of the profile, the seismic velocities do not exceed 5 km/s within a sub-basement-depth of 1 km, and the usual seismic layer 3 velocity of ~6.6 km/s (e.g., Christeson et al., 2019; Grevemeyer et al., 2018) is reached not before 3-4 km depth into the crust (Figs 5 and 8). However, the eastern part of the profile shows slightly higher velocities of up to ±0.2 km/s with respect to the reference model and ±0.4-0.8 km/s with respect to the western part of the profile. Further, these higher velocities (from 90 – 110 km along profile distance) coincide with a basement high within the FZ (Figs 5 and 7) and thicker crust, indicating an enhanced magma supply.
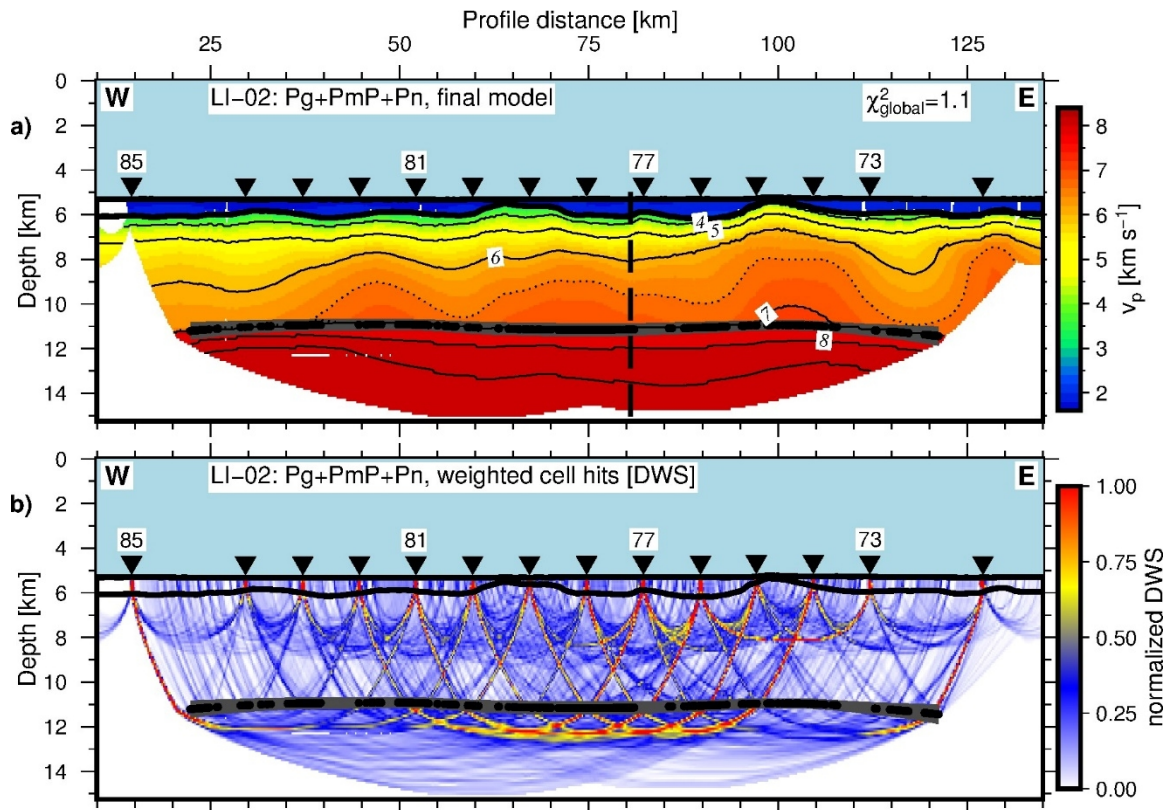
428 **Figure 5:** Inversion results for line LI-02. **(a)** Crustal and upper mantle velocity model obtained by
429 cumulative Pg, PmP and Pn inversion. The contour interval is 1 km/s in the crust starting at 4 km/s and
430 0.1 km/s in the mantle starting at 8.0 km/s. The dotted line represents a usual velocity of the lower crust
431 of 6.6 km/s. Black dots and grey shading denote the modelled Moho reflection points and the Moho
432 standard deviation, respectively. The vertical dashed line depicts the intersection location with line IS-01
433 (Fig. 1b). The remaining elements and symbols are the same as in Figure 4. **(b)** Corresponding
434 normalized DWS for the crust and upper mantle.

435 *5.1.2 LI-02: Upper Mantle Structure along the St. Paul Fracture Zone*

436   The Pn inversion yields a rather homogeneous upper mantle with velocities of ~8 km/s
437 along the profile LI-02 and hence parallel to the spreading direction (Figs 5 and 7). Abundant far
438 offset Pn arrivals up to 100 km on several OBS gathers provide ray penetration up to 6 km below
439 the Moho, and hence a good ray coverage in the upper mantle (Fig. 5). Therefore, these mantle
440 velocities are real and not attributable to the initial velocity model.

441 *5.1.3 LI-02: Uncertainties along the St. Paul Fracture Zone*

442   The final computed Pg, PmP, and Pn arrivals yield RMS fits of 46, 56, and 91 ms,
443   respectively, and result in a normalized global χ^2 of 1.1. During the MCA, the standard deviation
444   of the velocity model is reduced from 0.3-0.5 km/s to <0.2 km/s in the upper crust and < 0.1
445   km/s in the intermediate and lower crust (Fig. A1). The standard deviation for the Moho reflector
446   depth and hence the crustal thickness is reduced from an initial 0.75 km to a mean of 0.3 km. The
447   mean values and uncertainties for both crustal thickness and velocities are provided in Table 1.

448   5.2 IS-01: Across the St. Paul Fracture Zone

449   *5.2.1 IS-01: North of SPFZ-1*

450   The final crustal model for IS-01 reveals a relatively constant crustal thickness along the
451   whole profile (Figs 6 and 7) but can be subdivided into the two parts: north and south of the
452   SPFZ-1 in terms of velocity structure. The part north of the FZ encompasses a distance of ∼110
453   km (from 130 km to 240 km along profile distance), which displays a crustal thickness of 5.0-
454   5.4±0.3 km (mean=5.3 km). A thick crust, ~6.5±0.5 km (Fig. 7), is observed at the northern end
455   of the profile in a 15-20 km wide zone (at distance ~240 km), which coincides with a high
456   basement topography (Figs 6 and 7). However, since the Moho reflector north of ~240 km (along
457   profile distance) is not constrained by reversed ray coverage (Fig. 6), it may not be resolved
458   properly and is hence excluded from the further interpretation and statistical computations. The
459   velocity structure north of the FZ is relatively uniform and shows significantly higher crustal
460   velocities (+0.2-0.6 km/s) with respect to the reference model (Fig. A2).

461   The velocity depth-profiles in this region extracted from the final crustal velocity model
462   (in Figure 8 marked as o, p, and q) resemble the seismic structure of usual oceanic crust
463   containing the two-layer gradient structure with a high-velocity gradient in the upper crust and a
464   low-velocity gradient in the intermediate and lower crust representing layers 2 and 3,
465   respectively (Fig. 8 b, c). Here, layer 2 reveals velocities ∼4 km/s at the top increasing to ∼6.2-
466   6.5 km/s at its base (∼1.6±0.3 km sub-basement depth); the velocities of layer 3 increase from
467   ∼6.5-6.7 km/s at the top of the layer to ∼6.9-7.2 km/s at the base of the crust.

468   When compared to most of the profiles from LI-02, along the FZ, the layer 2-layer 3
469   boundary is more distinctively defined north of St. Paul. Further, crustal velocities are generally
470   higher, with values of ~4.5-5 km/s in the upper crust compared to <3.5 km/s at the top of the
471   crust along the FZ, and values of >6.8 km/s in the lower crust compared to ~6.3-6.8 km/s at the
472   base of the crust along the FZ. However, the eastern domain of LI-02 (profiles d, e in Fig. 8)
473   shows a closer similarity to the crust north of St. Paul, with a potential layer 2-layer 3 transition
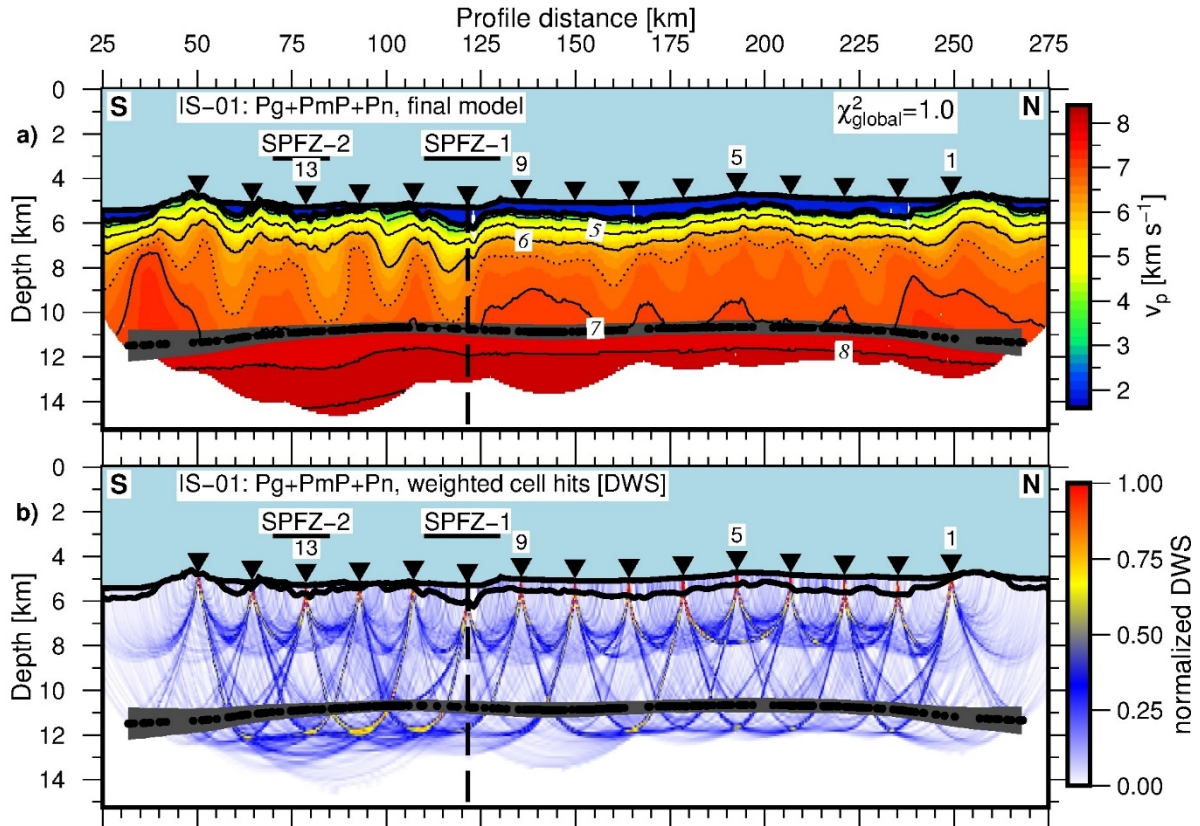474   occurring at ~1.7 km below the basement.

Figure 6: Inversion results for line IS-01. **(a)** Crustal and upper mantle velocity model obtained by cumulative Pg, PmP and Pn inversion. **(b)** Corresponding DWS for the crust and upper mantle. Thick horizontal labelled bars indicate the two FZs and their extent derived from the bathymetry (Fig. 1b). The remaining figure elements and contour intervals are the same as in Figure 5.

5.2.2 IS-01: Across SPFZ-1

Across the SPFZ-1 from north to south, the crustal thickness decreases from 5.2±0.3 km to 4.8±0.3 km (Figs 6 and 7). Within a distance of ~20 km from the center of the valley, the crust thickens again to 5.3±0.4 km, resulting in a zone of reduced crustal thickness about 20 km-wide The FZ exhibits only slightly lower velocities compared to the reference model at segment ends (Fig. A2). However, with respect to the adjacent crust in the north of the FZ it reveals a remarkable velocity reduction of 0.4-0.8 km/s throughout the upper and mid-crustal region (Fig. 8c: compare profile n with o, p, q).

5.2.3 IS-01: South of SPFZ-1

489   The southern part of the profile differs remarkably from the observations in the northern
490 part, showing more heterogeneities both in crustal thickness and velocities (Figs 6 and 7). The
491 crust thickens from the FZ southwards from a rather thin crust of 4.8±0.3 km to 5.6±0.3 km
492 within a distance of ∼60 km (from 115 km to 55 km along reverse profile distance) and reaches
493 a maximum thickness of 6.7±0.4 km below another basement high at the southern end of the
494 profile. However, similarly to the northern limit of the profile, the crustal thickness for distance
495 <55 km is not very well constrained and hence is not included in the statistical computations and
496 discussion. The velocity distribution shows both positive and negative anomalies with respect to
497 the reference model, but the velocities are generally lower than those north of the FZ by 0.2–0.8
498 km/s (Figs 8 and A2). The strong velocity variations affect both the upper and the lower crust.
499 Parts of the structure south of St. Paul, for example, the low velocity zone just north of the
500 SPFZ-2 (profile m in Fig. 8a, c), show a similar range of velocities to the structure along the FZ.
501 However, they also show a clear division into two layers with a high gradient upper crust and
502 low gradient mid- to lower-crust (occurring at ~1.5 km for profile m), and so cannot be
503 considered to exhibit the same crustal structure as inside the FZ. Conversely, other sections south
504 of St. Paul, such as at ~70 km along profile (profile l in Fig. 8a,c), show a more similar velocity
505 structure to the crust north of the FZ.

506 *5.2.4 IS-01: Upper Mantle Structure across SPFZ*

507   The Pn inversion yields rather homogeneous upper mantle velocities of 7.8-8 km/s along
508 the whole profile IS-01 (Figs 6 and 7). Due to a decreasing signal/noise ratio at far offsets in
509 some record sections and a conservative picking approach of only including picks with
510 uncertainties of <0.12 s, Pn offsets of good quality were generally limited to offsets smaller than
511 60 km.

512 *5.2.5 IS-01: Uncertainties across SPFZ*

513   The final computed Pg, PmP, and Pn arrivals yield RMS fits of 41, 67, and 85 ms,
514 respectively, resulting in a global normalized $\chi2 = 1.0$ for both the crustal and the joint crustal
515 and mantle models. An example of traveltime fits is illustrated in Figure 4. During the MCA, the
516 velocity standard deviation was reduced from 0.3-0.5 km/s to ∼0.2 km/s in the upper crust and <
517 0.1 km/s in the middle and lower crust (Fig. A2). The significantly higher uncertainty in the
518 shallow crust is caused by predominantly vertical travel path of the rays and the resulting low
519 sensitivity. The ray coverage is highest between 1.5-2.0 km of sub-basement depth since this is
520 the depth where the most rays turn (Fig. 6). Note that beyond the receiver line the crustal
521 velocities are constrained by only one-sided ray coverage and thus yield a very high uncertainty.
522 The standard deviation for the Moho reflector depth and hence the crustal thickness north of the
523 FZ, the FZ itself and south of the FZ is reduced from 0.75 km to 0.3 km. Mean values and
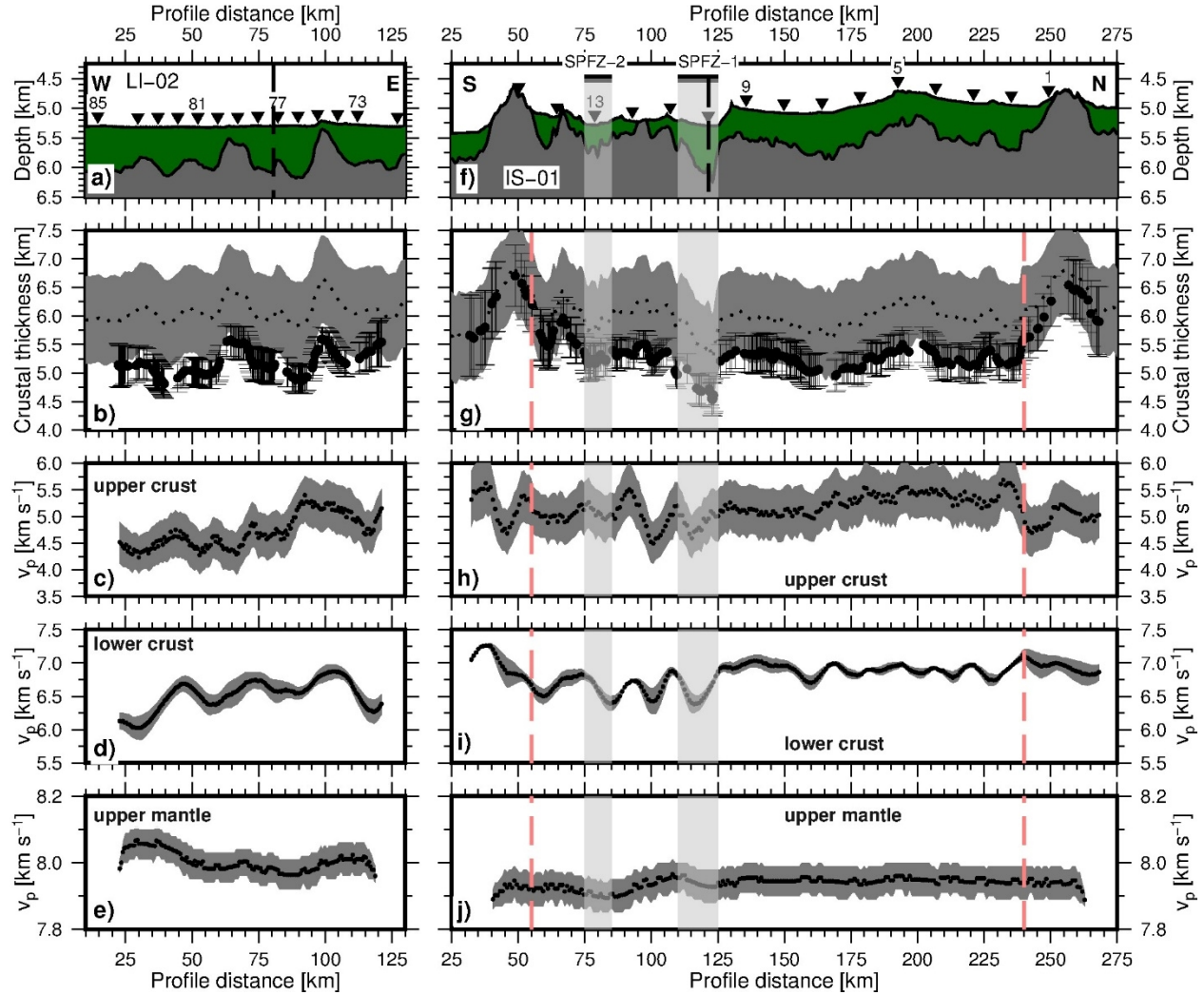524 uncertainties for both crustal thickness and velocities are provided in Table 1.

Figure 7: Bathymetry, sediment and crustal thickness as well as mean velocities for upper and lower crust and upper mantle along both refraction lines (LI-02: panels a-e, IS-01: panels f-j). **(a,f)** Bathymetry, sediment thickness (green region) above the basement (gray region) and OBS locations. **(b,g)** Black dots with error bars denote the crustal thickness obtained from the modelled Moho reflection points and their standard deviation. The dotted line and grey shading denote the mean and standard deviation of the crustal thickness input ensemble. **(c-e, h-j)** Vertically averaged velocities for the upper crust (panels c,h; 0.25 - 1.25 km sub-basement), lower crust (panels d,i; 0.25 -2.5 km above Moho) and the upper mantle (panels e,j; 0.25 -1.25 km below Moho) and their corresponding standard deviation (grey shading) along the two lines, respectively. Vertical light grey shading indicates the extent of the two fracture zone valleys (SPFZ-1,SPFZ-2; Fig. 1). Vertical red dashed line excludes the edge regions that are not constrained by reverse ray coverage for IS-01. Remaining elements are the same as in Figure 2 and 5.
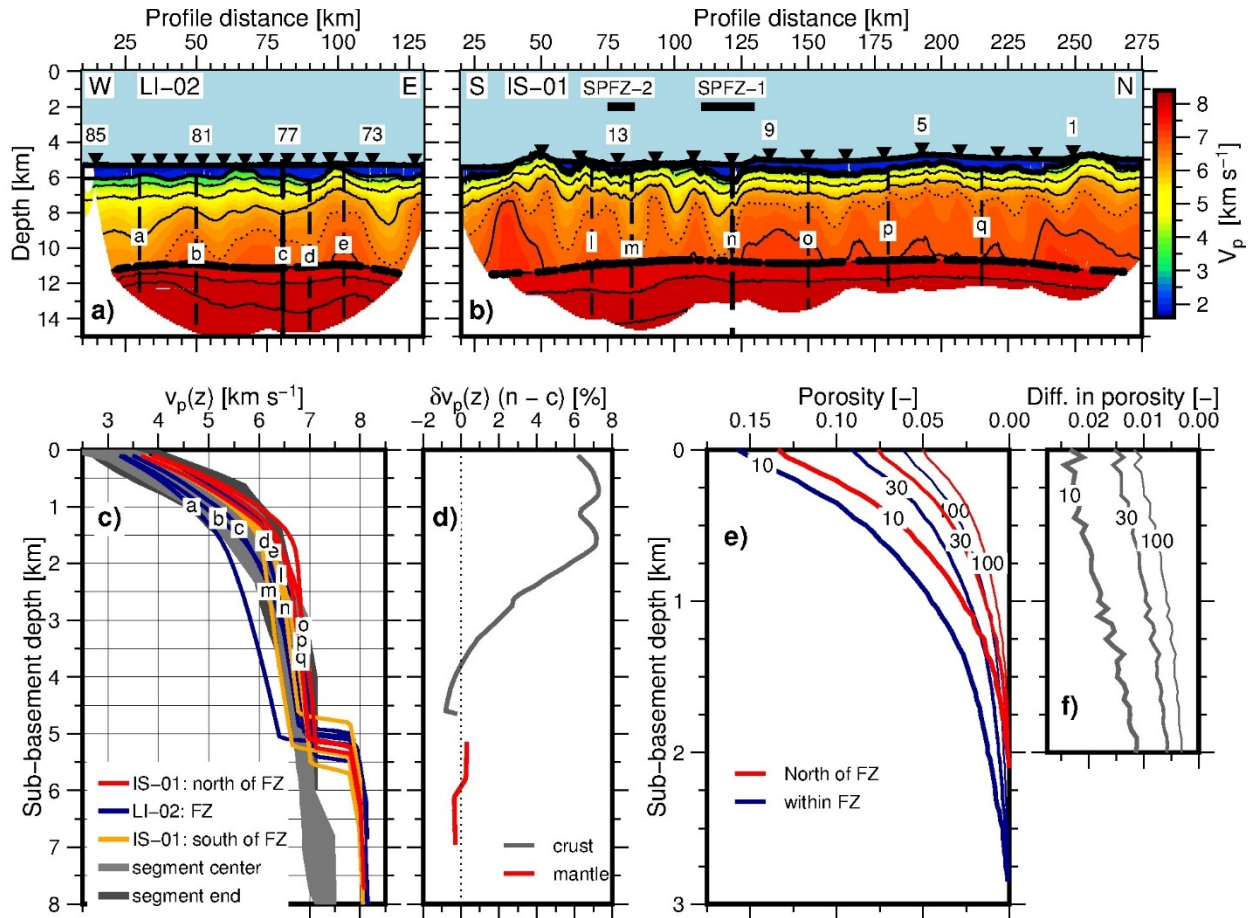
Figure 8: Velocity and porosity compilation for the two lines. **(a,b)** The locations for the selected 1-D velocity-depth profiles (labelled vertical dashed lines) of line LI-02 (a) and line IS-01 (b) are superimposed on the final velocity models. Remaining figure elements are the same as in Figure 5. **(c)** Extracted velocity depth profiles. Each profile represents the average of the velocity-depth profiles for four adjacent horizontal nodes. **(d)** Velocity difference within the vicinity of the profile intersection (profile n – profile c). **(e)** Porosity estimates using DEMA for averaged velocity depth functions of the SPFZ-1 (averaged from 15 -120 km distance alongside LI-02) and the crust north of it (averaged from 130 -240 km distance alongside IS-01). The labels indicate different aspect ratios of the fractures. **(f)** Difference in porosity between the crust within the fracture zone and north of it (FZ – North).

5.3 Summary of Results

548   Table 1 lists the findings of this study regarding crustal and upper mantle properties for
549 three distinct regions: north of St. Paul, south of St. Paul, and along the St. Paul FZ itself. The
550 mean upper crustal velocity is obtained from averaging vertically and horizontally down from
551 0.25-1.25 km of sub-basement depth. The lower crustal velocity is obtained by vertical and
552 horizontal averaging of the 0.25–2.5 km (reversed depth) of the lower crust just above the
553 constrained Moho reflector. The mean upper mantle velocity is obtained from vertical and
554 horizontal averaging between 0.5-2 km below the constrained Moho reflector. Only regions with
555 sufficient ray coverage contribute to these statistical computations. The overall variability of the
556 velocity structure in the survey area is also summarized in Figure 9, where 1-D velocity depth
557 profiles are extracted for both lines with an interval of three horizontal nodes and colored for the
558 distinct regions.

559 **Table 1**: Summary of the main findings regarding crustal and upper mantle properties.

Parameter / Location	**North of FZ**	**Along FZ**	**South of FZ**
Crustal thickness [km]	5.3 ± 0.3	5.2 ± 0.3	5.4 ± 0.3
Vp upper crust [km/s]	5.2 ± 0.5	4.7 ± 0.4	5.1 ± 0.4
Vp lower crust [km/s]	6.9 ± 0.1	6.5 ± 0.1	6.7 ± 0.1
Vp upper mantle [km/s]	7.9 ± 0.05	8.0 ± 0.05	7.9 ± 0.05

560
561
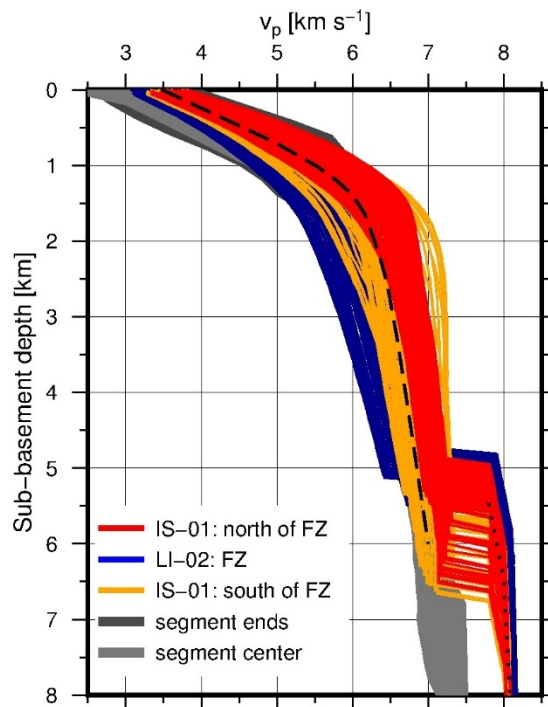
562 **Figure 9:** Velocity-depth compilation. The 1-D velocity-depth functions are extracted with an interval of
563 three horizontal nodes (0.6 km for LI-02 and 0.9 km for IS-01, respectively) and color coded for the
564 distinct regions (see legend). Grey shading indicates the reference velocity ensemble from Grevemeyer et
565 al. (2018). The dashed and dotted lines denote the mean initial velocity-depth function for the crust and
566 the initial velocity-depth function used below the constrained Moho for the Pn inversion, respectively.

567

568 **6 Discussion**

569   6.1 Crustal Thickness along the St. Paul Fracture Zone

570   In the literature the term fracture zone has been loosely used for both the tectonically and
571 seismically active transform fault offsetting the spreading axis and its inactive fracture zone (e.g.,
572 Detrick et al., 1993). Here, we will use the term "transform fault" for the active plate boundary
573 offsetting the spreading axis, while with the term "fracture zone", we will refer to the inactive
574 fossil trace where lithosphere of contrasting age meets and subsidence occurs on either side
575 depending upon their thermal structures (e.g., Menard, 1967; Sandwell, 1984). This clear
576 separation between the fracture zones and the transform faults is important as recent evidence
577 suggest that crust accreted along a transform fault might be affected by processes acting at ridge-
578 transform intersections before it converts into a fracture zone (e.g., Grevemeyer et al., 2021;
579 Marjanović et al., 2020).

580   The St. Paul fracture zone reveals an average crustal thickness of ~5.2 km, which is
581 roughly 1 km thinner when compared to the global average of normal oceanic crust of 6.15 km
582 thickness (e.g., Christeson et al., 2019), but close to the thickness of oceanic crust in the
583 equatorial Atlantic, from 5.6-6.0 ±0.1 km (Vaddineni et al., 2021). Interestingly, it did not show
584 any significant change in the crustal thickness with respect to the crust found either to the north
585 or south of the FZ. Furthermore, its thickness is in the same order of magnitude as the Chain FZ
586 (Marjanović et al., 2020) and falls in the range of other FZ surveyed in the Atlantic Ocean, e.g.,
587 ∼4.5 km at Tydeman FZ (e.g., Calvert & Potts, 1985; Potts et al., 1986a), ~5 km for the
588 Mercurius FZ (Peirce et al., 2019). Additionally, Davy et al. (2020) observed a crustal thickness
589 of ~6 km for the Late Cretaceous Marathon FZ. A new compilation of crustal thicknesses of
590 major Atlantic TF and FZ (Marjanović et al., 2020) indicates thin crust at some transform faults
591 (2-5 km) whereas most fracture zones have crustal thicknesses in the range of usual oceanic crust
592 (5-7 km). An exception, however, is the Kane FZ, which shows a significantly thinner crust (2-3
593 km) (Cormier et al., 1984; Detrick & Purdy, 1980).

594   In general, the thinner crust found along transform faults and fracture zones is clearly
595   consistent with the concept of focused mantle upwelling along mid-ocean ridges (e.g., Lin et al.,
596   1990; Tolstoy et al., 1993), supporting magmatically starved conditions acting at transform
597   faults. Further, geological observations and sampling of rocks from transform valleys at slow-
598   and ultraslow-spreading ridges often reveals exposed upper mantle rocks near segment ends
599   (e.g., Cannat, 1993; Cannat et al., 1995). These observations are consistent with the inferences
600   from Detrick et al. (1993), suggesting that crust found at both transform faults and fracture zones
601   is "thin, intensely fractured, and hydrothermally altered basaltic section overlying ultramafics
602   that are extensively serpentinized in places". However, the crust within the St. Paul FZ is only
603   slightly (0.1-0.3 km) thinner when compared to oceanic crust adjacent to the FZ. A gradual
604   crustal thinning over a distance of several tens of kilometers on either side of a fracture zone or
605   transform fault, as reported previously for some fracture zones in the North Atlantic (White et al.,
606   1984), is not observed, neither across the St. Paul FZ as shown in our data nor across the Chain
607   FZ (Marjanović et al., 2020). One interpretation might be that the crust found along transform
608   faults may deviate significantly from oceanic crust in fracture zones, as envisioned recently
609   (Grevemeyer et al., 2021).

610   A similar deduction has been made recently to explain the crustal structure across the
611   Chain FZ. Marjanović et al. (2020) suggested that lateral dyke propagation along the adjacent
612   spreading axis into the transform fault augments crust at RTIs. Such a dyke injection is supported
613   by the presence of J-shaped ridges in the vicinity of RTIs observed in a global study of transform
614   faults (Grevemeyer et al., 2021). Bathymetric data obtained along the St. Paul FZ reveal a
615   number of such J-shaped ridges, though ridge tips are often blanketed by sediments (Fig. 1c).
616   Dyking is possibly controlled by 3-D mantle upwelling as envisioned by Lin et al. (1990) at slow
617   spreading ridges. At the 21°30'N segment of the MAR, ridge propagation forced by lateral
618   dyking has not only advanced into the transform domain, but cut through a transform fault,
619   causing its die-off (Dannowski et al., 2018). We therefore propose that a second phase of RTI
620   magmatic accretion might be an important process shaping the crust and lithosphere at the
621   proximal end of transform faults. However, the proposed model is still rather conceptual and thus
622   we cannot rule out that magma migrates also along the base of crust. A scenario where magma is
623   supplied within the mantle before intruding into the crust may explain better the layer-2/layer-3
624   type layered structure of the crust found along St. Paul than a model where dyking alone is
625   governing RTI magmatism.

626   The occurrence of a second phase of RTI magmatism is supported by geological
627   sampling, revealing that lithosphere along transform valleys is generally characterized by mantle
628   exhumation (e.g., Fox et al., 1986; Tucholke & Lin, 1994), while outside corners and fracture
629   zones are dominated by magmatically accreted basaltic crust (e.g., Karson & Dick, 1984). The
630   observation that even the floor of a fracture zone valley (Karson & Dick, 1983) is composed of
631   basaltic rocks supports the interpretation that transform crust is being augmented at RTIs by
632   magmatism.

633 Finally, it is important to emphasize if crust and mantle are indeed modified by a second
634 phase of magmatic activity at RTIs it may also explain some of the local variability observed
635 both in our models and features not explicitly modelled here, like amplitude variations of either
636 PmP or Pn. Thus, in contrast to oceanic crust emplaced at a spreading segment, at the RTI
637 magmatism only may modulate the pre-existing highly hydrated lithosphere. We therefore cannot
638 rule out that fragments of serpentinized mantle or hydrated lower crust occur along fracture
639 zones. However, our data strongly support the view that the overall structure of the St. Paul FZ is
640 magmatic in origin rather than featuring hydrated lithosphere as proposed previously (e.g.,
641 Detrick et al., 1993).

642

643 6.2 Seismic Velocity Structure along the St. Paul Fracture Zone

644 Crustal seismic velocities along the SPFZ reveal significantly reduced values when
645 compared to the crust north of the FZ. Throughout the upper and middle crust, velocities are
646 reduced by 0.2-1.1 km/s. The velocity structure within the FZ, however, still shows the typical
647 features of a two layered structure of normal oceanic crust formed at segment ends (Fig. 8c), i.e.,
648 a high-velocity gradient upper crust and a low-velocity gradient lower crust. This decrease in
649 seismic velocity throughout the entire crust might be best explained by the presence of large-
650 scale porosity and fracturing of crustal rocks. Nevertheless, the observed layered structure
651 closely resembling oceanic crust supports that crust, though fractured, was magmatically
652 accreted. Therefore, the crust found along the St. Paul FZ differs profoundly from the
653 conventional wisdom where crust at discontinuities is generally characterized by basically a
654 single layer and thin crust (e.g., Davy et al., 2020). For a mature oceanic crust near
655 15°N/55°30'W in the Atlantic Ocean, Davy et al. (2020) suggest that the structure of ridge crest
656 discontinuities is controlled by the behavior of adjacent spreading segments. Therefore, crust
657 accreted at discontinuities near magmatically starved spreading segments will mimic those
658 conditions, while crust formed at transforms or higher-order ridge offsets adjacent to
659 magmatically robust segments will reflect magmatically accreted crust. The accretion near St.
660 Paul seems to have occurred during a period of constant magma supply from the mantle.

661   To estimate the porosities associated with decreasing velocity, we carried out a
662   differential effective medium analysis (DEMA) after Taylor and Singh (2002). The DEMA was
663   performed for a host rock of basaltic composition and assuming a population of aligned,
664   elongate, fluid-filled fractures with aspect ratios (ARs) between 10 and 100 (Supplementary Fig.
665   S5). The porosities are computed for laterally averaged 1-D velocity-depth profiles for both
666   within the SPFZ-1 (line LI-02, from 25- 120 km along profile distance) and the crust resembling
667   normal oceanic crust north of the SPFZ-1 (line IS-01, from 130-240 km along profile distance).
668   The results and their deviation for three different ARs (10, 30, 100) are illustrated in Figures 8e
669   and 8f. We obtain porosities decreasing from up to ~15% in the top of the crust to ∼0 % at sub-
670   basement depths at 2.0-2.75 km for an AR of 10. For an AR of 100 in contrast, the porosity is
671   reduced from only ∼6 % at the top of the basement to ∼0 % at depths of 1.5-2 km. Depending
672   on the AR the DEMA reveals porosities that are ~2.25 % (AR=10) to 0.5-1 % (AR=100) higher
673   for the FZ with respect to the crust north of it (Fig. 8f). A recent study of the crust at the
674   Romanche TF indicate that the porosity could be 15% near the seafloor decreasing to 1% at the
675   base of the crust (Gregory et al., 2021). If similar porosity was present within the active St. Paul
676   TF, the reduced porosity could be explained by combination of lateral dyke injection at the RTI
677   (Marjanović et al., 2020) and hydrothermal alteration and mineral precipitation (Audhkhasi &
678   Singh, 2019; Grevemeyer et al., 1999) during the early development of the fracture zone.

679   Increased porosity, which in turn causes decreasing seismic velocities, might be related to
680   past deformation along the shear zone of the transform fault and/or emplacement of crust in a
681   tectonically dominated environment at RTIs. This observation nurtures previous interpretation
682   that fracture zones might be formed by hydrothermally altered basaltic and gabbroic sections that
683   are to some degree fractured and faulted, as envisioned earlier (e.g., Detrick et al., 1993; White et
684   al., 1984). However, even though crust might be partially altered and fractured, within the St.
685   Paul FZ the mantle rocks do not seem to consist of extensively serpentinized peridotite. Instead,
686   the presence of clear PmP reflection arrivals along the FZ valley and a continuous upper mantle
687   Pn refraction with apparent velocity of ∼ 8 km/s support a relatively dry mantle with a low
688   degree of hydration or even the absence of upper mantle serpentinization along the entire section
689   of the SPFZ-1. Inverted velocities along LI-02 are in the order of ~8 km/s (Fig. 7) and therefore
690   much faster than mantle velocity of <7.5-7.8 km/s reported for some Atlantic transform faults
691   (e.g, Detrick et al., 1993; Davy et al. 2020), supporting our interpretation. The dehydration of the
692   mantle might be caused by the presence of higher temperature and crustal thickening dyke
693   injection at the RTI, where the transform fault becomes a fracture zone.

694   6.3 Crustal Thickness as a Function of Distance across St. Paul Fracture Zone

695   Most previous studies along the axis of the MAR have revealed a strong dependence of
696 crustal thickness variations along the ridge crest (e.g., Lin et al., 1990) and hence distance to a
697 transform fault. For example, between 33-35°N of the MAR, Canales et al. (2000), and Hooft et
698 al. (2000) observed that crustal thickness varies significantly as a function of distance from both
699 the Oceanographer transform fault and non-transform offsets, showing thick crust at segment
700 centers (up to 8 km) and thin crust at segments' ends (<3 km). Similar features are observed at
701 the MAR at 21°N (Dannowski et al., 2011), and 5°S (Planert et al., 2009) and along the ultra-
702 slow spreading Southwest Indian Ridge at 50°E (Niu et al., 2015), and 66°E (Muller et al.,
703 1999). In general, crustal thickness at segment ends of slow-spreading ridges is in the order of 4-
704 6 km thick and at segment centers thickness may increase to 7-9 km (e.g., Grevemeyer et al.,
705 2018). It is, therefore, remarkable that our north-south profile reveals an almost constant
706 thickness of 5.2-5.6 km over 100 km from the FZ with no obvious dependence of crustal
707 thickness with distance to the St. Paul fracture zone at 2°N. Similar features are reported for the
708 MAR in the vicinity of the Chain fracture zone, where crustal thickness is in the order of 4.6 to
709 5.9 km, showing no significant imprint of the transform discontinuity on ridge crest
710 segmentation (Marjanović et al., 2020). One explanation might be that mantle upwelling in the
711 equatorial Atlantic has been more sheet-like, and hence more similar to the type of mantle
712 upwelling imagined for fast-spreading ridges rather than plume-like or 3-D mantle upwelling
713 suggested for the slow-spreading MAR (Lin & Morgan, 1992). However, the reason why mantle
714 upwelling in the equatorial Atlantic should differ from elsewhere along the MAR (e.g., Hooft et
715 al., 2000; Planert et al., 2009; Dannowski et al., 2011) remains elusive.

716   Another interesting feature is that the observed crustal thickness averages ~5.4 km along
717 the ~200 km long north-south trending profile (IS-01). Farther south, between 0° and ~3°S
718 around the Chain FZ, crustal thickness is 4.6-5.9 km (Marjanović et al., 2020) and at 2°S of the
719 MAR the crustal thickness ranges from 5.6 to 6.0 km along a 600 km long flow line profile
720 (Vaddineni et al., 2021). However, Christeson et al. (2020) reported from five ridge parallel
721 profiles at 31°S a significant crustal thickness variations of 3.6 to 7.0 km for different crustal
722 ages (6-60 Ma), but an almost constant thickness along each profile and thus for crust of the
723 same age, suggesting that the equatorial and south Atlantic shows consistently thinner crust when
724 compared to the average thickness of 7 km reported by White et al. (1992) for the Atlantic.
725 However, we have to note that that data compiled by White et al. (1992) occurred predominantly
726 in the North Atlantic with a large number of experiments in the north-western Atlantic where
727 crust is in the order of 7-8 km (e.g., Purdy, 1983; Minshull et al., 1991), suggesting that previous
728 estimates might be biased. In contrast, the majority of crustal thickness estimates, either along
729 our profiles or elsewhere in the equatorial or south Atlantic region, compares well with global
730 estimates of the global mean crustal thickness (e.g., Chen, 1992; Christeson et al., 2019; Harding
731 et al., 2017; Van Avendonk et al., 2017), revealing an average global crustal thickness of 6.15 km
732 (Christeson et al., 2019). Therefore, most observed crustal thickness estimates compare well to
733 predictions from petrological models, suggesting an average crustal thickness of 6 km emplaced
734 at a normal mantle temperature of 1300°C (e.g., McKenzie & Bickle, 1988; Korenaga et al.,
735 2002). However, slightly reduced crustal thickness in the equatorial Atlantic of ~5.3 km between
736 Chain and Romanche, roughly 6 km north of Romanche (Gregory et al., 2021) and <5.5 km
737 along our longitudinal profile may supports a cooler mantle underlying the equatorial Atlantic.
738 This interpretation is supported by the exceptionally low degree of melting of the upper mantle
739 in the equatorial Atlantic as indicated by the chemical composition of mantle-derived mid-ocean
740 ridge peridotites and basalts (Bonatti et al., 1993; Dalton et al., 2014) and upper mantle S-wave
741 velocity (Grevemeyer, 2020; James et al., 2014).

742 6.4 Anisotropy

743   To assess the crustal and mantle anisotropy, the velocity structure from both seismic lines
744 was compared in the vicinity of their intersection, averaging properties over a roughly 1 km long
745 section (due to different node spacing we averaged 0.8 km along LI-02 and 1.2 km along IS-01).
746 Figure 8d shows the velocity structure of the profiles at the intersection. Positive values indicate
747 faster velocities mapped along line IS-01 running roughly north-south and hence parallel to the
748 strike of the ridge axis. Anisotropy reaches a maximum of ~7% in the upper 2 km of the crust
749 and decreases continuously to zero at a depth of ~4 km below the basement and thus may occur
750 within the sheeted dykes. Within the upper mantle, no significant velocity anisotropy can be
751 observed.

752 Our observation of the upper to mid-crustal anisotropy indicates higher velocities perpendicular
753 to the fracture zone (i.e., along the strike of the ridge) with respect to velocities obtained parallel
754 to the fracture zone (i.e., perpendicular to the ridge axis). It is interesting to note that our
755 observations are consistent with that at the East Pacific Rise, where 4% of anisotropy was
756 observed with the fast direction roughly trending along the strike of the ridge crest (e.g., Dunn &
757 Toomey, 2001), which was interpreted to represent the effect of ridge-parallel trending faults. At
758 St. Paul, the fast-direction seems also to be orientated parallel to the spreading axis. Therefore, if
759 the observed crustal anisotropy would be caused by a set of faults it would support a set of faults
760 cutting through FZ. Alternatively, anisotropy could be related to the emplacement of dykes,
761 which are the dominant feature at 1 to 3 km depth in oceanic crust. One interpretation might
762 therefore be that crustal anisotropy reflects J-shaped ridges migrating into the transform domain.
763 However, one must be careful in interpreting the crustal anisotropy as it is derived from two
764 crossing profiles.

765   Another interesting feature is the lack of any apparent upper mantle anisotropy. Gaherty
766 et al. (2004) observed 3.4% of upper mantle anisotropy in the North Atlantic to the south of
767 Bermuda and in the Pacific mantle anisotropy is a striking feature, with values reaching 6-7% in
768 short offset experiments at the East Pacific Rise (Dunn & Toomey, 1997; Dunn et al., 2000).
769 Therefore, the absence of any anisotropy is a puzzling feature and it might therefore be
770 reasonably to argue that mantle velocity along the fast direction and hence along the fracture
771 zone might be with 7.9-8.1 km/s rather low. However, as stresses rotate over a short distance
772 when approaching a transform fault (Morgan & Parmentier, 1984), mantle flow might be
773 distorted along fracture zones and hence anisotropic pattern. In general, a velocity of ~8 km/s is
774 in the range of observations from mature lithosphere when being sampled along ridge parallel
775 profile (e.g., Davy et al., 2020; Gaherty et al. 2004) and much lower when compared to, for
776 example, a flow line profile at 2°S where Vaddineni et al. (2021) observed in 20 to 30 Myr old
777 lithosphere an upper mantle velocity of ~8.2 km/s. Observations obtained from the travel times
778 of Pn arrivals of regional earthquakes recorded at moored hydrophones support this discrepancy,
779 revealing for equatorial upper mantle a seismic velocity of 7.7 km/s in the slow and 8.4 km/s in
780 the fast direction (de Melo et al., 2020). Therefore, it might be reasonable to suggest that some
781 small degree of uppermost hydration may occur along the SPFZ to explain somewhat lower
782 mantle velocity in the fast direction of anisotropy.

783 7 Conclusions

784   We presented new constraints from seismic reflection and wide-angle data surveying the
785 crustal and upper mantle structure along and across the St. Paul fracture zone, one of the largest
786 transform faults in the equatorial Atlantic Ocean. High-resolution P-wave travel time
787 tomography revealed a number of key observations:

788   1.) Crustal structure along the fracture zone shows the typical layering of magmatically
789 accreted oceanic crust with a crustal thickness of 5 to 5.5 km, a clearly defined seismic Moho
790 and an upper mantle velocity of ~8 km/s.

791   2.) Crustal thickness across the fracture zone is in the order of 5 to 6 km, showing only a few
792   hundreds of meters of crustal thinning in the vicinity of the St. Paul fracture zone. However,
793   crust at St. Paul is slightly thinner than anywhere else along the line. Nevertheless, the roughly
794   200 km long well-resolved part of the fracture zone crossing profile did not show the same
795   features and strong crustal thickness variation of 2-4 km found along the active Mid-Atlantic
796   Ridge elsewhere (e.g., Canales et al., 2000; Dannowski et al., 2011; Hooft et al., 2000; Planert et
797   al., 2009) and thus did not show strong evidence supporting decreased melt production and hence
798   occurrence of magmatically starved crust at transform faults (e.g., Lin et al., 1990; Tolstoy et al.,
799   1993).

800   3.) Crustal seismic velocities along St. Paul are a few percent slower than farther away from it.
801   This observation may suggest that crust along the fracture zone has either higher porosity,
802   probably caused by a larger degree of fracturing, or it may reflect anisotropy. Unfortunately,
803   anisotropy is poorly resolved in the two crossing profiles.

804   4.) Mantle velocity of ~8 km/s along the transform fault did not reveal strong evidence for
805   serpentinization of the uppermost mantle below the FZ, a feature which has previously been
806   reported for a number of Atlantic fracture zones (e.g., Detrick et al., 1993) and was interpreted in
807   terms of highly fracture and hydrated lithosphere. However, with ~8 km/s upper mantle velocity
808   it is only slightly faster along the transform fault that with ~7.95 km/s across it, hardly showing
809   any evidence for a strong mantle anisotropy, which is believed to be an intrinsic feature of the
810   ocean lithosphere formed by seafloor spreading.

811   We prefer to interpret our observation with respect to a model where magmatically
812   starved and tectonically disruptive lithosphere envisioned for transform faults (e.g., Detrick et
813   al., 1993) is magmatically augmented at the proximal ridge-transform intersection before
814   transform crust is turning into a fracture zone. Such a scenario has recently been envisioned to
815   explain the fact that world-wide transform faults are several hundreds of meters deeper than their
816   adjacent fracture zones and is supported by high-resolution bathymetry, showing a phase of
817   accretion at RTIs (Grevemeyer et al., 2021). Marjanović et al. (2020) suggested that this phase of
818   accretion is probably controlled by dyke propagation along the adjacent spreading ridge into the
819   transform fault domain. Therefore, lithosphere found today in the St. Paul FZ has been
820   magmatically overprinted while passing along its eastern RTI, explaining why crust along the St.
821   Paul FZ reflects magmatically accreted lithosphere.

822

823 **Appendix**
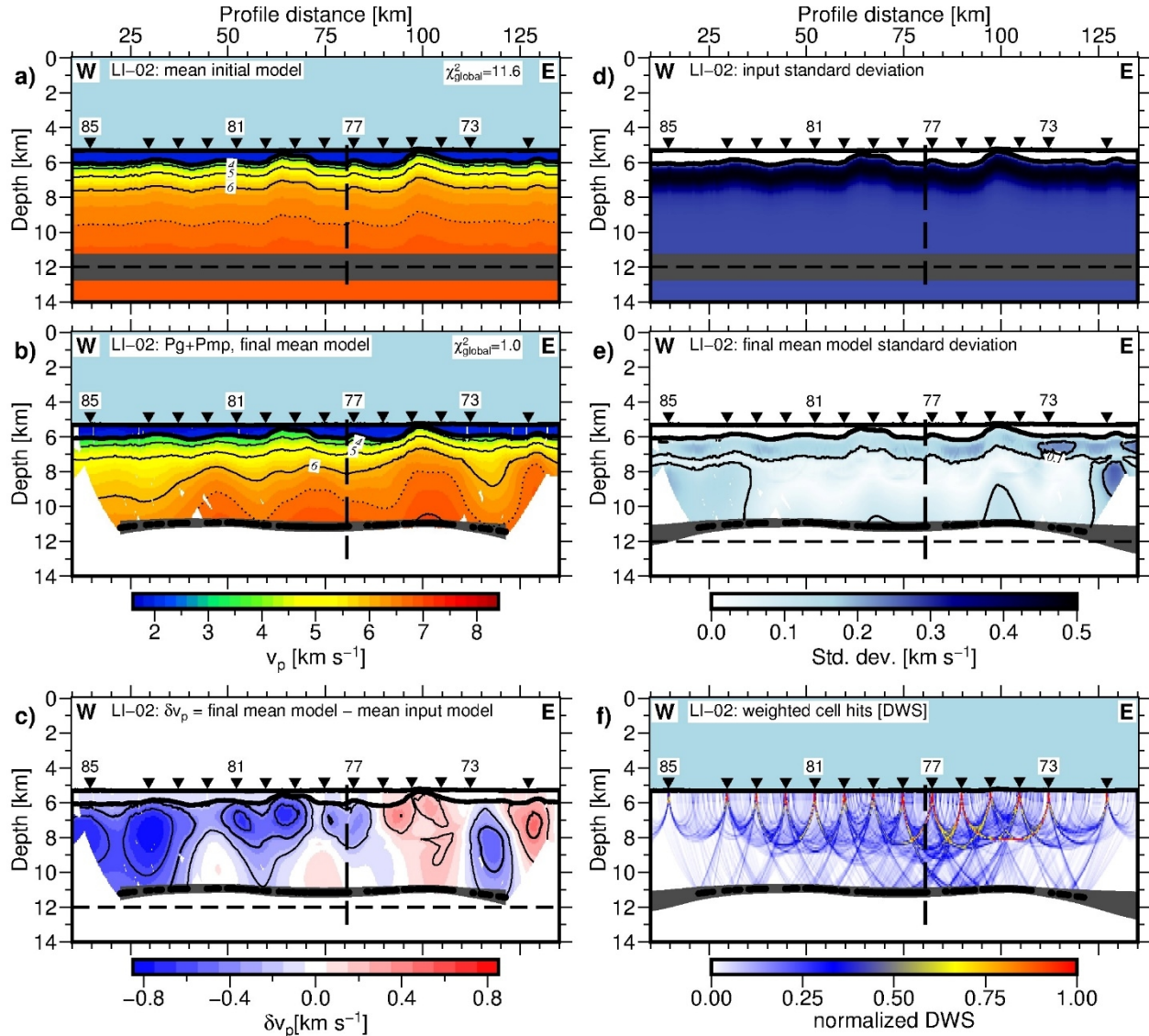
825 **Figure A1:** Results from Monte Carlo analysis for the line LI-02 along St. Paul FZ (Fig. 1c): **(a)** Mean
826 initial crustal velocity model (Grevemeyer et al., 2018). **(b)** Mean final crustal velocity model obtained by
827 cumulative inversion of Pg and PmP arrivals. The velocity contour is 1 km/s starting from 4 km/s. **(c)**
828 Velocity deviation between mean final and mean initial model (final - initial). The contour interval is 0.2
829 km/s starting at 0.2 km/s. **(d)** The initial standard deviation of the mean input velocity model. **(e)** The
830 standard deviation of the final mean model. The contour interval is 0.1 km/s. **(f)** Weighted cell hits (DWS)
831 of the final mean model. Black dots, horizontal black dashed line and grey shading denote the modelled
832 Moho reflection points, the mean initial flat Moho and the Moho standard deviation, respectively. All
833 remaining elements are the same as in Figure 5.
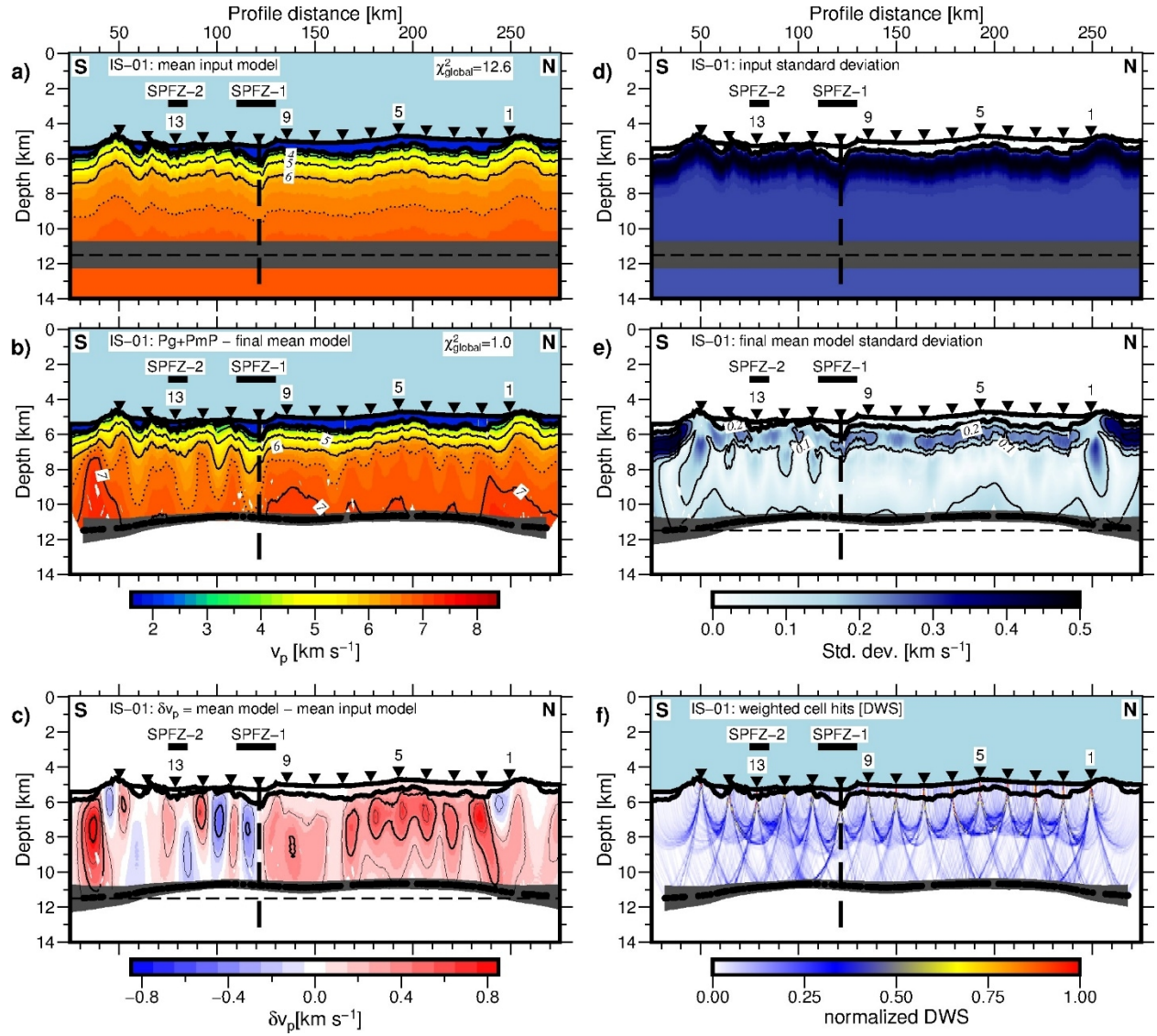
835 **Figure A2:** MCA results for line IS-01 across SPFZ (Fig. 1b): All figure elements are the same as in
836 Figure A1 and Figure 6.

837 **Acknowledgements**

849

850   **References**

851   Ambos, E.L & Hussong D.M. (1986). Oceanographer transform fault structure compared

852   to that of surrounding oceanic crust: Results from seismic refraction data analysis.

853   *Journal of geodynamics*, 5.1, pp. 79–102. https://doi.org/10.1016/0264-

854   3707(86)90024-4

855

856   Bell, R. E., & Buck, W. R. (1992). Crustal control of ridge segmentation inferred from

857   observations of the Reykjanes Ridge. Nature, 357, 583–586.

858   https://doi.org/10.1038/357583a0

859

860   Bird, P. (2003). "An updated digital model of plate boundaries". *Geochemistry,*

861   *Geophysics, Geosystems,* 4.3. https://doi.org/10.1029/2001GC000252

862

863   Bonatti, E.,Seyler, M., & Sushevskaya, N. (1993)., A cold suboceanic mantle belt at the

864   Earth equator. *Science* 261, 315-320. https://doi.org/10.1126/science.261.5119.315

865

866   Cannat, M. (1993). Emplacement of mantle rocks in the seafloor at mid-ocean ridges,

867   *Journal of Geophysical Research*, 98, 4163-4172. https://doi.org/10.1029/92JB02221

868

869 Cannat, M., Mevel, C., Maia, M., Deplus, C., Durand, C., Gente, P., Agrinier, P.,
870   Belarouchi, A., Dubuisson, G., Humler, E., & Reynolds, J.(1995). Thin crust,
871   ultramafic exposures, and rugged faulting patterns at the Mid-Atlantic Ridge (22–24°
872   N), *Geology* 23, 49-52. https://doi.org/10.1130/0091-
873   7613(1995)023<0049:TCUEAR>2.3.CO;2

874

875 Carlson, R. L., & Miller, D. J. (2004). Influence of pressure and mineralogy on seismic
876   velocities in oceanic gabbros: Implications for the composition and state of the lower
877   oceanic crust, *Journal of Geophysical Research*, 109, B09205.
878   https://doi.org/10.1029/2003JB002699

879

880 Calvert, A.J., & Potts, C.G. (1985). Seismic evidence for hydrothermally altered mantle
881   beneath old crust in the Tydeman fracture zone. *Earth and Planetary Science Letters,*
882   75.4, pp. 439–449. https://doi.org/10.1016/0012-821X(85)90187-6

883

884 Canales, J. P., Detrick, R. S., Lin, J., Collins, J. A., & Toomey, D. R. (2000). Crustal and
885   upper mantle seismic structure beneath the rift mountains and across a nontransform
886   offset at the Mid-Atlantic Ridge (35 N). *Journal of Geophysical Research: Solid Earth*,
887   *105*(B2), 2699-2719. https://doi.org/10.1029/1999JB900379

888

889 Chen, Y. J. (1992). Oceanic crustal thickness versus spreading rate. *Geophysical Research*
890   *Letters*, *19*(8), 753-756. https://doi.org/10.1029/92GL00161

891

892 Christeson, G. L., Goff, J. A., & Reece, R. S. (2019). Synthesis of oceanic crustal structure
893   from two-dimensional seismic profiles. *Reviews of Geophysics*, 57, 504–529.
894   https://doi.org/10.1029/2019RG000641

895

896 Christeson, G. L., Reece, R. S., Kardell, D. A., Estep, J. D., Fedotova, A., & Goff, J. A.
897   (2020). South Atlantic Transect: Variations in Oceanic Crustal Structure at 31° S.
898   *Geochemistry, Geophysics, Geosystems*, *21*(7), e2020GC009017.
899   https://doi.org/10.1029/2020GC009017

901 Cohen, J.K. , Stockwell, J.W. (2010). CWP/SU: Seismic Unix Release 41: A free package
902   for seismic research and processing: Center for Wave Phenomena, Colorado School of
903   Mines. Available online at https://wiki.seismic-unix.org/

905 Cormier, M. H., Detrick, R. S., & Purdy, G. M. (1984). Anomalously thin crust in oceanic
906   fracture zones: New seismic constraints from the Kane fracture zone. *Journal of*
907   *Geophysical Research: Solid Earth*, *89*(B12), 10249-10266.
908   https://doi.org/10.1029/JB089iB12p10249

910 Creager, K. C., & Dorman, L. M. (1982). Location of instruments on the seafloor by joint
911   adjustment of instrument and ship positions. *Journal of Geophysical Research: Solid*
912   *Earth*, *87*(B10), 8379-8388. https://doi.org/10.1029/JB087iB10p08379

914 Dalton, C. A., Langmuir, C. H., & Gale, A. (2014). Geophysical and geochemical
915   evidence for deep temperature variations beneath mid-ocean ridges. *Science*,
916   *344*(6179), 80-83. https://www.doi.org/10.1126/science.1249466

918 Dannowski, A., Grevemeyer, I., Phipps Morgan, J., Ranero, C. R., Maia, M., & Klein, G.
919   (2011). Crustal structure of the propagating TAMMAR ridge segment on the Mid-
920   Atlantic Ridge, 21.5 N. *Geochemistry, Geophysics, Geosystems*, *12*(7).
921   https://doi.org/10.1029/2011GC003534

923   Dannowski, A., Morgan, J. P., Grevemeyer, I., & Ranero, C. R. (2018). Enhanced mantle
924   upwelling/melting caused segment propagation, oceanic core complex die off, and the
925   death of a transform fault: The Mid-Atlantic Ridge at 21.5 N. *Journal of Geophysical*
926   *Research: Solid Earth*, *123*(2), 941-956. https://doi.org/10.1002/2017JB014273

927

928   Davy, R. G., Collier, J. S., Henstock, T. J., VoiLA Consortium, Rietbrock, A., Goes, S., et
929   al. (2020). Wide-angle seismic imaging of two modes of crustal accretion in mature
930   Atlantic Ocean crust. *Journal of Geophysical Research: Solid Earth*, *125*(6),
931   e2019JB019100. https://doi.org/10.1029/2019JB019100

932

933   de Melo, G. W., Parnell-Turner, R., Dziak, R. P., Smith, D. K., Maia, M., do Nascimento,
934   A. F., & Royer, J. Y. (2021). Uppermost Mantle Velocity beneath the Mid-Atlantic
935   Ridge and Transform Faults in the Equatorial Atlantic Ocean. *Bulletin of the*
936   *Seismological Society of America*, *111*(2), 1067-1079.
937   https://doi.org/10.1785/0120200248

938

939   Detrick Jr, R. S., & Purdy, G. M. (1980). The crustal structure of the Kane fracture zone
940   from seismic refraction studies. *Journal of Geophysical Research: Solid Earth*, *85*(B7),
941   3759-3777. https://doi.org/10.1029/JB085iB07p03759

942

943   Detrick, R. S., Cormier, M. H., Prince, R. A., Forsyth, D. W., & Ambos, E. L. (1982).
944   Seismic constraints on the crustal structure within the Vema fracture zone. *Journal of*
945   *Geophysical Research: Solid Earth*, *87*(B13), 10599-10612.
946   https://doi.org/10.1029/JB087iB13p10599

947

948   Detrick, R. S., White, R. S., & Purdy, G. M. (1993). Crustal structure of North Atlantic
949   fracture zones. *Reviews of Geophysics*, *31*(4), 439-458.
950   https://doi.org/10.1029/93RG01952

951

952 Dunn, R. A., & Toomey, D. R. (1997). Seismological evidence for three-dimensional melt

953 migration beneath the East Pacific Rise. *Nature*, *388*(6639), 259-262.

954 https://doi.org/10.1038/40831

955

956 Dunn, R. A., & Toomey, D. R. (2001). Crack-induced seismic anisotropy in the oceanic

957 crust across the East Pacific Rise (9 30′ N). *Earth and Planetary Science Letters*,

958 *189*(1-2), 9-17. https://doi.org/10.1016/S0012-821X(01)00353-3

959

960 Dunn, R. A., Toomey, D. R., & Solomon, S. C. (2000). Three-dimensional seismic

961 structure and physical properties of the crust and shallow mantle beneath the East

962 Pacific Rise at 9° 30'N. *Journal of Geophysical Research: Solid Earth*, *105*(B10),

963 23537-23555. https://doi.org/10.1029/2000JB900210

964

965 Gaherty, J. B., Lizarralde, D., Collins, J. A., Hirth, G., & Kim, S. (2004). Mantle

966 deformation during slow seafloor spreading constrained by observations of seismic

967 anisotropy in the western Atlantic. *Earth and Planetary Science Letters*, *228*(3-4), 255-

968 265. https://doi.org/10.1016/j.epsl.2004.10.026

969

970 Gregory, E., Singh, S. C., Marjanović, M., & Wang, Z. (2021). Serpentinized peridotite

971 versus thick mafic crust at the Romanche oceanic transform fault, *Geology,* 49 (9):

972 1132–1136. https://doi.org/10.1130/G49097.1

973

974 Grevemeyer, I. (2020). Upper Mantle Structure beneath the Mid-Atlantic Ridge from

975 Regional Waveform Modeling. *Bulletin of the Seismological Society of America*,

976 *110*(1), 18-25. https://doi.org/10.1785/0120190080

977

978   Grevemeyer, I., Kaul, N., Villinger, H., & Weigel, W. (1999). Hydrothermal activity and
979   the evolution of the seismic properties of upper oceanic crust. *Journal of Geophysical*
980   *Research: Solid Earth*, *104*(B3), 5069-5079. https://doi.org/10.1029/1998JB900096

981

982   Grevemeyer, I., Ranero, C. R., & Ivandic, M. (2018). Structure of oceanic crust and
983   serpentinization at subduction trenches. *Geosphere*, *14*(2), 395-418.
984   https://doi.org/10.1130/GES01537.1

985

986   Grevemeyer, I., Rüpke, L.H., Morgan, J.P., Iyer, K, & Devey, C.W. (2021). Extensional
987   tectonics and two-stage crustal accretion at oceanic transform faults. *Nature,* 591, 402–
988   407. https://doi.org/10.1038/s41586-021-03278-9

989

990   Grevemeyer, I., Singh, S.C., Papenberg, C. (2019). Ocean bottom seismometer and ocean
991   bottom hydrophone seismic refraction and wide angle data from profile P02 of Maria
992   S. Merian cruise MSM69 with links to sgy data files. PANGAEA.
993   https://doi.org/10.1594/PANGAEA.907944

994

995   Grion, S., Exley, R., Manin, M., Miao, X., Pica, A. L., Wang, Y., et al. (2007). Mirror
996   imaging of OBS data. *first break*, *25*(11). https://doi.org/10.3997/1365-2397.2007028

997

998   Harding, J. L., Van Avendonk, H. J., Hayman, N. W., Grevemeyer, I., Peirce, C., &
999   Dannowski, A. (2017). Magmatic-tectonic conditions for hydrothermal venting on an
1000   ultraslow-spread oceanic core complex. *Geology*, *45*(9), 839-842.
1001   https://doi.org/10.1130/G39045.1

1002

1003   Hooft, E. E. E., Detrick, R. S., Toomey, D. R., Collins, J. A., & Lin, J. (2000). Crustal
1004   thickness and structure along three contrasting spreading segments of the Mid-Atlantic

Ridge, 33.5–35 N. *Journal of Geophysical Research: Solid Earth*, *105*(B4), 8205-8226. https://doi.org/10.1029/1999JB900442

James, E. K., Dalton, C. A., & Gaherty, J. B. (2014). R ayleigh wave phase velocities in the A tlantic upper mantle. *Geochemistry, Geophysics, Geosystems*, *15*(11), 4305-4324. https://doi.org/10.1002/2014GC005518

Korenaga, J., Holbrook, W. S., Kent, G. M., Kelemen, P. B., Detrick, R. S., Larsen, H. C., et al. (2000). Crustal structure of the southeast Greenland margin from joint refraction and reflection seismic tomography. *Journal of Geophysical Research: Solid Earth*, *105*(B9), 21591-21614. https://doi.org/10.1029/2000JB900188

Korenaga, J., Kelemen, P. B., & Holbrook, W. S. (2002). Methods for resolving the origin of large igneous provinces from crustal seismology. *Journal of Geophysical Research: Solid Earth*, *107*(B9), ECV-1. https://doi.org/10.1029/2001JB001030

Lin, J., Purdy, G. M., Schouten, H., Sempere, J. C., & Zervas, C. (1990). Evidence from gravity data for focusedmagmatic accretionalong the Mid-Atlantic Ridge. *Nature*, *344*(6267), 627-632. https://doi.org/10.1038/344627a0

Lin, J., & Morgan, J. P. (1992). The spreading rate dependence of three-dimensional mid-ocean ridge gravity structure. *Geophysical Research Letters*, *19*(1), 13-16. https://doi.org/10.1029/91GL03041

Macdonald, K. C., Fox, P. J., Perram, L. J., Eisen, M. F., Haymon, R. M., Miller, S. P., et al. (1988). A new view of the mid-ocean ridge from the behaviour of ridge-axis discontinuities. *Nature*, *335*(6187), 217-225. https://doi.org/10.1038/335217a0

1032

1033 Maia, M., Sichel, S., Briais, A., Brunelli, D., Ligi, M., Ferreira, N., et al. (2016). Extreme
1034   mantle uplift and exhumation along a transpressive transform fault. *Nature Geoscience*,
1035   *9*(8), 619-623. https://doi.org/10.1038/ngeo2759

1036

1037 Marjanović, M., Singh, S. C., Gregory, E. P., Grevemeyer, I., Growe, K., Wang, Z., et al.
1038   (2020). Seismic crustal structure and morphotectonic features associated with the
1039   Chain Fracture Zone and their role in the evolution of the equatorial Atlantic region.
1040   *Journal of Geophysical Research: Solid Earth*, *125*(10), e2020JB020275.
1041   https://doi.org/10.1029/2020JB020275

1042

1043 Matthews, K. J., Müller, R. D., Wessel, P., & Whittaker, J. M. (2011). The tectonic fabric
1044   of the ocean basins. *Journal of Geophysical Research: Solid Earth*, *116*(B12).
1045   https://doi.org/10.1029/2011JB008413

1046

1047 McKenzie, D. P., & Parker, R. L. (1967). The North Pacific: an example of tectonics on a
1048   sphere. *Nature*, *216*(5122), 1276-1280. https://doi.org/10.1038/2161276a0

1049

1050 Mckenzie, D. A. N., & Bickle, M. J. (1988). The volume and composition of melt
1051   generated by extension of the lithosphere. *Journal of petrology*, *29*(3), 625-679.
1052   https://doi.org/10.1093/petrology/29.3.625

1053

1054 Mehouachi, F., & Singh, S. C. (2018). Water-rich sublithospheric melt channel in the
1055   equatorial Atlantic Ocean. *Nature Geoscience*, *11*(1), 65-69.
1056   https://doi.org/10.1038/s41561-017-0034-z

1057

1058 Menard, H. W. (1967). Extension of northeastern-Pacific fracture zones. *Science*,
1059   *155*(3758), 72-74. https://doi.org/10.1126/science.155.3758.72

1060

1061 Menard, H. W. (1955). Deformation of the northeastern Pacific basin and the west coast of
1062   North America. *Geological Society of America Bulletin*, *66*(9), 1149-1198.
1063   https://doi.org/10.1130/0016-7606(1955)66[1149:DOTNPB]2.0.CO;2

1064

1065 Minshull, T. A., White, R. S., Mutter, J. C., Buhl, P., Detrick, R. S., Williams, C. A., &
1066   Morris, E. (1991). Crustal structure at the Blake Spur fracture zone from expanding
1067   spread profiles. *Journal of Geophysical Research: Solid Earth*, *96*(B6), 9955-9984.
1068   https://doi.org/10.1029/91JB00431

1069

1070 Morgan, W. J. (1968). Rises, trenches, great faults, and crustal blocks. *Journal of
1071   Geophysical Research*, *73*(6), 1959-1982. https://doi.org/10.1029/JB073i006p01959

1072

1073 Morgan, J. P., & Parmentier, E. M. (1984). Lithospheric stress near a ridge-transform
1074   intersection. *Geophysical Research Letters*, *11*(2), 113-116.
1075   https://doi.org/10.1029/GL011i002p00113

1076

1077 Moser, T. J. (1991). Shortest path calculation of seismic rays. *Geophysics*, *56*(1), 59-67.
1078   https://doi.org/10.1190/1.1442958

1079

1080 Moser, T. J., Nolet, G., & Snieder, R. (1992). Ray bending revisited. *Bulletin of the
1081   Seismological Society of America*, *82*(1), 259-288.

1082

1083 Müller, R. D., Sdrolias, M., Gaina, C., & Roest, W. R. (2008). Age, spreading rates, and
1084   spreading asymmetry of the world's ocean crust. *Geochemistry, Geophysics,
1085   Geosystems*, *9*(4). https://doi.org/10.1029/2007GC001743

1086

1087   Muller, M. R., Minshull, T. A., & White, R. S. (1999). Segmentation and melt supply at

1088   the Southwest Indian Ridge. *Geology*, *27*(10), 867-870. https://doi.org/10.1130/0091-

1089   7613(1999)027<0867:SAMSAT>2.3.CO;2

1090

1091   Niu, X., Ruan, A., Li, J., Minshull, T. A., Sauter, D., Wu, Z., et al. (2015). Along-axis

1092   variation in crustal thickness at the ultraslow spreading S outhwest I ndian R idge (50°

1093   E) from a wide-angle seismic experiment. *Geochemistry, Geophysics, Geosystems*,

1094   *16*(2), 468-485. https://doi.org/10.1002/2014GC005645

1095

1096   Paige, C. C., & Saunders, M. A. (1982). LSQR: An algorithm for sparse linear equations

1097   and sparse least squares. *ACM Transactions on Mathematical Software (TOMS)*, *8*(1),

1098   43-71.

1099

1100   Peirce, C., Reveley, G., Robinson, A. H., Funnell, M. J., Searle, R. C., Simão, N. M., et al.

1101   (2019). Constraints on crustal structure of adjacent OCCs and segment boundaries at

1102   13° N on the Mid-Atlantic Ridge. *Geophysical Journal International*, *217*(2), 988-

1103   1010. https://doi.org/10.1093/gji/ggz074

1104

1105   Planert, L., Flueh, E. R., & Reston, T. J. (2009). Along-and across-axis variations in

1106   crustal thickness and structure at the Mid-Atlantic Ridge at 5 S obtained from wide-

1107   angle seismic tomography: Implications for ridge segmentation. *Journal of*

1108   *Geophysical Research: Solid Earth*, *114*(B9). https://doi.org/10.1029/2008JB006103

1109

1110   Potts, C. G., Calvert, A. J., & White, R. S. (1986). Crustal structure of Atlantic fracture

1111   zones-III. The Tydeman fracture zone. *Geophysical Journal International*, *86*(3), 909-

1112   942. https://doi.org/10.1111/j.1365-246X.1986.tb00668.x

1113

1114 Purdy, G. M. (1983). The seismic structure of 140 Myr old crust in the western central
1115   Atlantic Ocean. *Geophysical Journal International*, *72*(1), 115-137.
1116   https://doi.org/10.1111/j.1365-246X.1983.tb02808.x

1117

1118 Raitt, M. (1963). The crustal rocks. *The sea*, *3*, 85-102.

1119

1120 Roland, E., Lizarralde, D., McGuire, J. J., & Collins, J. A. (2012). Seismic velocity
1121   constraints on the material properties that control earthquake behavior at the Quebrada-
1122   Discovery-Gofar transform faults, East Pacific Rise. *Journal of Geophysical Research:*
1123   *Solid Earth*, *117*(B11). https://doi.org/10.1029/2012JB009422

1124

1125 Sandwell, D. T. (1984). Thermomechanical evolution of oceanic fracture zones. *Journal of*
1126   *Geophysical Research: Solid Earth*, *89*(B13), 11401-11413.
1127   https://doi.org/10.1029/JB089iB13p11401

1128

1129 Sandwell, D. T., Müller, R. D., Smith, W. H., Garcia, E., & Francis, R. (2014). New global
1130   marine gravity model from CryoSat-2 and Jason-1 reveals buried tectonic structure.
1131   *Science*, *346*(6205), 65-67. https://doi.org/10.1126/science.1258213

1132

1133 Searle, R. C., Thomas, M. V., & Jones, E. J. W. (1994). Morphology and tectonics of the
1134   Romanche Transform and its environs. *Marine Geophysical Researches*, *16*(6), 427-
1135   453. https://doi.org/10.1007/BF01270518

1136

1137 Sykes, L. R. (1967). Mechanism of earthquakes and nature of faulting on the mid-oceanic
1138   ridges. *Journal of Geophysical Research*, *72*(8), 2131-2153.
1139   https://doi.org/10.1029/JZ072i008p02131

1140

1141   Taylor, M. A. J., & Singh, S. C. (2002). Composition and microstructure of magma bodies
1142   from effective medium theory. *Geophysical Journal International*, *149*(1), 15-21.
1143   https://doi.org/10.1046/j.1365-246X.2002.01577.x

1144

1145   Tolstoy, M., Harding, A. J., & Orcutt, J. A. (1993). Crustal thickness on the Mid-Atlantic
1146   Ridge: Bull's-eye gravity anomalies and focused accretion. *Science*, *262*(5134), 726-
1147   729. https://doi.org/10.1126/science.262.5134.726

1148

1149   Toomey, D. R., & Foulger, G. R. (1989). Tomographic inversion of local earthquake data
1150   from the Hengill-Grensdalur central volcano complex, Iceland. *Journal of Geophysical*
1151   *Research: Solid Earth*, *94*(B12), 17497-17510.
1152   https://doi.org/10.1029/JB094iB12p17497

1153

1154   Van Avendonk, H. J., Davis, J. K., Harding, J. L., & Lawver, L. A. (2017). Decrease in
1155   oceanic crustal thickness since the breakup of Pangaea. *Nature Geoscience*, *10*(1), 58-
1156   61. https://doi.org/10.1038/ngeo2849

1157

1158   Vaddineni, V. A., Singh, S.C., Grevemeyer, I., Audhkhasi, P., & Papenberg, C. (2021).
1159   Evolution of the Crustal and upper Mantle seismic structure from 0-27 Ma in the
1160   equatorial Atlantic Ocean at 2°43´S. *Journal of Geophysical Research: Solid Earth,*
1161   *e2020JB021390*. https://doi.org/10.1029/2020JB021390

1162

1163   Vine, F. J., & Moores, E. M. (1972). A model for the gross structure, petrology, and
1164   magnetic properties of oceanic crust. *Studies in Earth and Space Sciences: A Memoir*
1165   *in Honor of Harry Hammond Hess*, 195-205.

1166

1167   Wessel, P., Smith, W. H., Scharroo, R., Luis, J., & Wobbe, F. (2013). Generic mapping
1168   tools: improved version released. *Eos, Transactions American Geophysical Union*,
1169   *94*(45), 409-410. https://doi.org/10.1002/2013EO450001

1170

1171   White, R. S., Detrick, R. S., Sinha, M. C., & Cormier, M. H. (1984). Anomalous seismic
1172   crustal structure of oceanic fracture zones. *Geophysical Journal International*, *79*(3),
1173   779-798. https://doi.org/10.1111/j.1365-246X.1984.tb02868.x

1174

1175   White, R. S., McKenzie, D., & O'Nions, R. K. (1992). Oceanic crustal thickness from
1176   seismic measurements and rare earth element inversions. *Journal of Geophysical
1177   Research: Solid Earth*, *97*(B13), 19683-19715. https://doi.org/10.1029/92JB01749

1178

1179   Whitmarsh, R. B. (1978). Seismic refraction studies of the upper igneous crust in the North
1180   Atlantic and porosity estimates for layer 2. *Earth and Planetary Science Letters*, *37*(3),
1181   451-464. https://doi.org/10.1016/0012-821X(78)90061-4

1182

1183   Whitmarsh, R. B., & Calvert, A. J. (1986). Crustal structure of Atlantic fracture zones—I.
1184   The Charlie-Gibbs fracture zone. *Geophysical Journal International*, *85*(1), 107-138.
1185   https://doi.org/10.1111/j.1365-246X.1986.tb05174.x

1186

1187   Wilson, J. T. (1965). A new class of faults and their bearing on continental drift. *Nature*,
1188   *207*(4995), 343-347.

1189

1190   Yilmaz, Ö. (2001). *Seismic data analysis: Processing, inversion, and interpretation of
1191   seismic data*. Society of exploration geophysicists.

Supporting Information for "Seismic structure of the St. Paul Fracture Zone and Late Cretaceous to Mid Eocene oceanic crust in the equatorial Atlantic Ocean near 18°W"

Kevin Growe[1,2], Ingo Grevemeyer[1], Satish Singh[2], Milena Marjanović[2],

Emma P. M. Gregory[2], Cord Papenberg[1], Venkata Vaddineni[2], Laura Gómez

de la Peña[1], and Zhikai Wang[2]

[1]GEOMAR Helmholz Centre for Ocean Research Kiel

[2]Université de Paris, Institut de Physique du Globe de Paris; CNRS, Paris, France

Contents of this file

Introduction

Table S1 lists the acquisition parameters of the two seismic refraction lines used for this study. Figures S1a-S1n and S2a-S2o show all OBS record sections with corresponding traveltime fits and raypaths, for both lines, LI-02 and IS-01, respectively. Figures S3 and S4 illustrate the OBS mirrow image and the post-stack time-migrated MCS sections, that were used to constrain the basement depth below the seafloor for line LI-02 and IS-01,

----

September 18, 2021, 12:34am

respectively. Figure S5 depicts the porosity-velocity-aspect-ratio dependencies computed with a differential effective medium analysis after Taylor and Singh (2002). Figures S6-S15 show the results of several resolution tests for the tomographic inversion: 1. crustal checkerboard tests, 2. Moho regularization tests 3. Moho resolution tests and 4. mantle resolution tests. Their results and implications are briefly discussed in the main text. Table S2 lists all discretization, forward and inversion parametrization used for this study. And finally, Table S3 compares the different parametrization for the PmP inversion.

Table S1. Refraction line acquisition parameters.

Parameter/Line	**LI-02**	**IS-01**
Profile length [km]	143	350
Number of OBS	14	15
Mean OBS-spacing [km]	8.6	14.2
Number of shots	875	1167
Shot spacing [km]	~0.16	0.3
Sampling frequency [Hz]	250	250
Total airgun volume [l]	86	82
Airgun array towing depth [m]	7.5	10
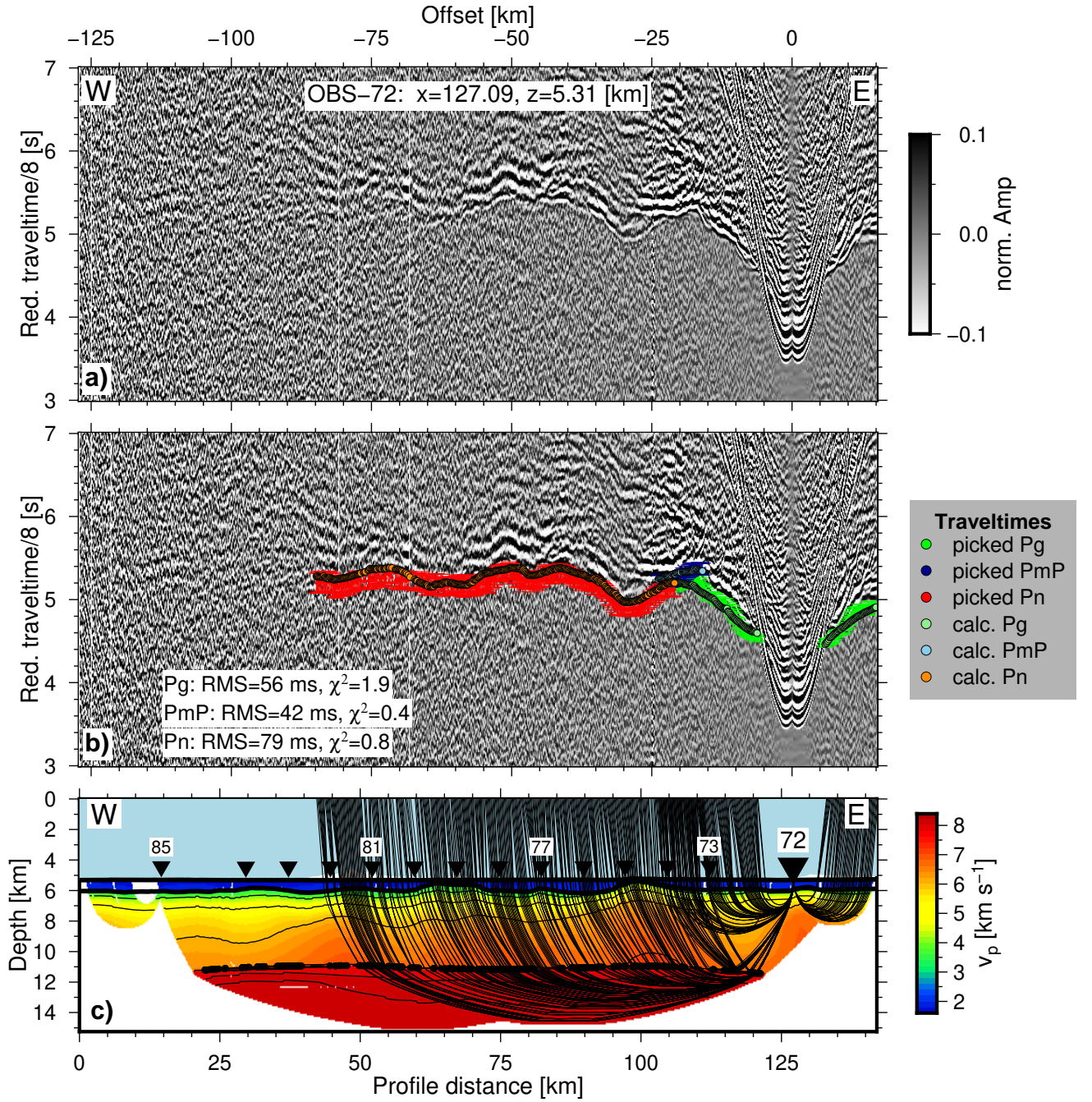
Figure S1a. **(a)** Record section of OBS 72 (LI-02) with **(b)** superimposed picked (small dots with error bars, indicating pick uncertainty) and computed traveltimes (larger dots). The time is reduced with a reduction velocity of 8 km/s. The amplitude is normalized and clipped to 10 %. **(c)** Corresponding raypaths superimposed on final velocity model. The velocity contour interval is 1.0 km/s for the crust, starting with 4 km/s, and 0.1 km/s for the mantle, starting at 8.0 km/s. Remaining figure elements are the same as in Fig. 4 in the main text.
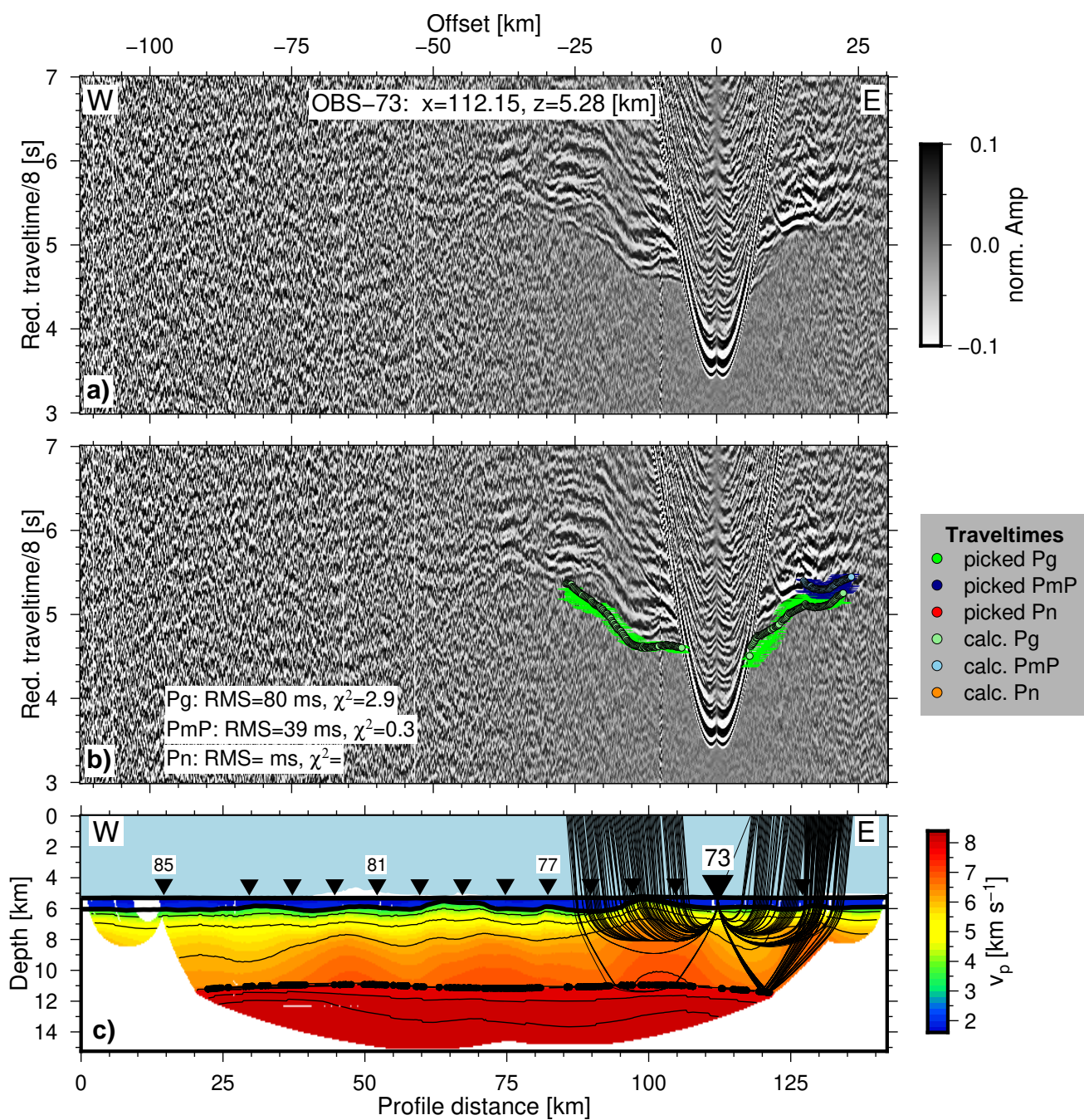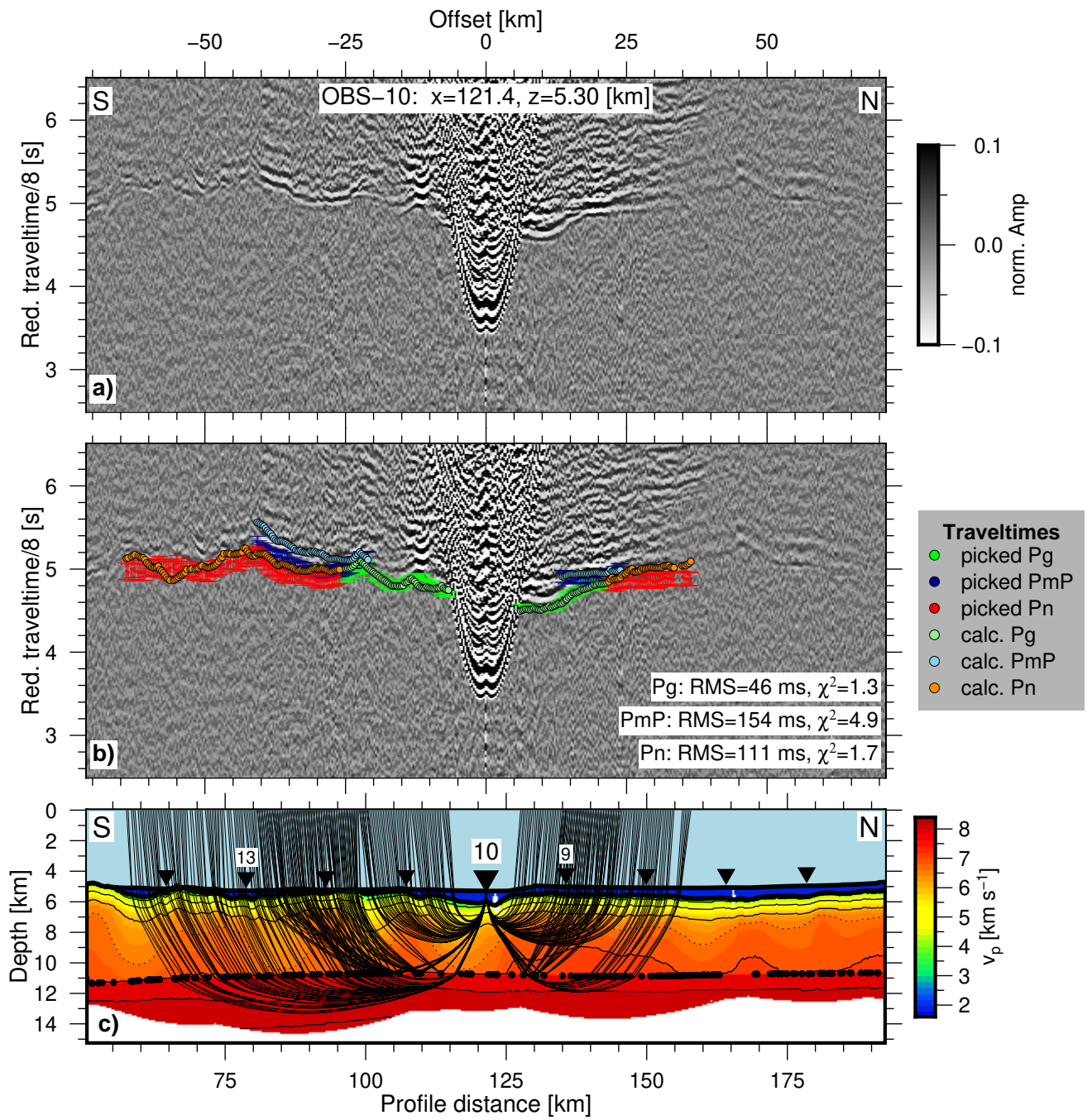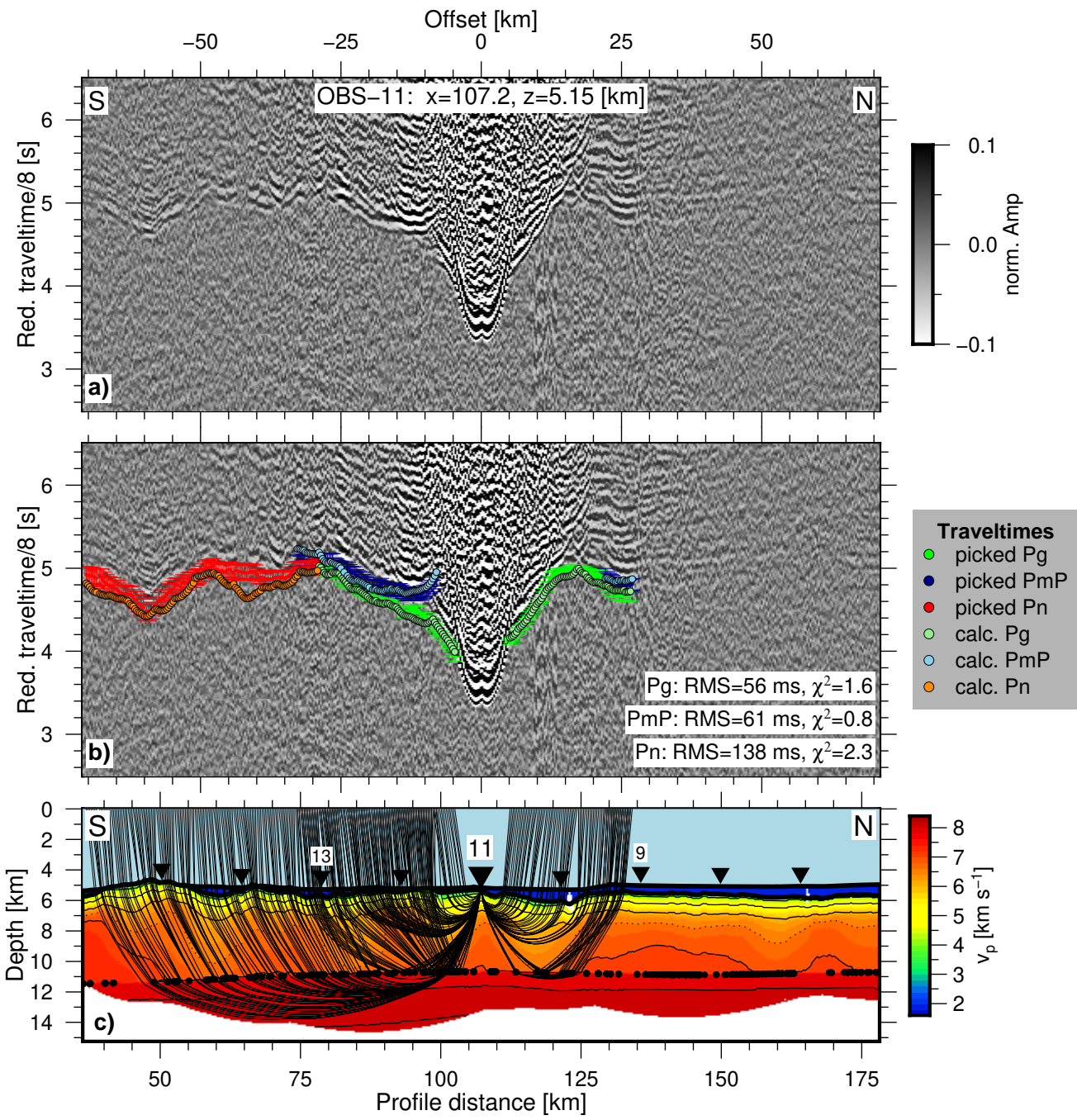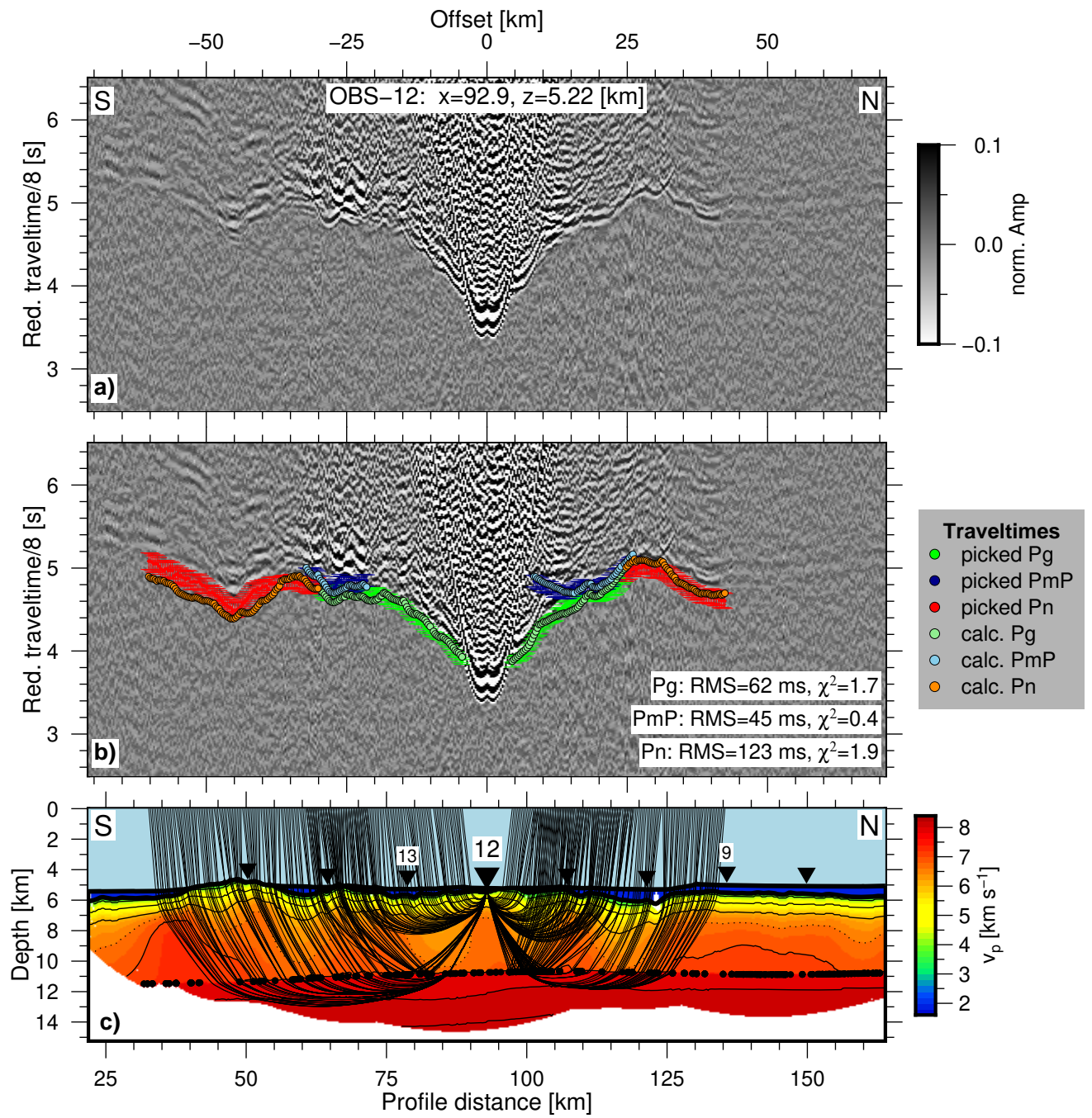
Figure S1b. Record section, traveltime fit and raypaths for OBS 73 (LI-02).
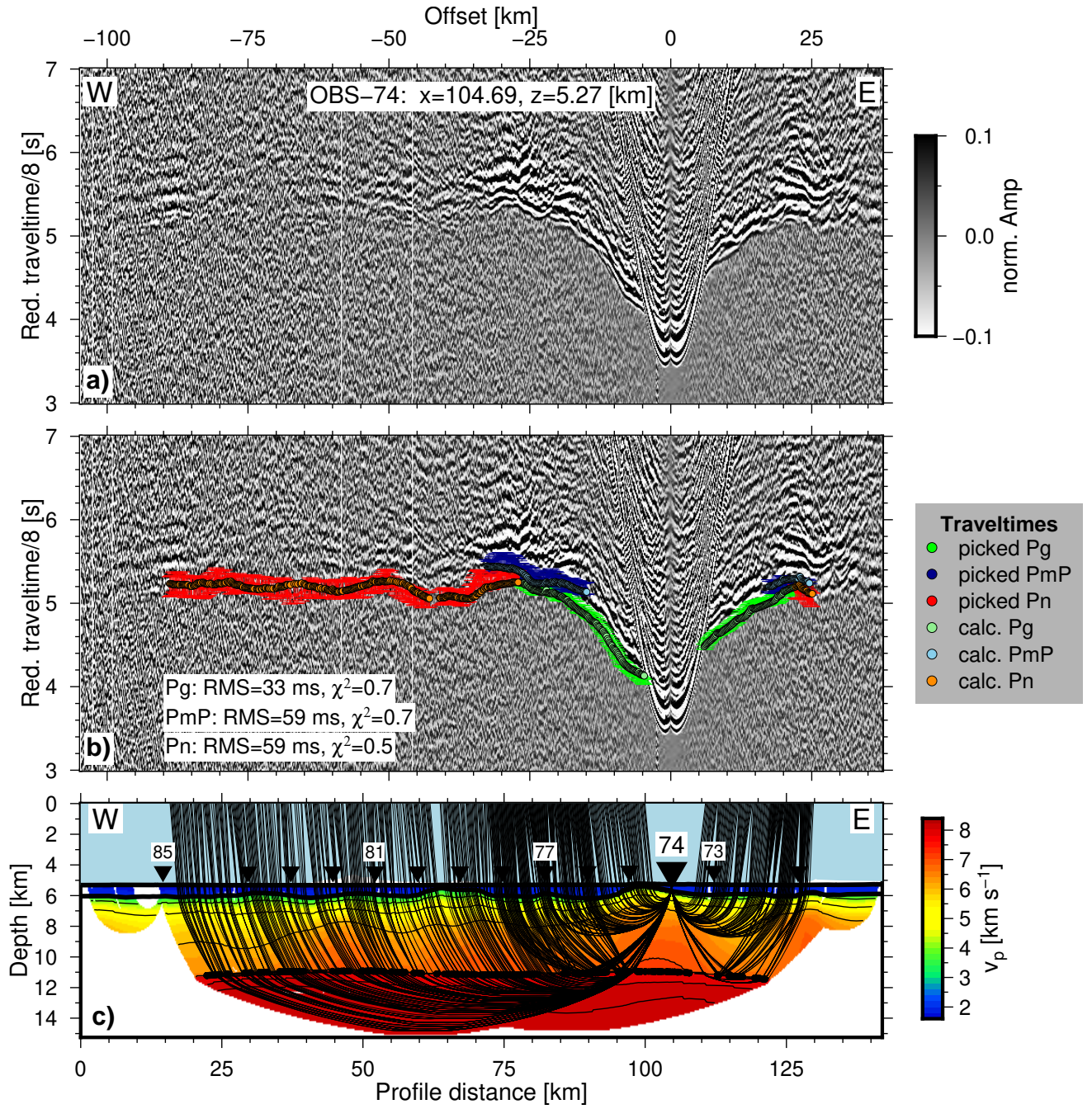
Figure S1c. Record section, traveltime fit and raypaths for OBS 74 (LI-02).
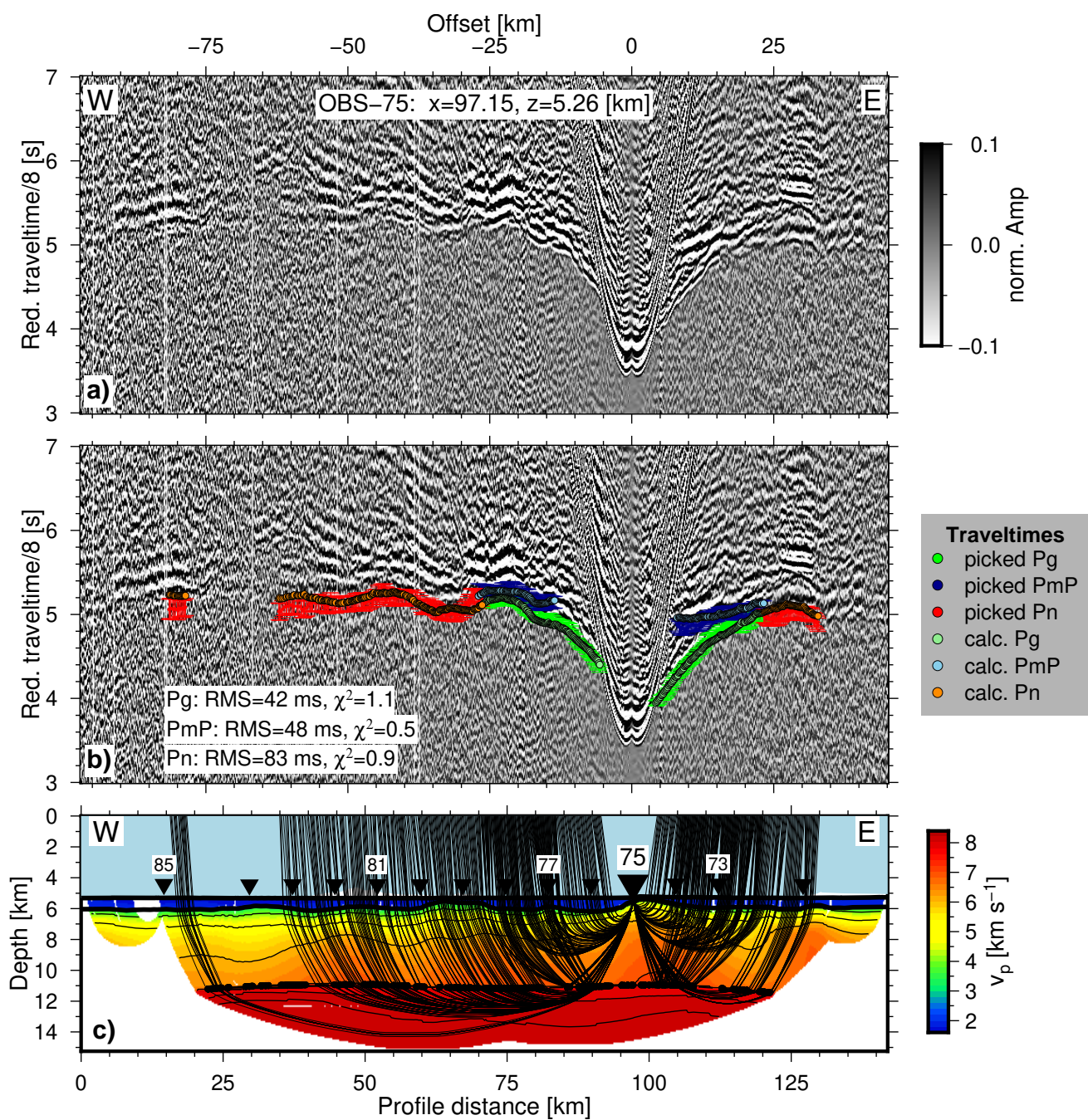
Figure S1d. Record section, traveltime fit and raypaths for OBS 75 (LI-02).

September 18, 2021, 12:34am
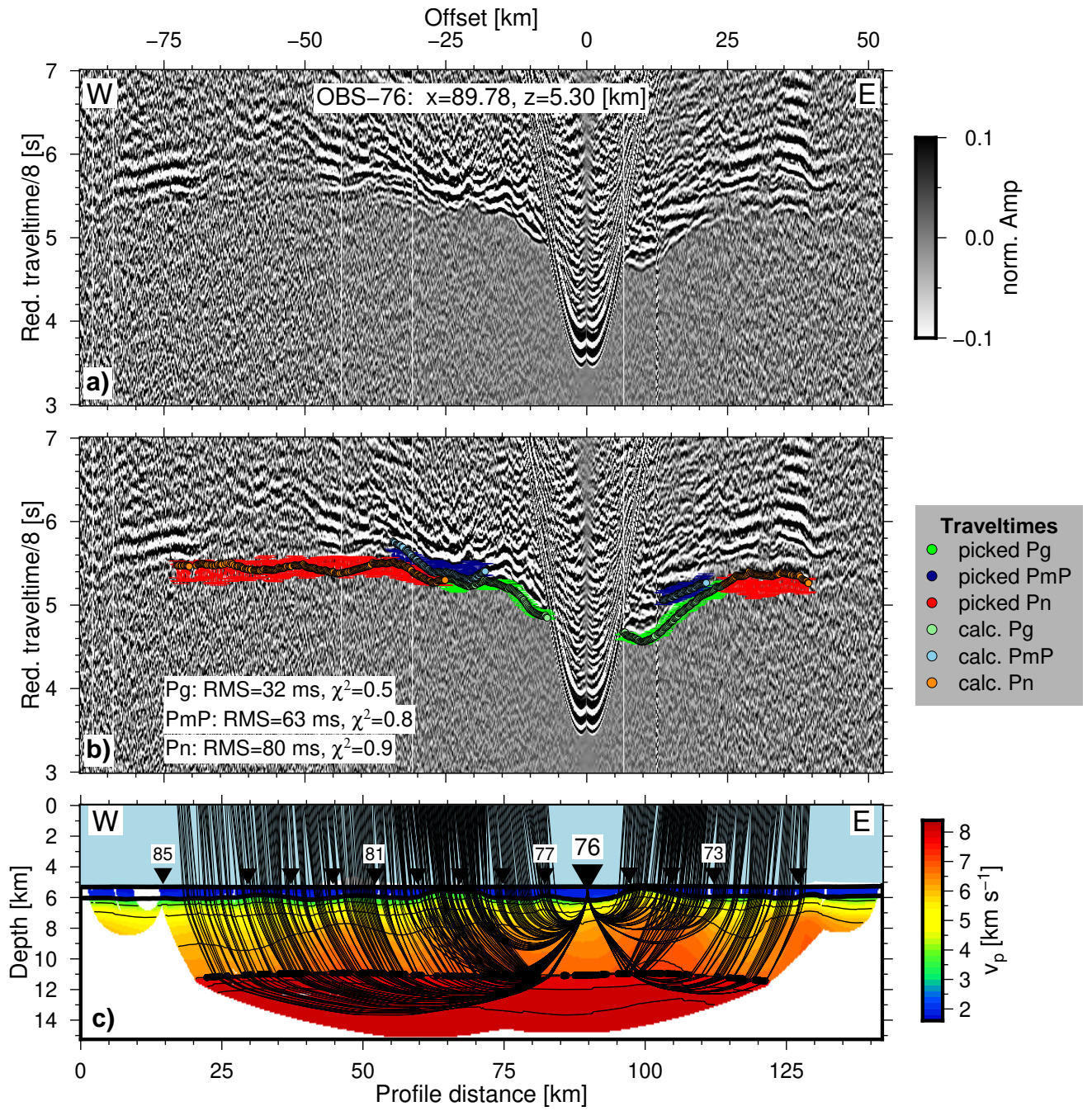
Figure S1e. Record section, traveltime fit and raypaths for OBS 76 (LI-02).
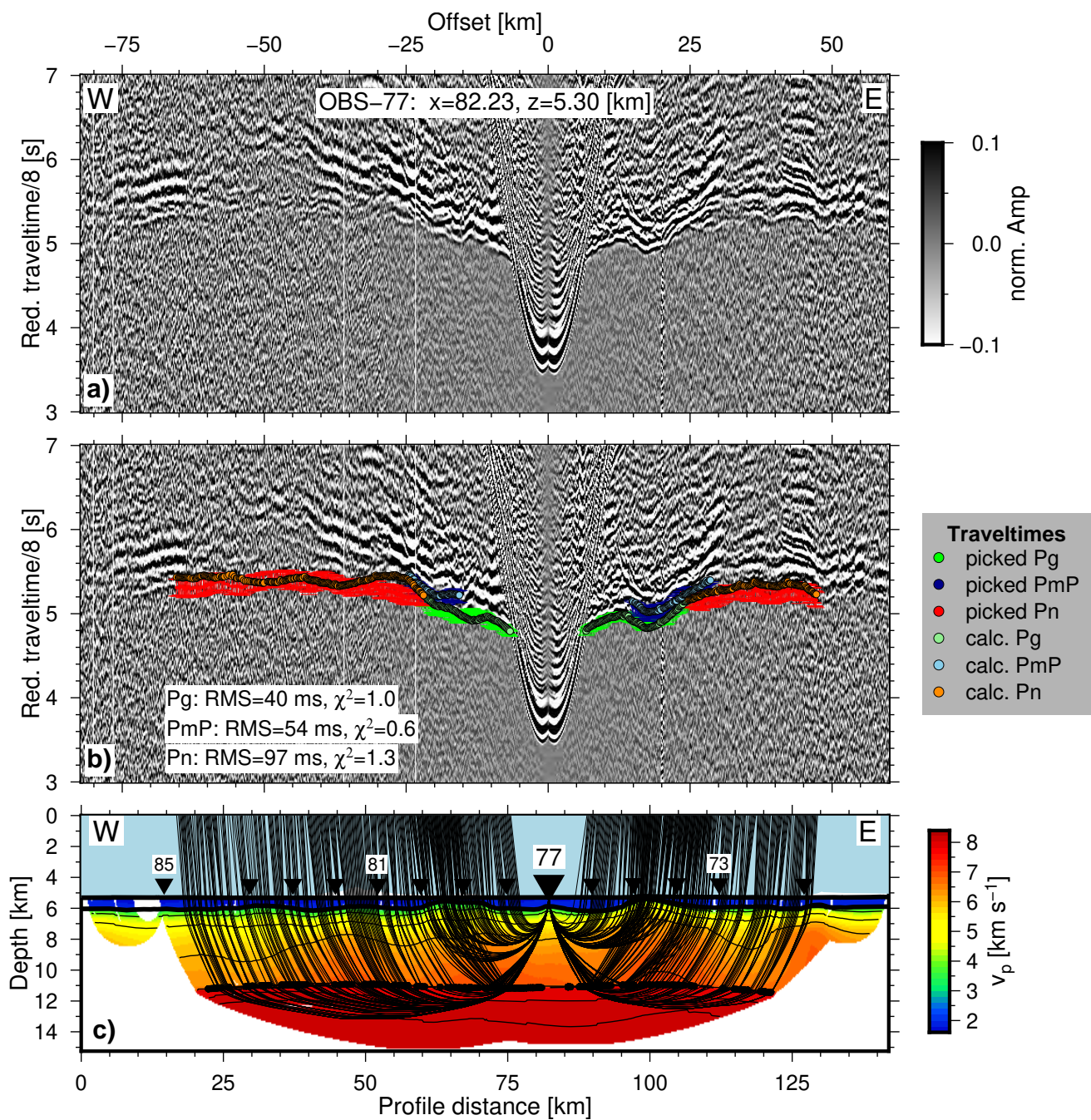
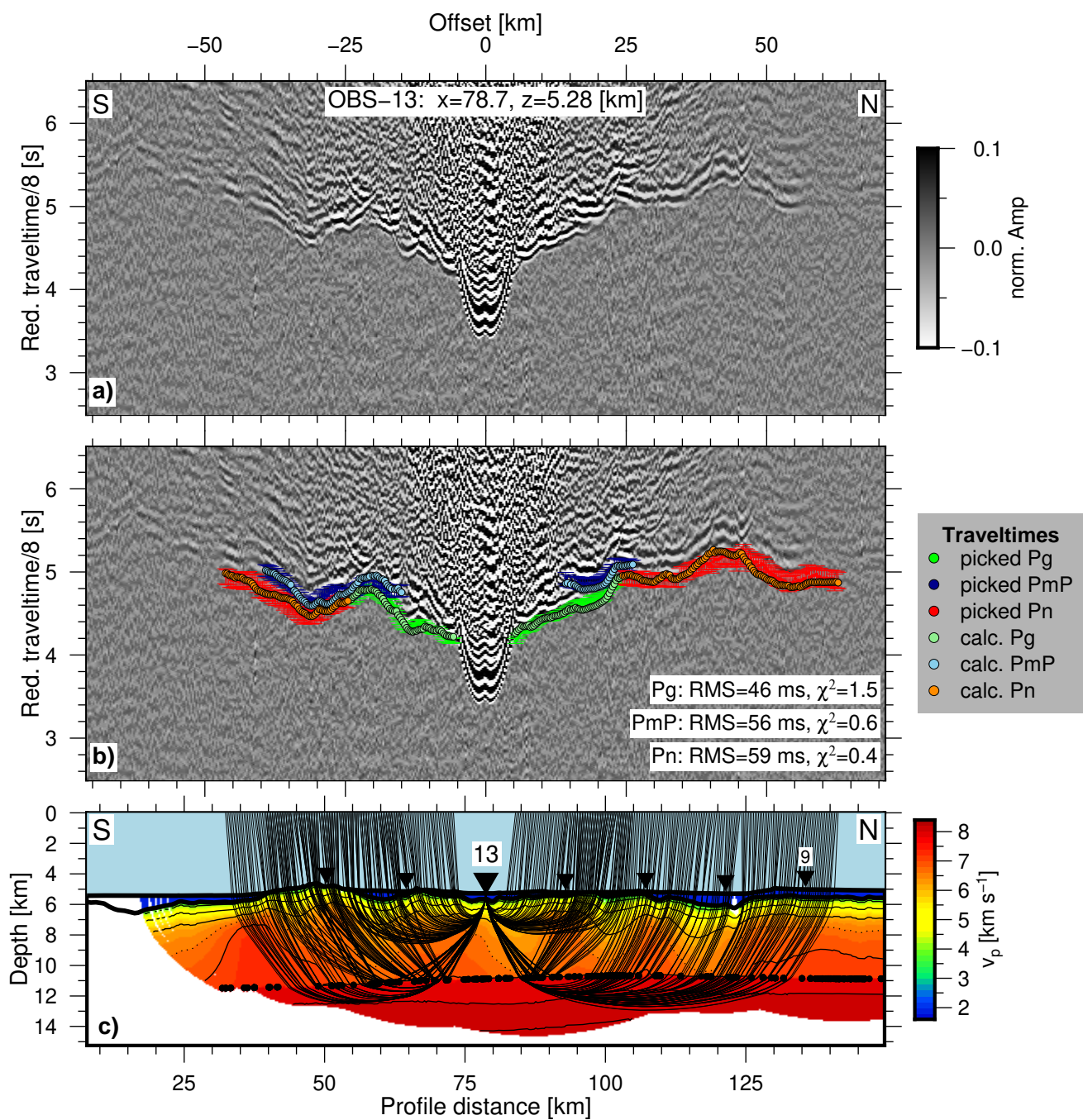**Figure S1f.** Record section, traveltime fit and raypaths for OBS 77 (LI-02).
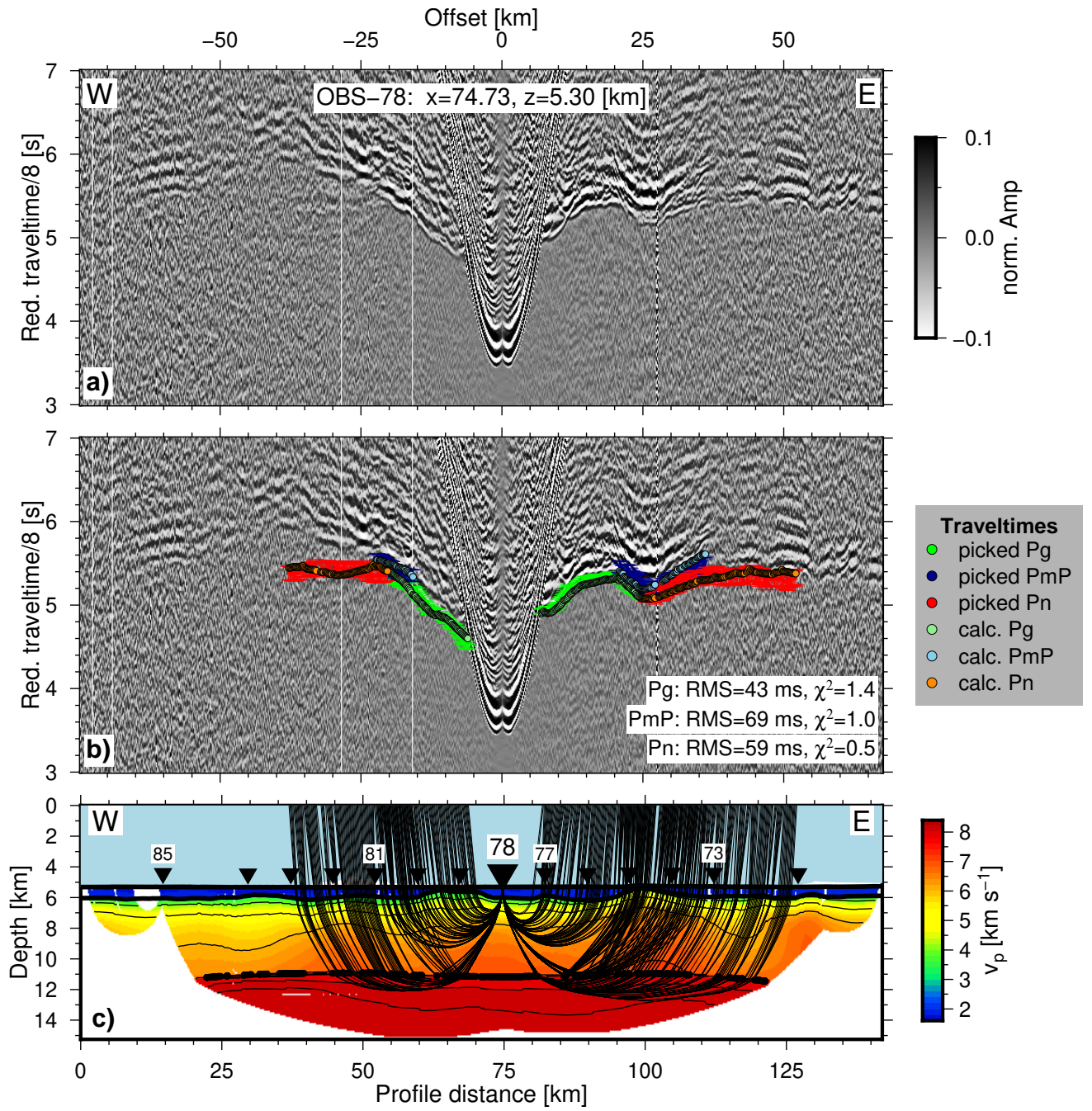
Figure S1g. Record section, traveltime fit and raypaths for OBS 78 (LI-02).
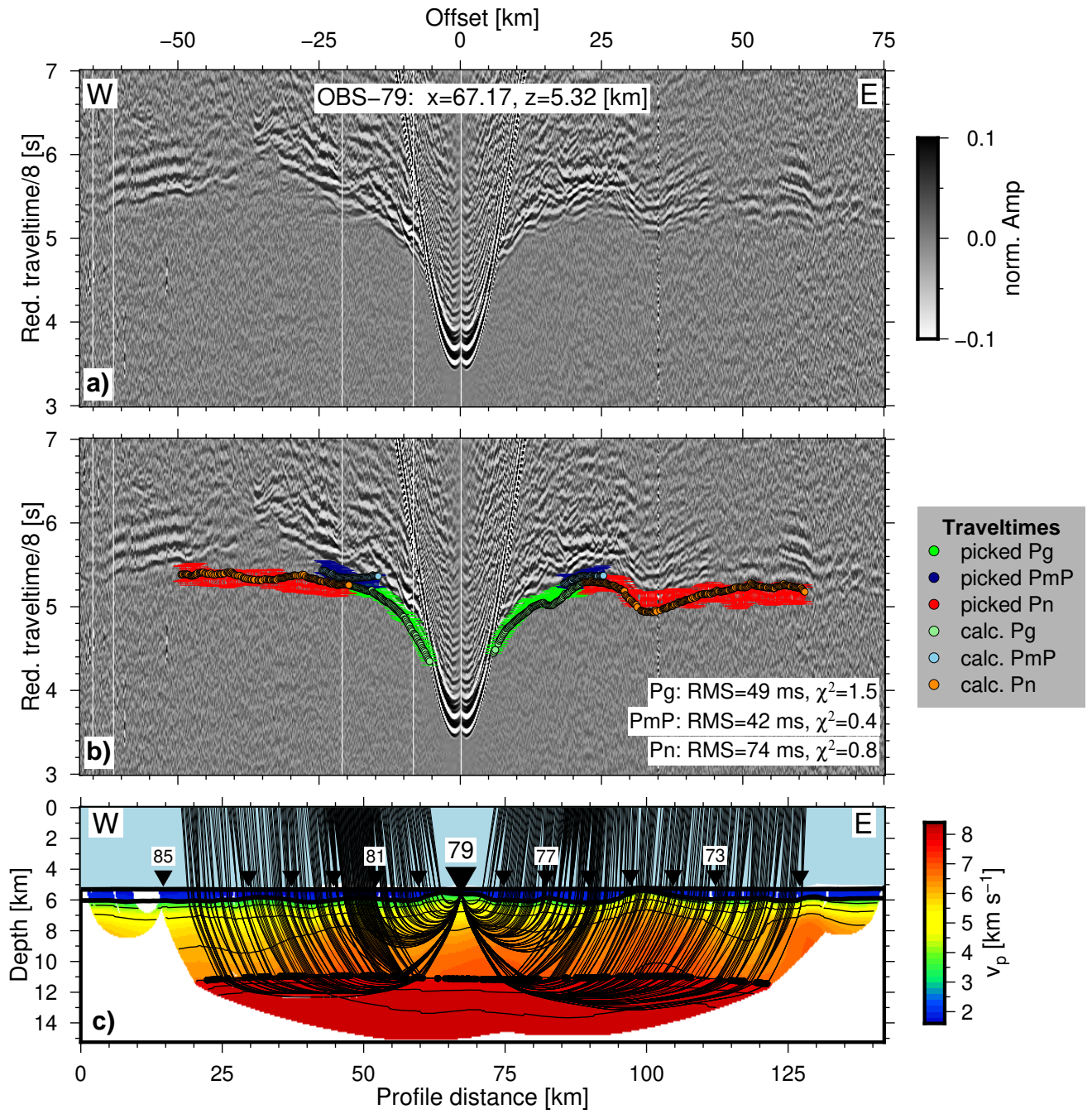
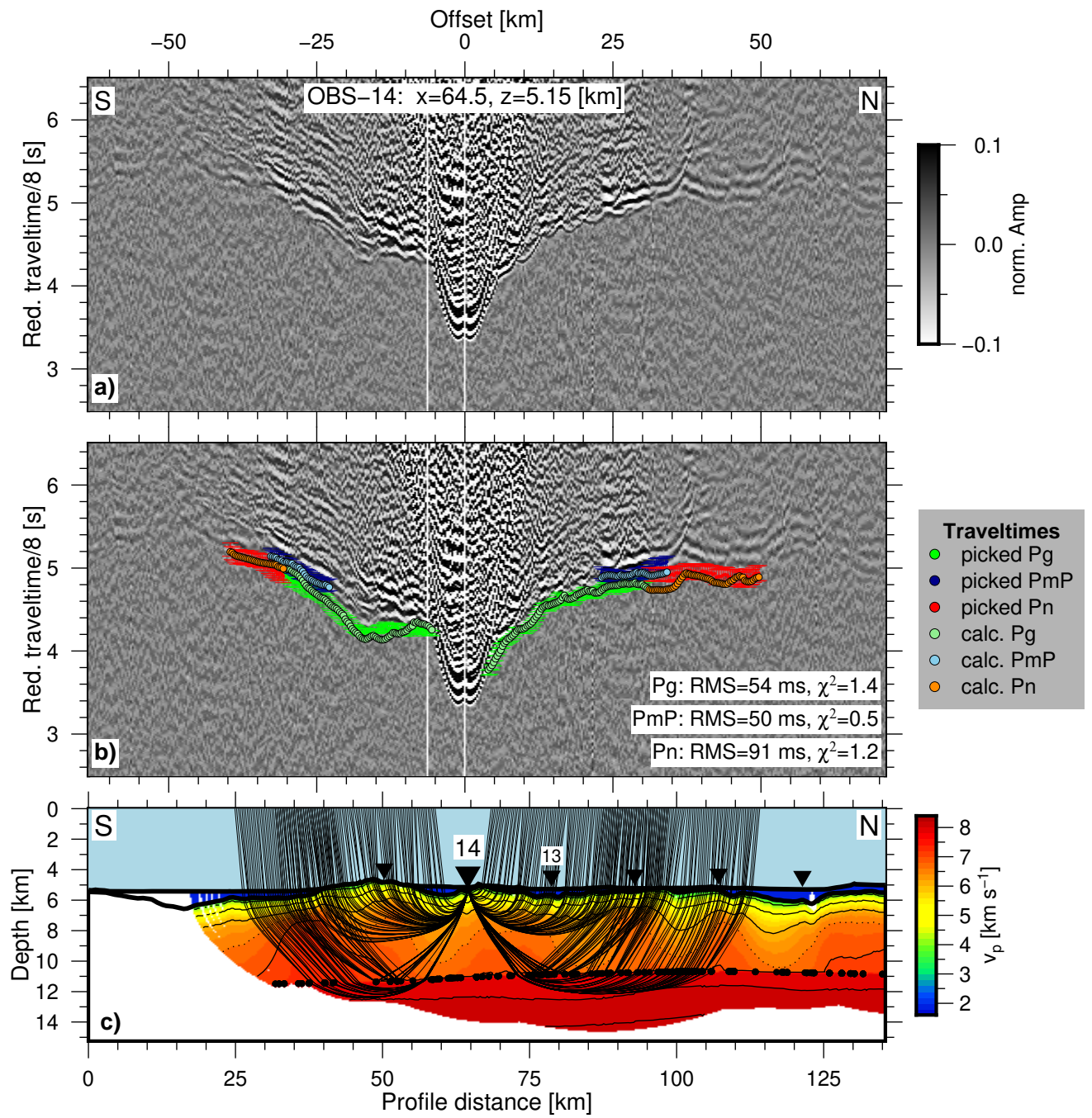**Figure S1h.** Record section, traveltime fit and raypaths for OBS 79 (LI-02).
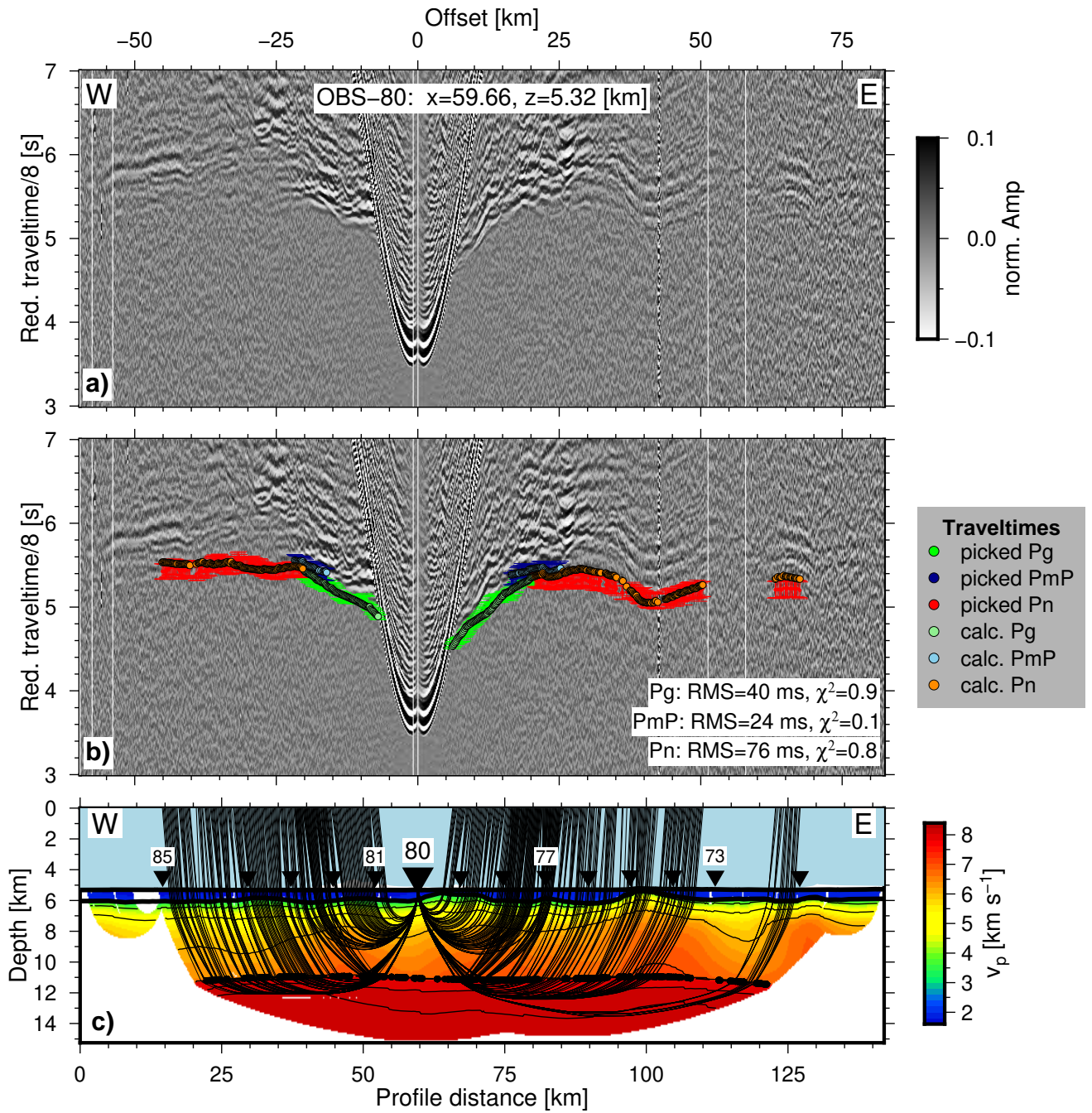
Figure S1i. Record section, traveltime fit and raypaths for OBS 80 (LI-02).
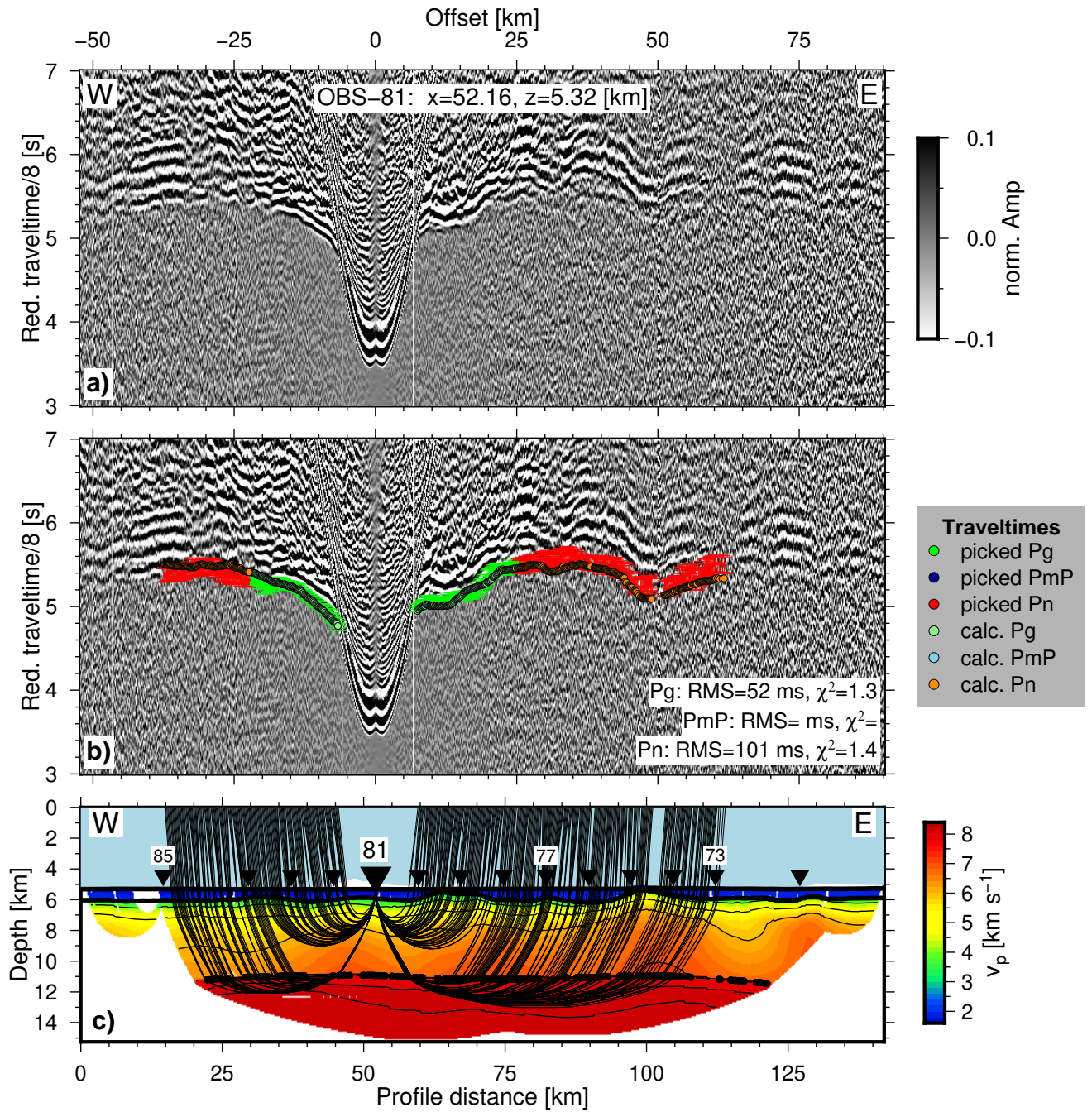
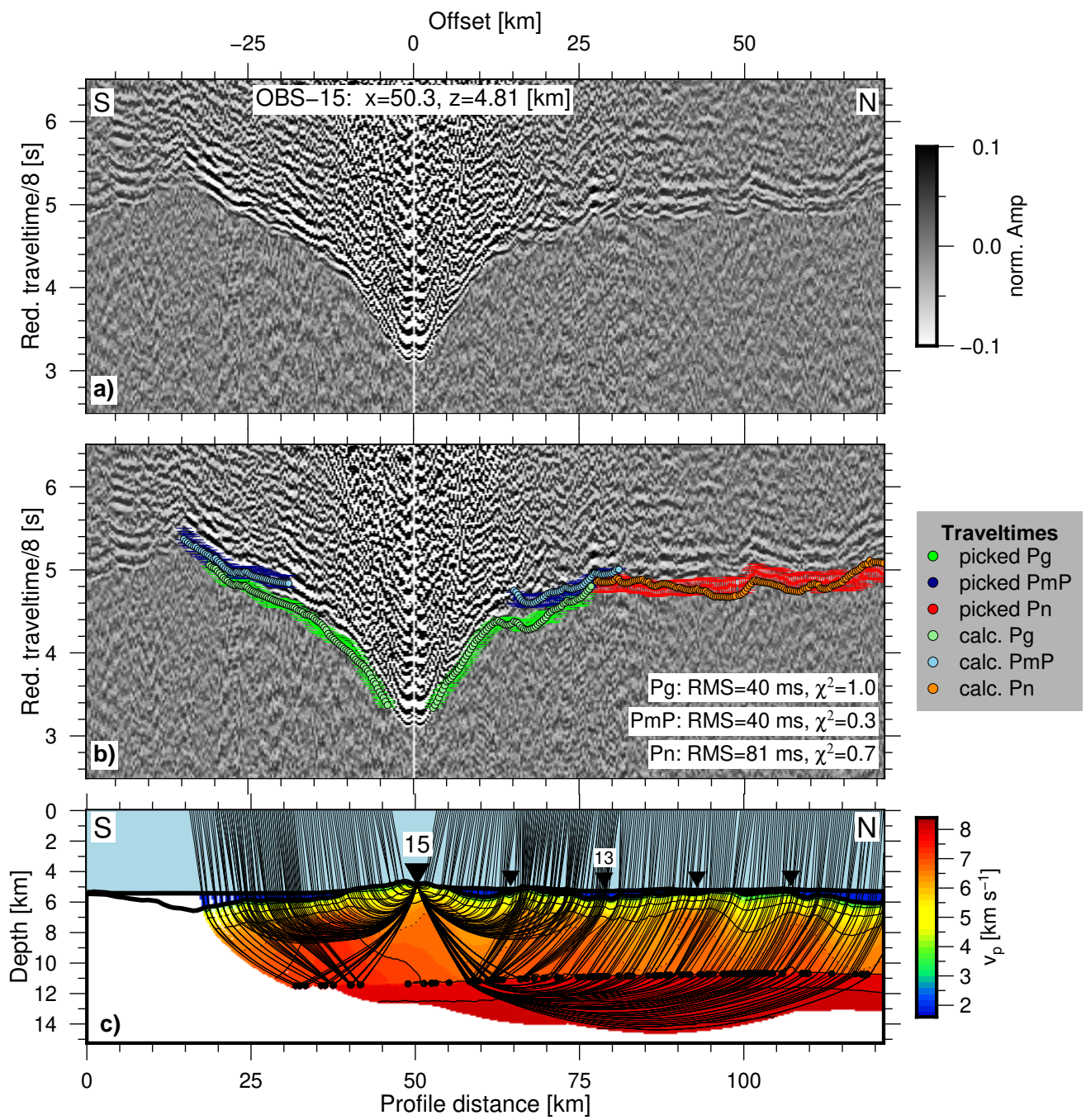**Figure S1j.** Record section, traveltime fit and raypaths for OBS 81 (LI-02).
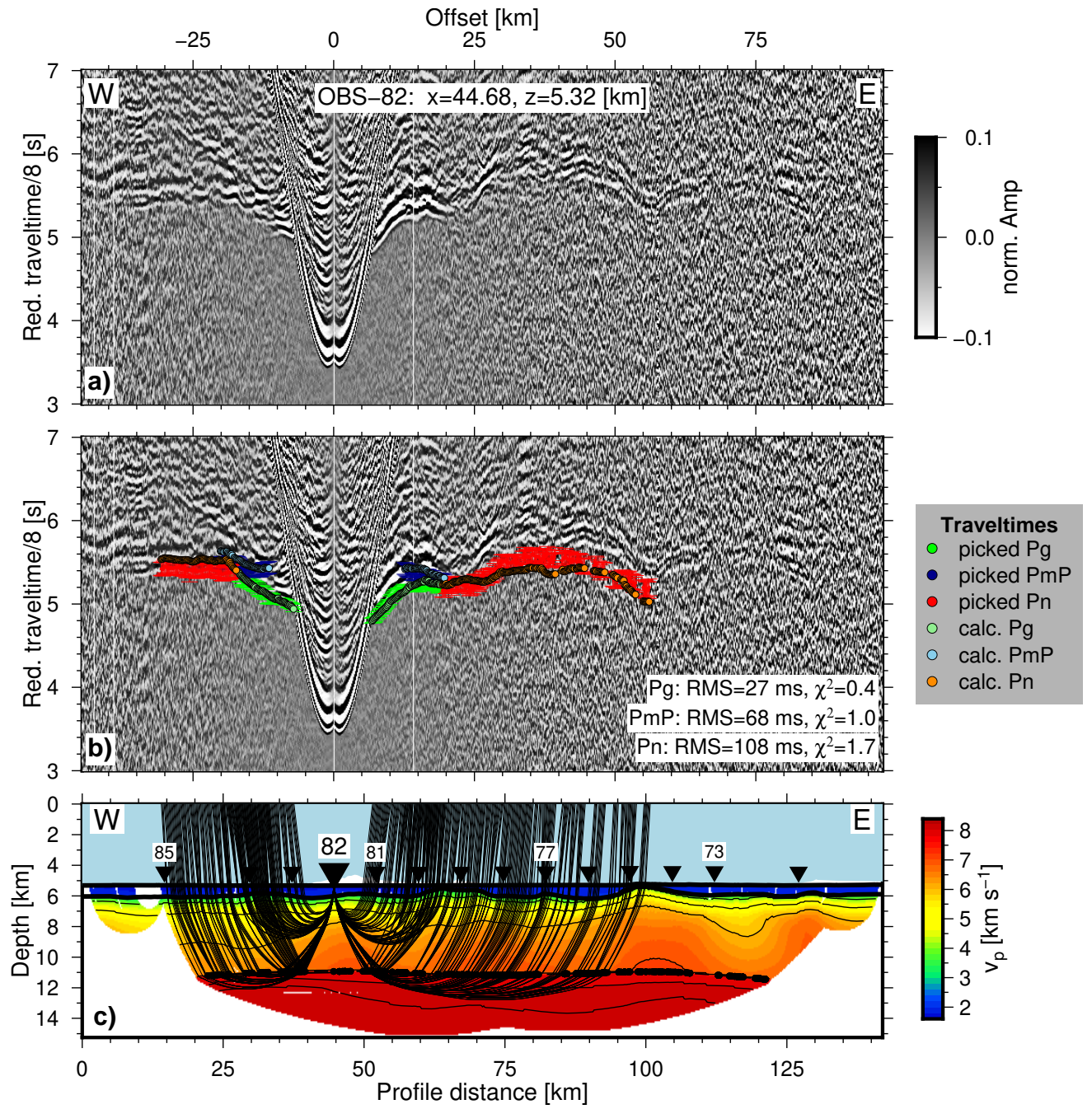
Figure S1k. Record section, traveltime fit and raypaths for OBS 82 (LI-02) .
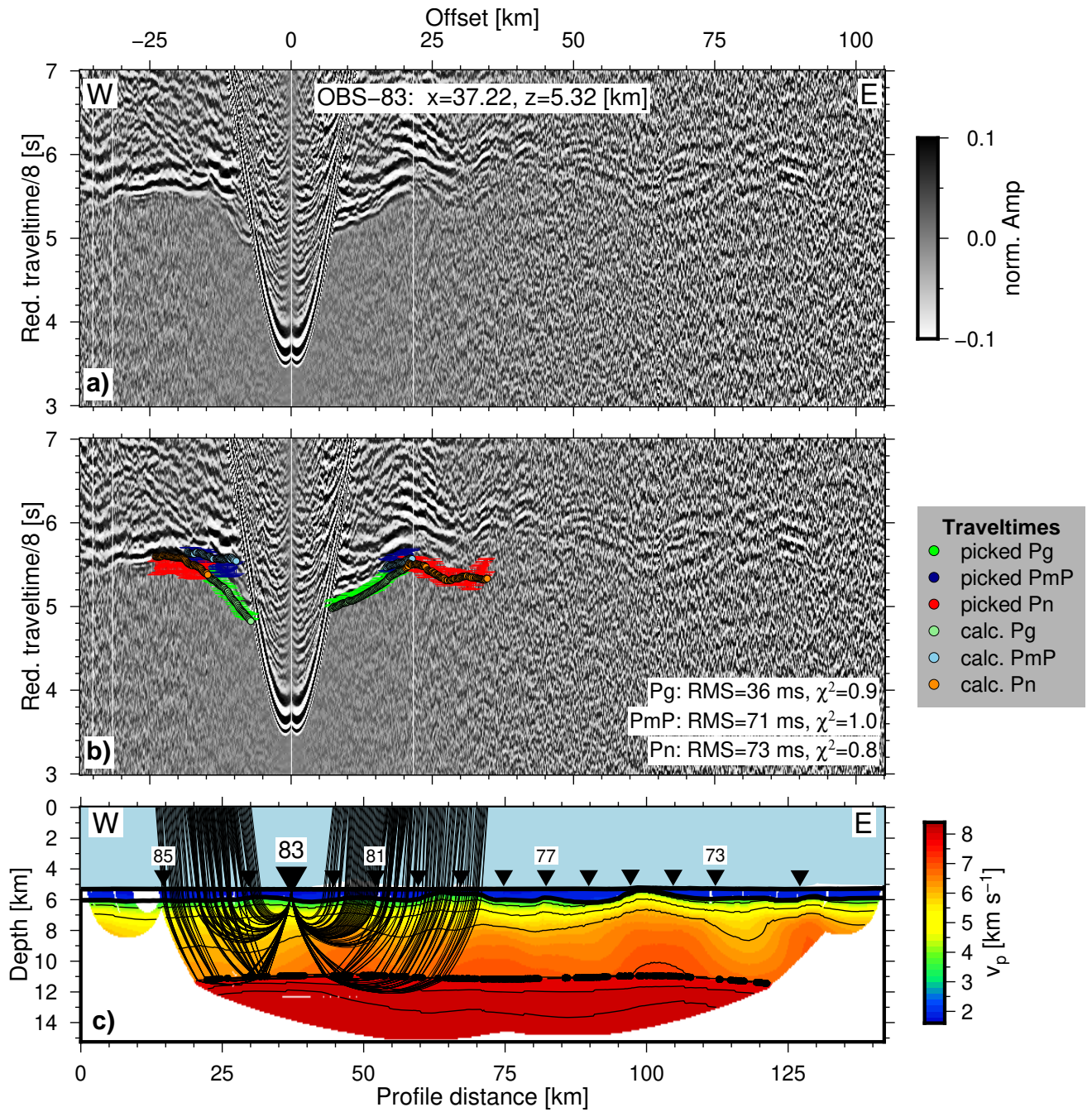
Figure S1l. Record section, traveltime fit and raypaths for OBS 83 (LI-02).
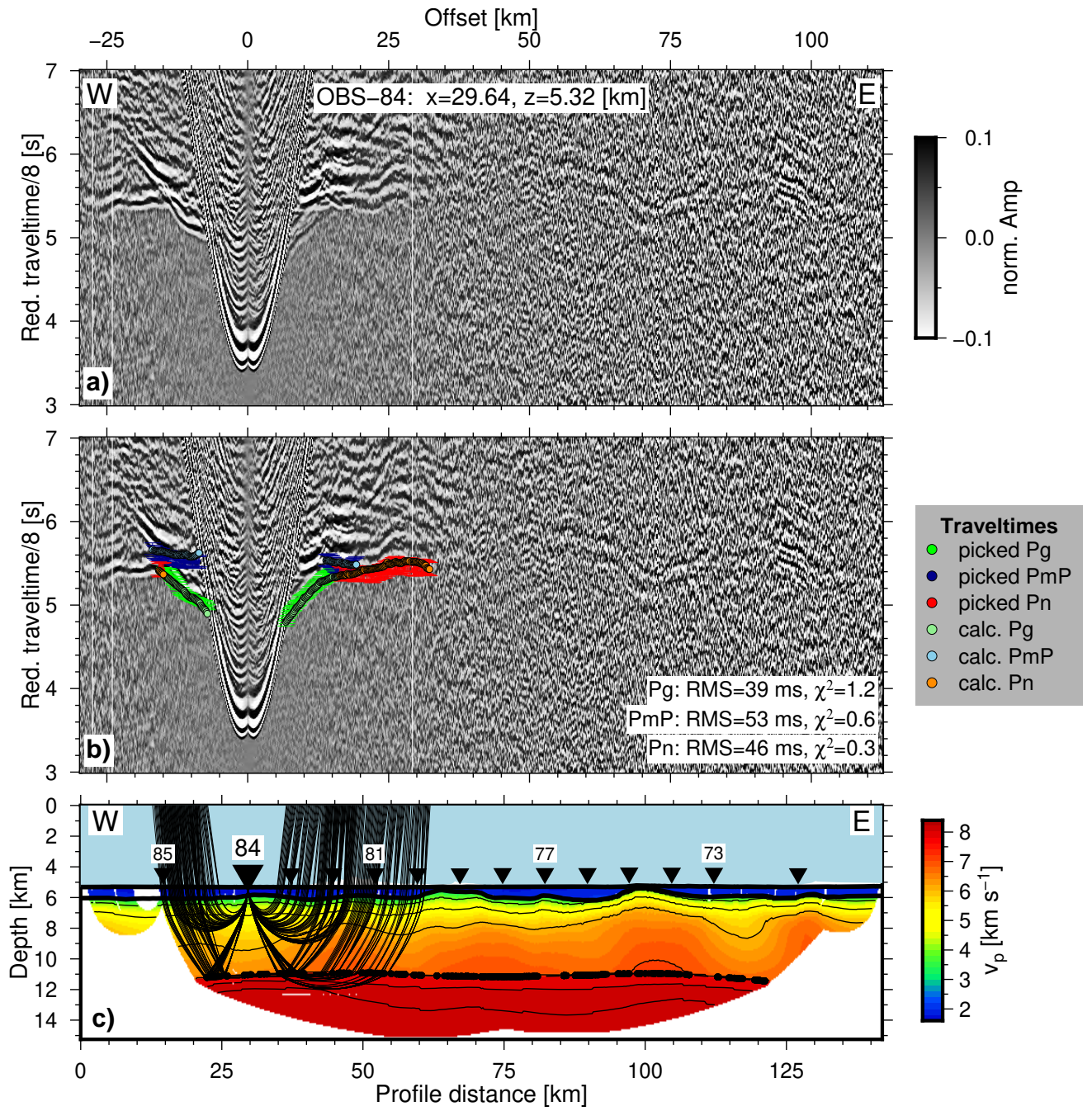
Figure S1m. Record section, traveltime fit and raypaths for OBS 84 (LI-02).
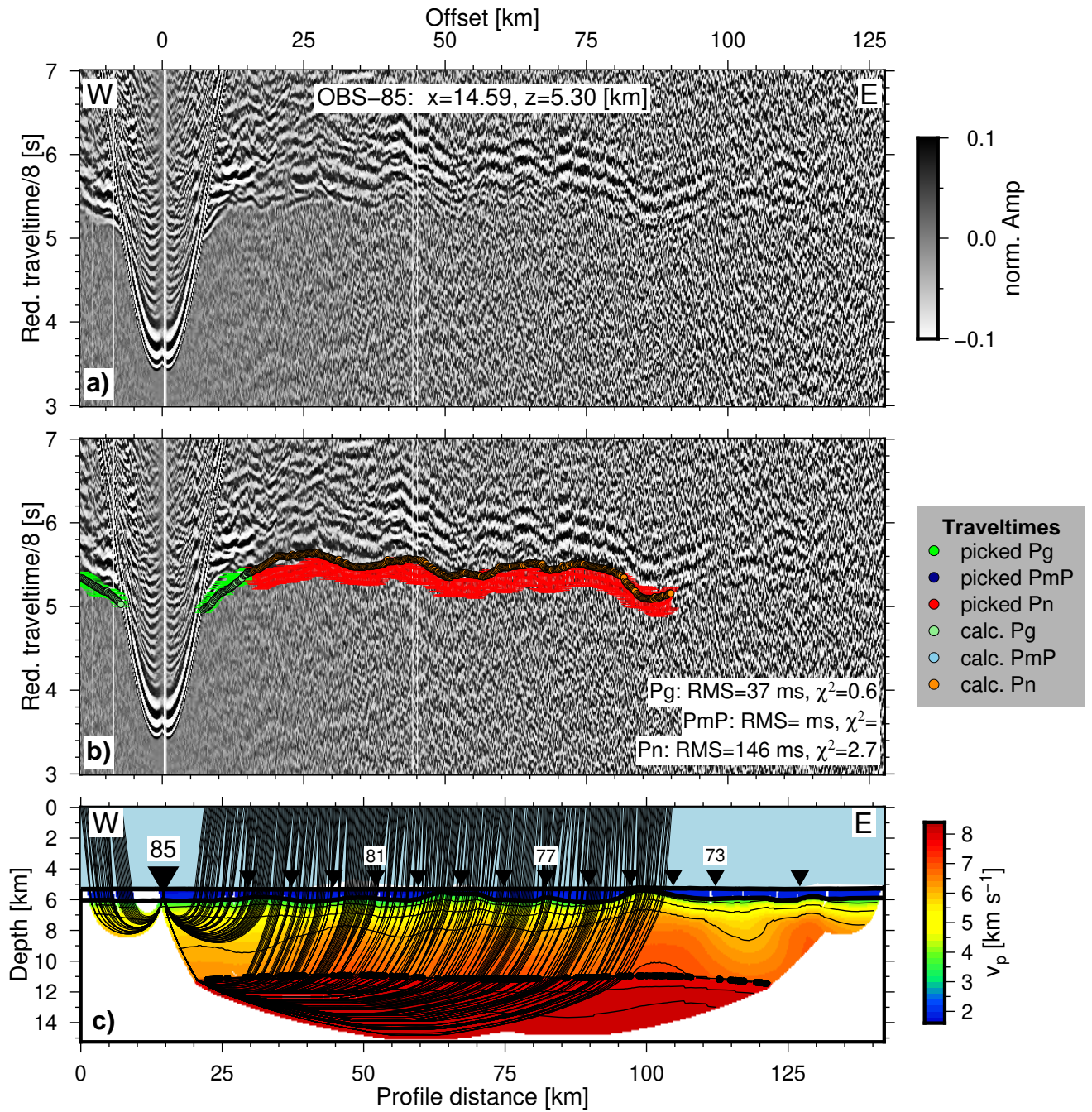
Figure S1n. Record section, traveltime fit and raypaths for OBS 85 (LI-02).
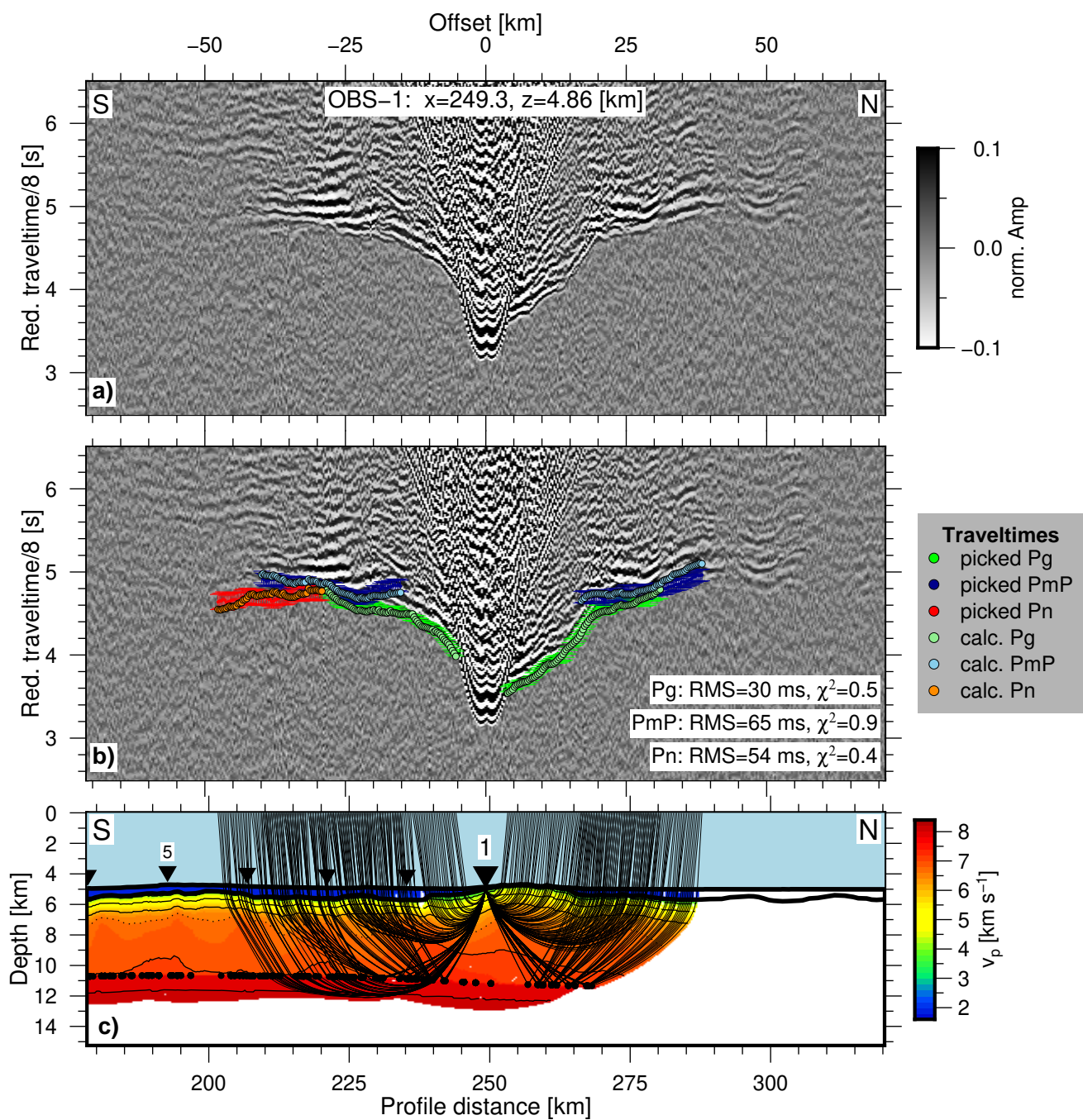
Figure S2a. Record section, traveltime fit and raypaths for OBS 01 (IS-01).
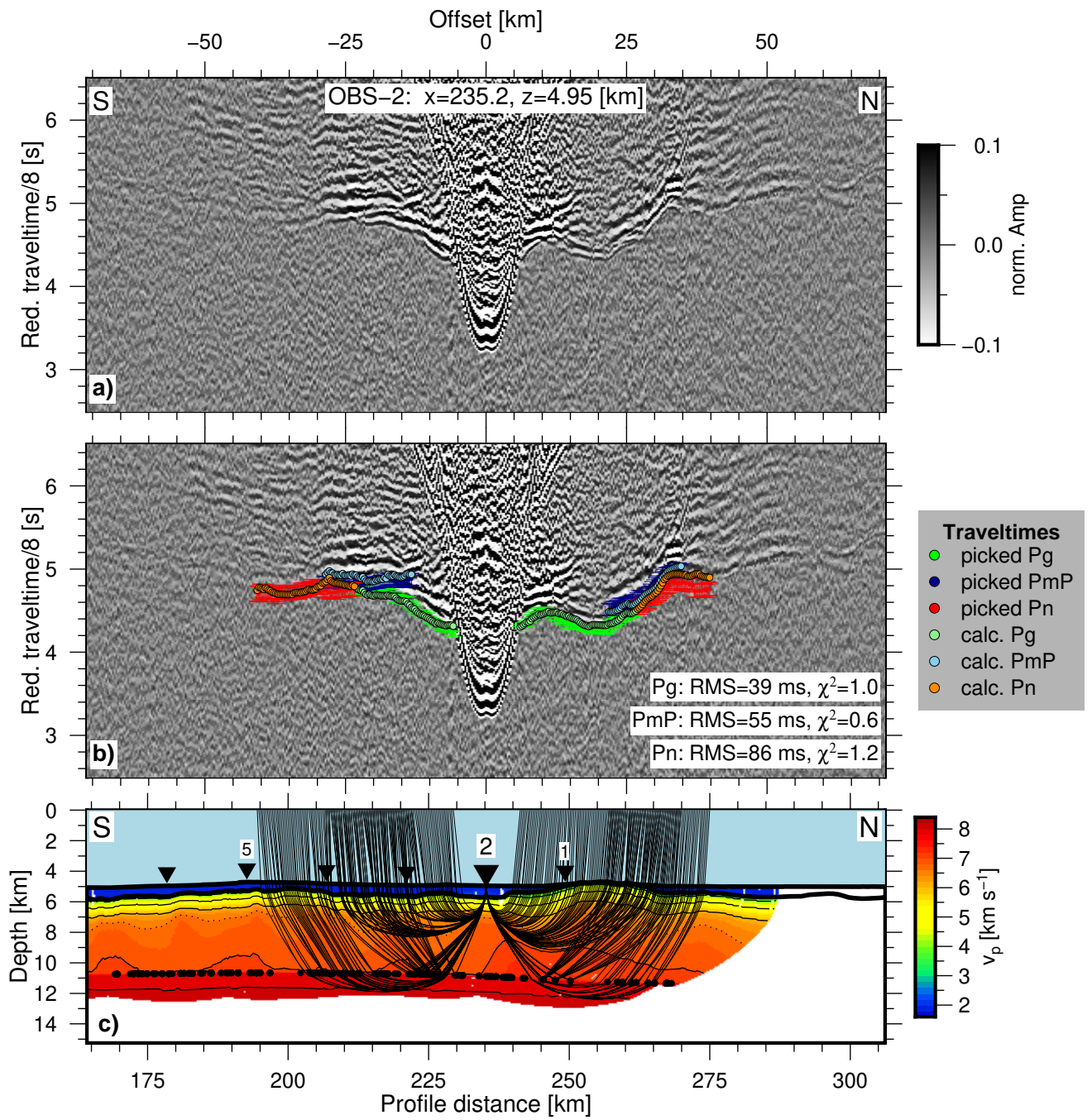
**Figure S2b.** Record section, traveltime fit and raypaths for OBS 02 (IS-01).
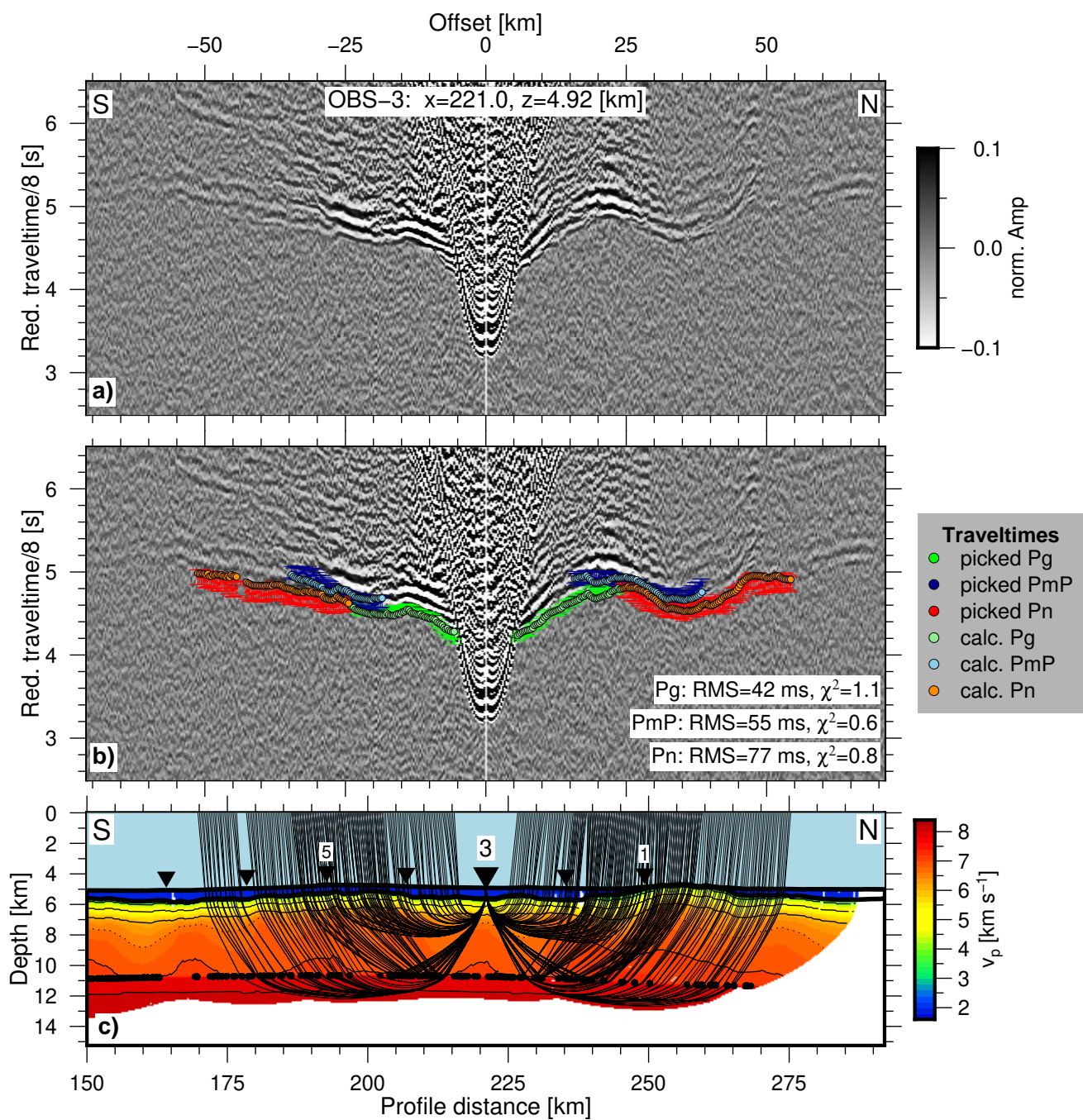
Figure S2c. Record section, traveltime fit and raypaths for OBS 03 (IS-01).
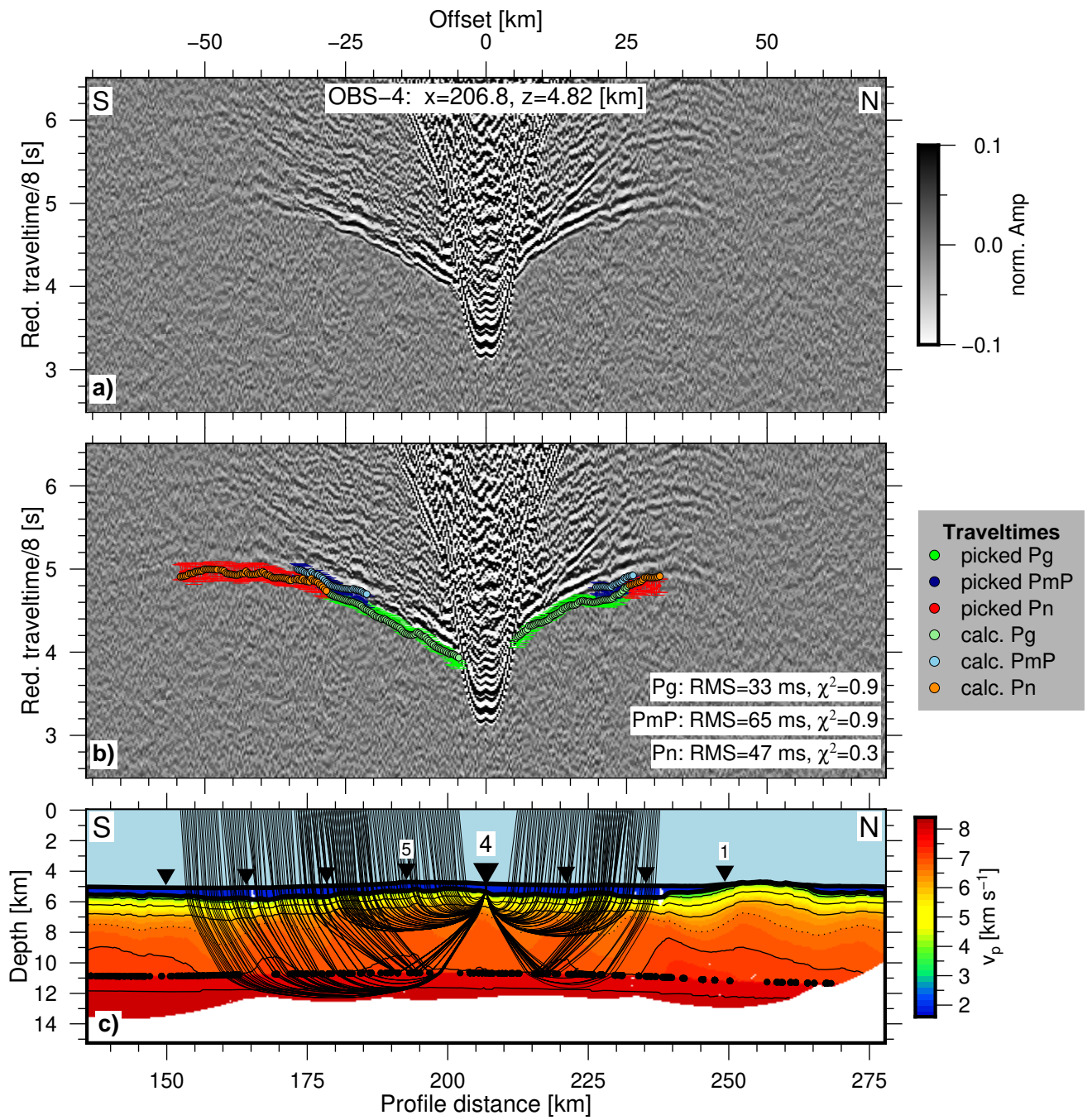
Figure S2d. Record section, traveltime fit and raypaths for OBS 04 (IS-01).
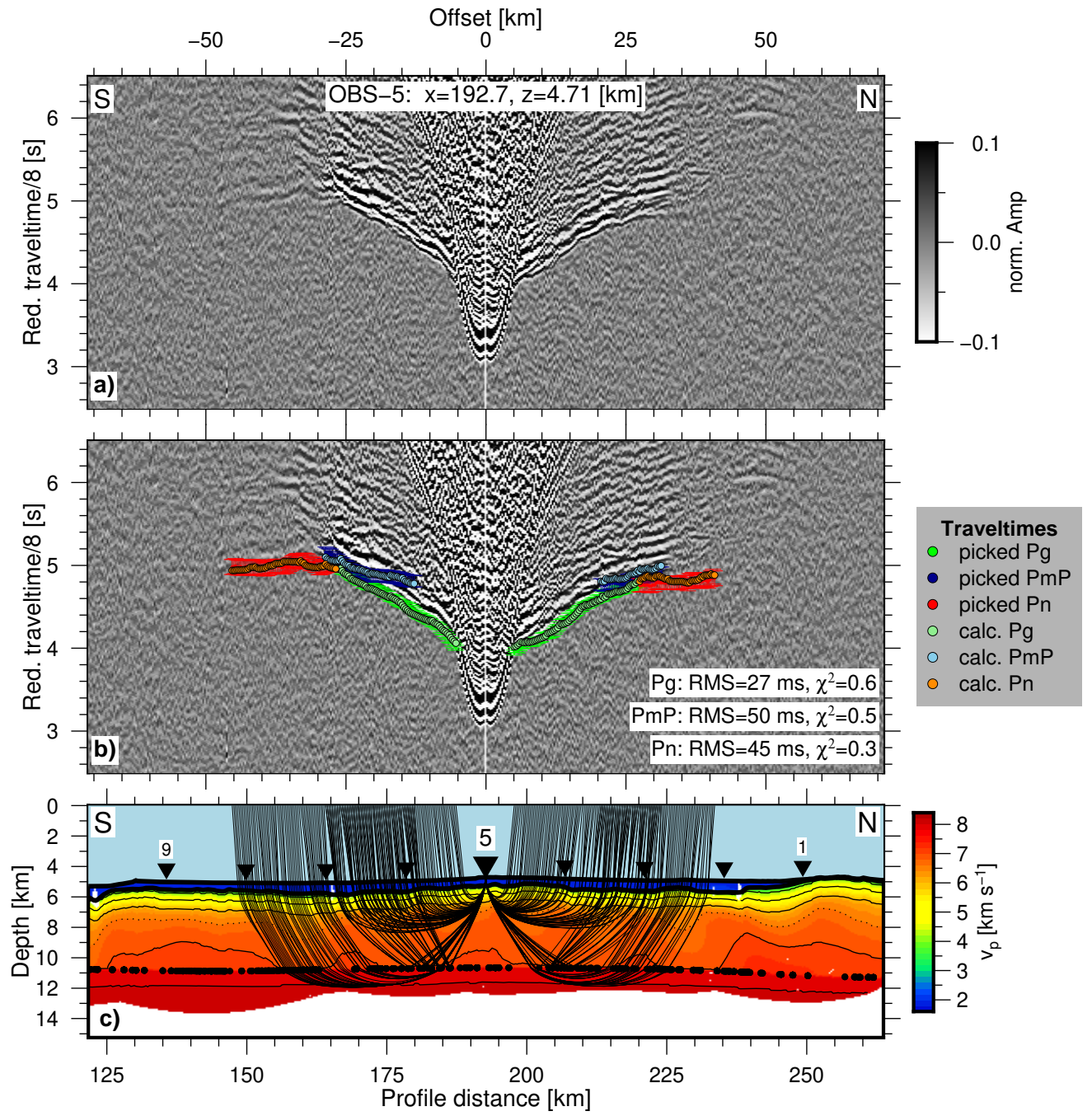
Figure S2e. Record section, traveltime fit and raypaths for OBS 05 (IS-01).
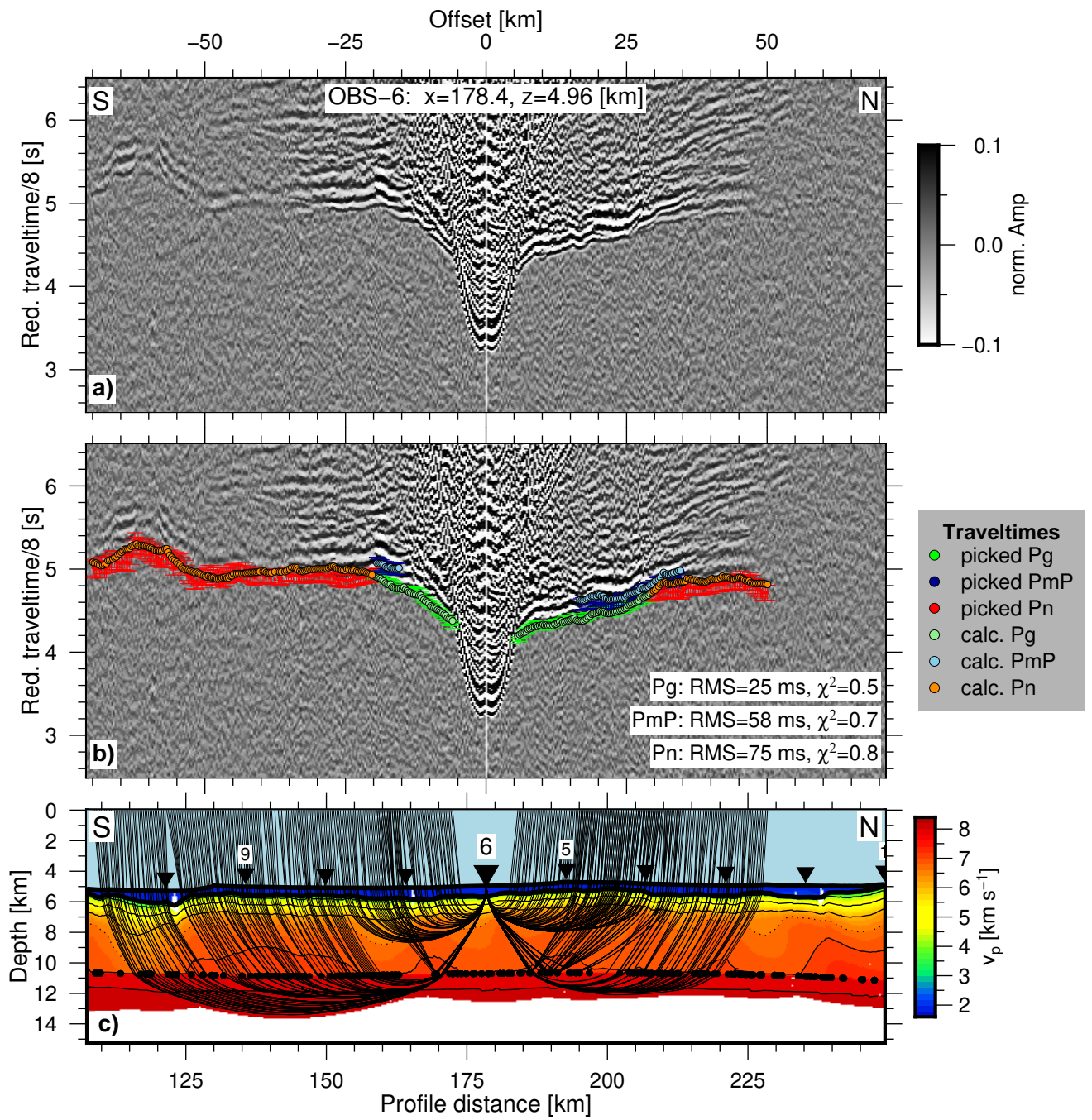
Figure S2f. Record section, traveltime fit and raypaths for OBS 06 (IS-01).
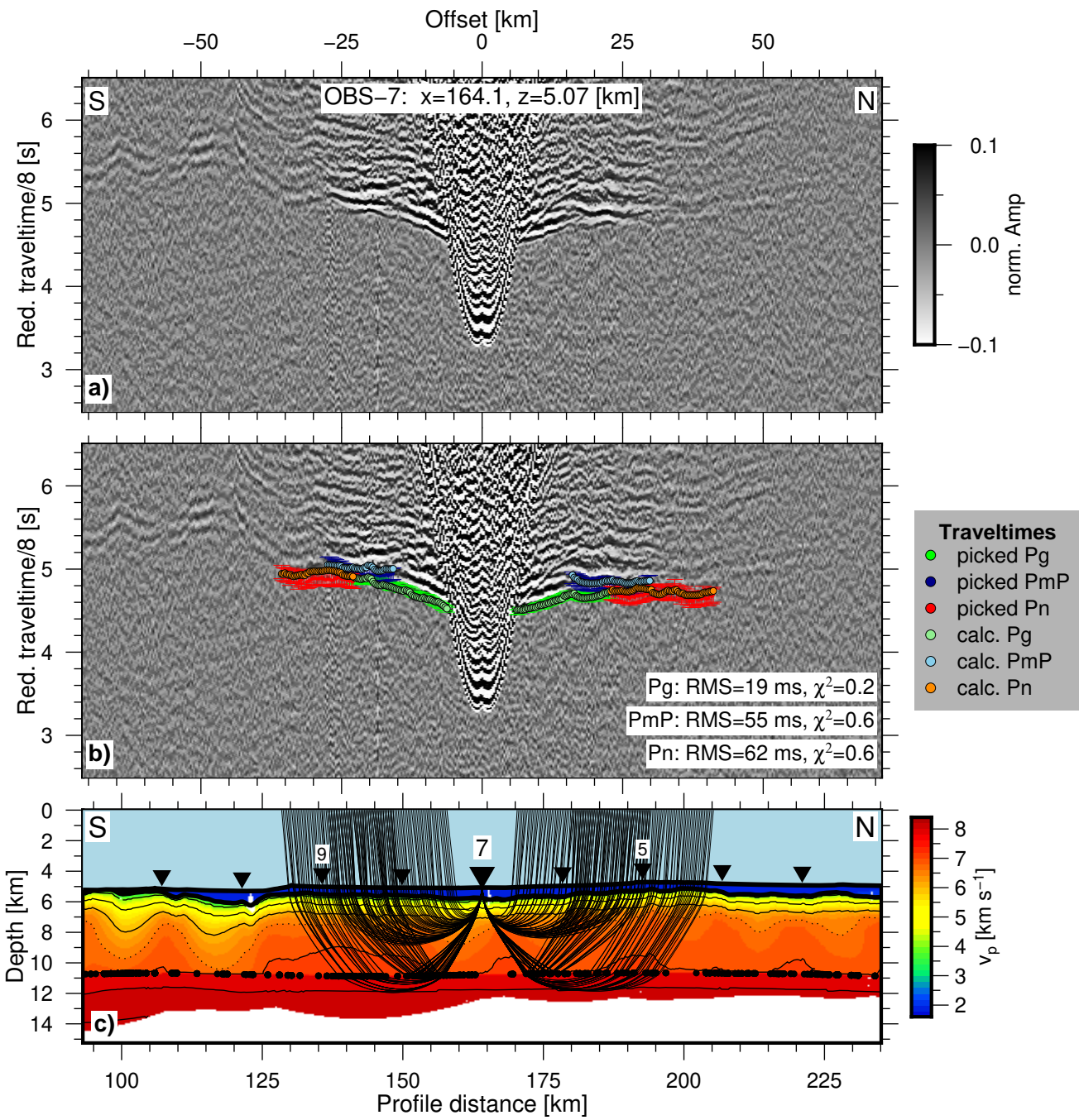
Figure S2g. Record section, traveltime fit and raypaths for OBS 07 (IS-01).
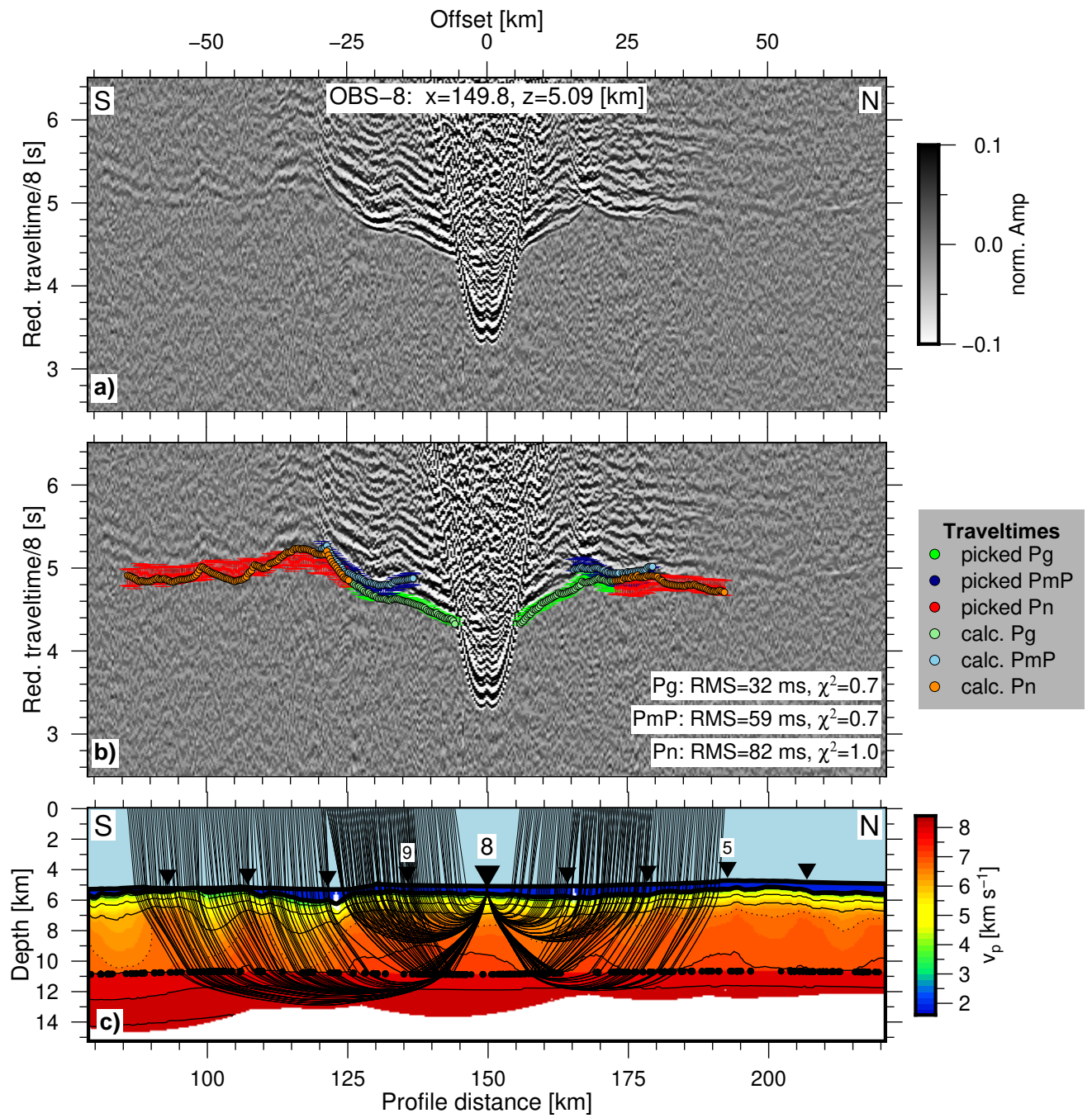
Figure S2h. Record section, traveltime fit and raypaths for OBS 08 (IS-01).
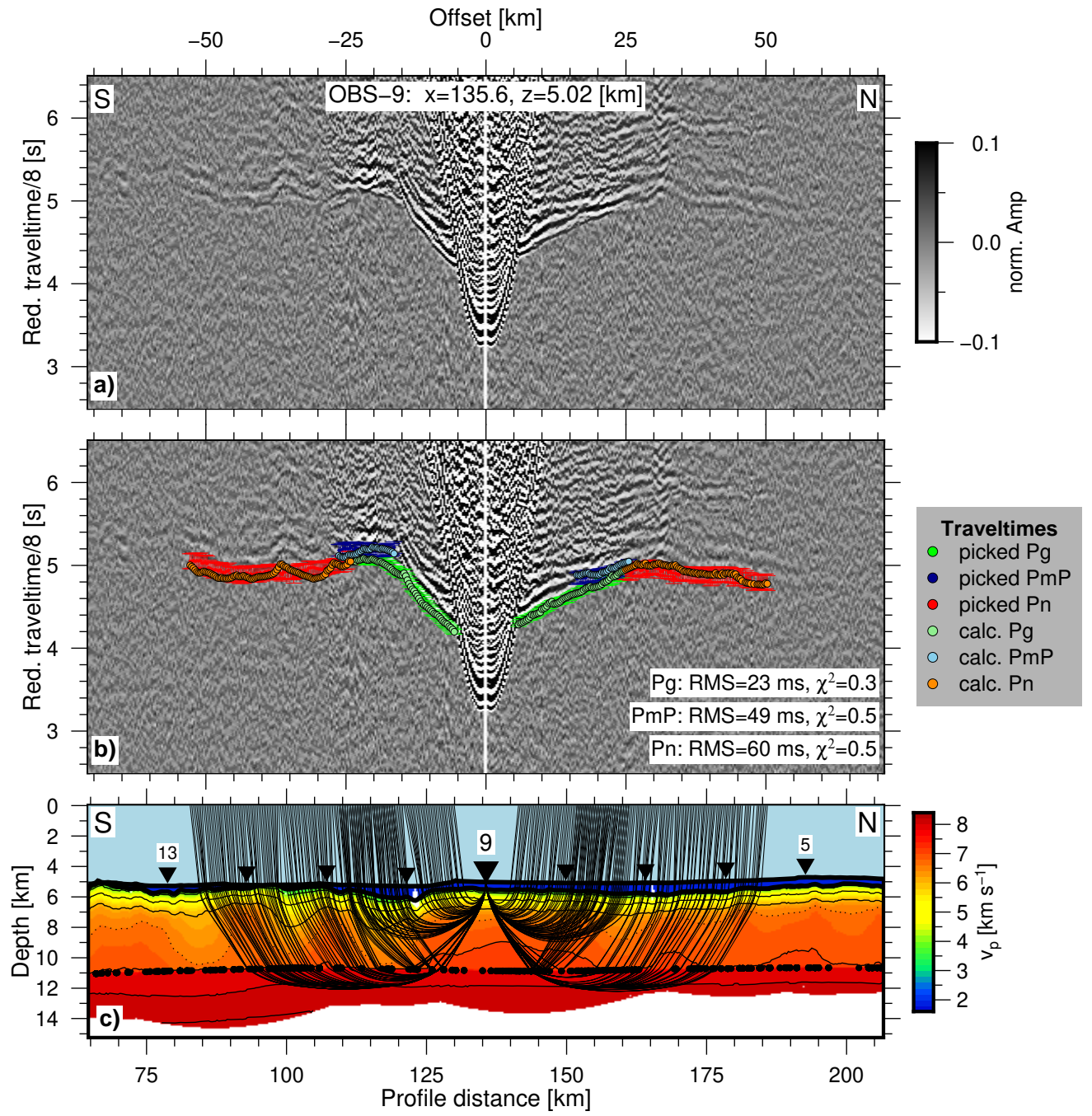
Figure S2i. Record section, traveltime fit and raypaths for OBS 09 (IS-01).

Figure S2j. Record section, traveltime fit and raypaths for OBS 10 (IS-01).

Figure S2k. Record section, traveltime fit and raypaths for OBS 11 (IS-01).

Figure S2l. Record section, traveltime fit and raypaths for OBS 12 (IS-01).

Figure S2m.   Record section, traveltime fit and raypaths for OBS 13 (IS-01).

Figure S2n. Record section, traveltime fit and raypaths for OBS 14 (IS-01).

Figure S2o. Record section, traveltime fit and raypaths for OBS 15 (IS-01).
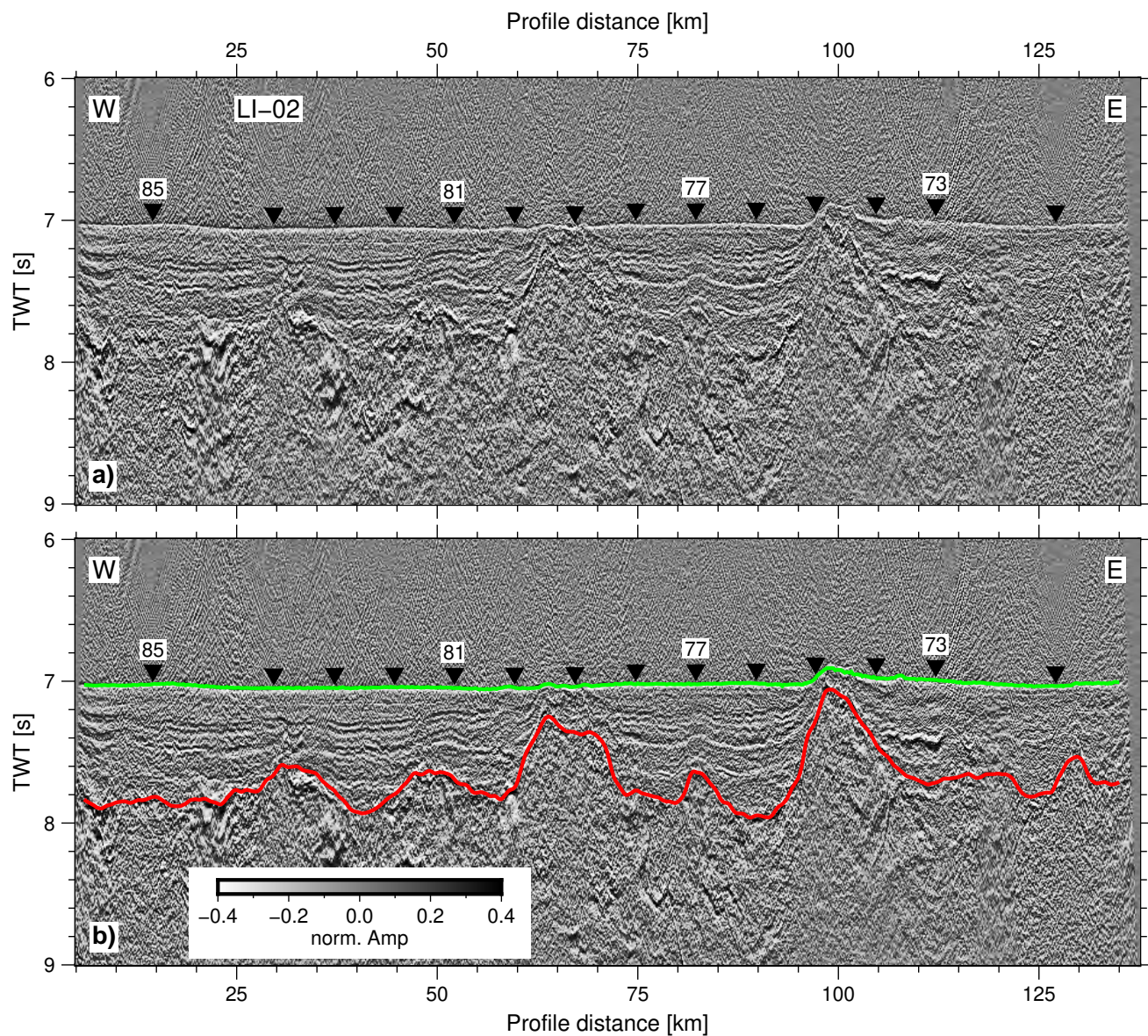
Figure S3. LI-02: **(a)** Mirror image obtained by migration of the multiples (e.g Grion et al., 2007) with **(b)** superimposed seafloor (green) and basement (red) picks. The amplitude is normalized by its maximum and clipped to 40 %.
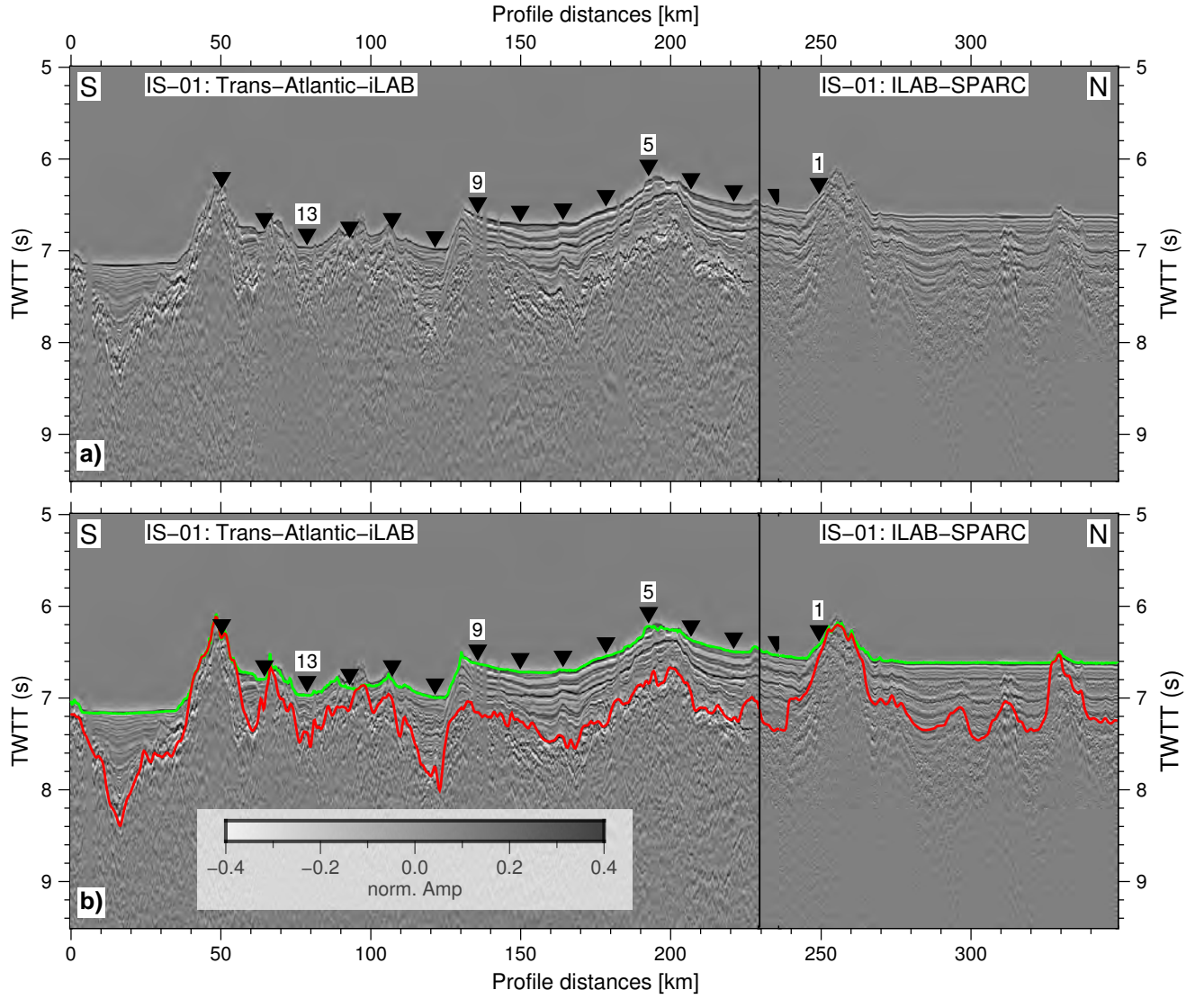
Figure S4. IS-01: **(a)** A composite post-stack time-migrated MCS section along the N-S line acquired during the two cruises, Trans-Atlantic-iLAB (2015) and ILAB-SPARC (2018). The solid vertical line indicates the joint location for the two datasets. The information on the MCS data processing steps is provided in the main text. The amplitude is normalized by its maximum and clipped to 40 %. **(b)** Seafloor (green) and basement (red) picks are superimposed on the seismic section.
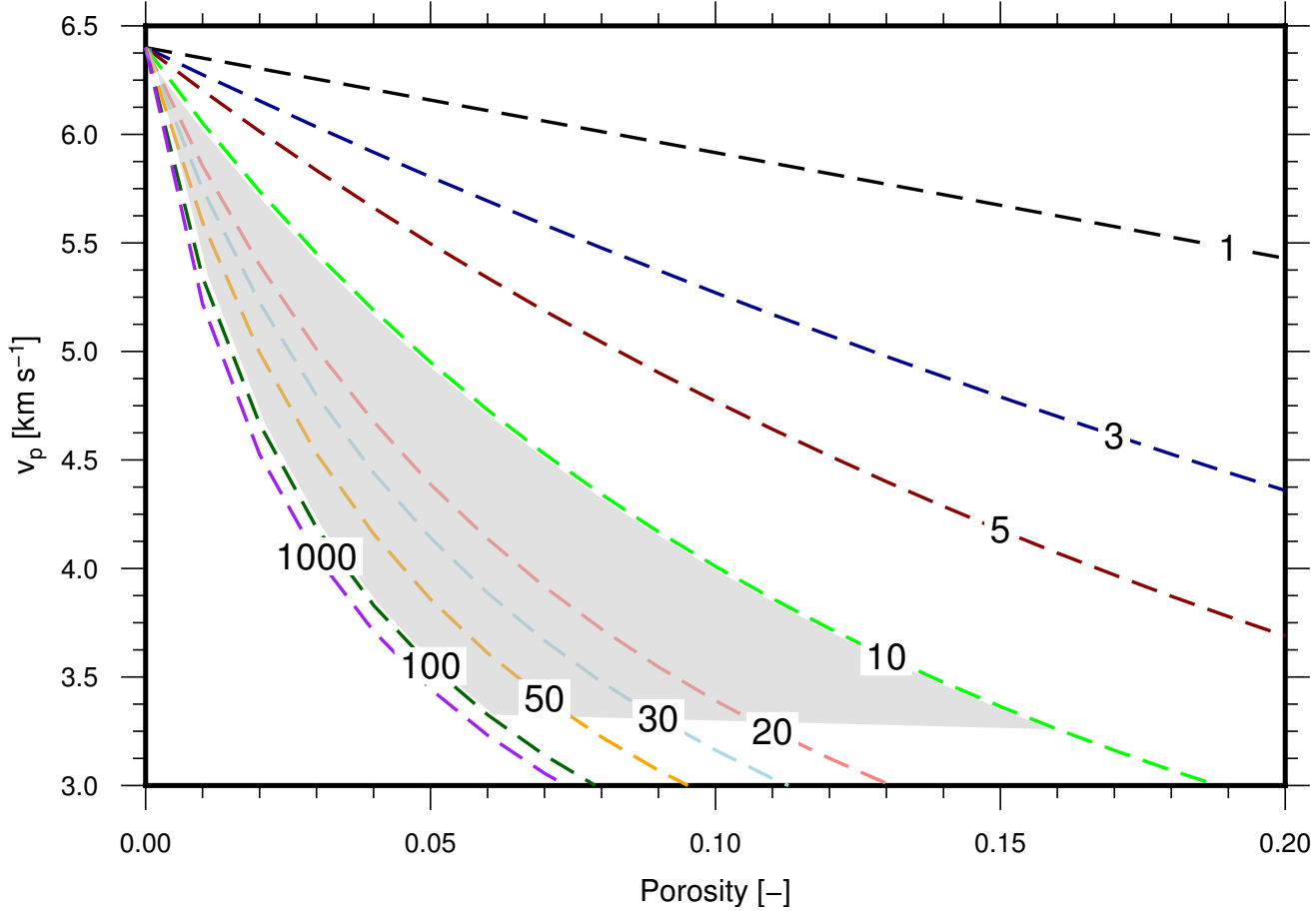
Figure S5.   Velocity-porosity relationship for different aspect ratios of fractures (numbered labels). Calculated using a differential effective medium analysis after Taylor and Singh (2002) for a basaltic host rock. Grey area highlights the range of observed crustal velocities and hence the range of possible porosities with respect to the chosen range of aspect ratios of 10-100.
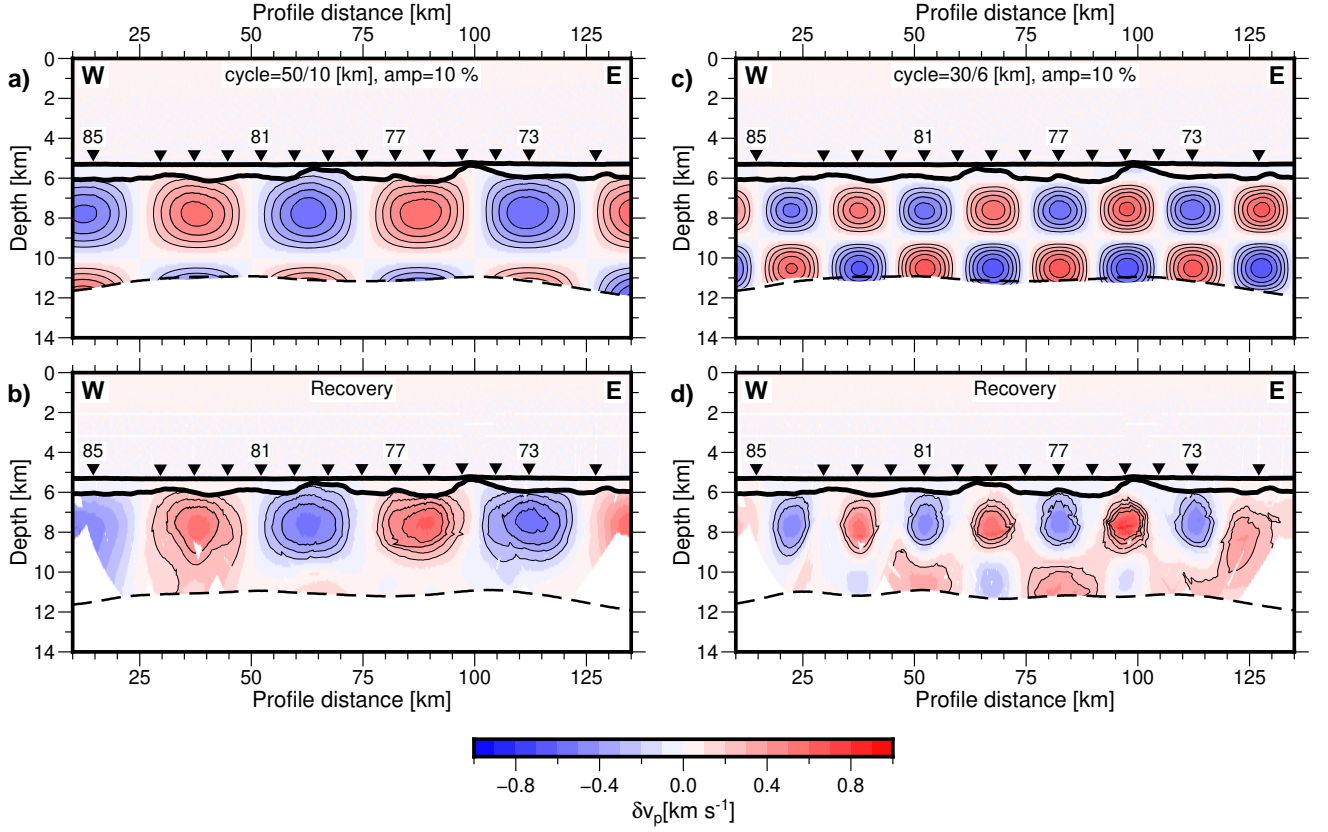
Figure S6. Checkerboard test for LI-02: crustal checkerboard resolution test for different cycle lengths and a perturbation amplitude of 10 %. The contour interval is 0.1 km/s starting at ±0.2 km/s. The dashed line denotes the constrained Moho reflector. The remaining figure elements are the same as in Figure 5 in the main text.
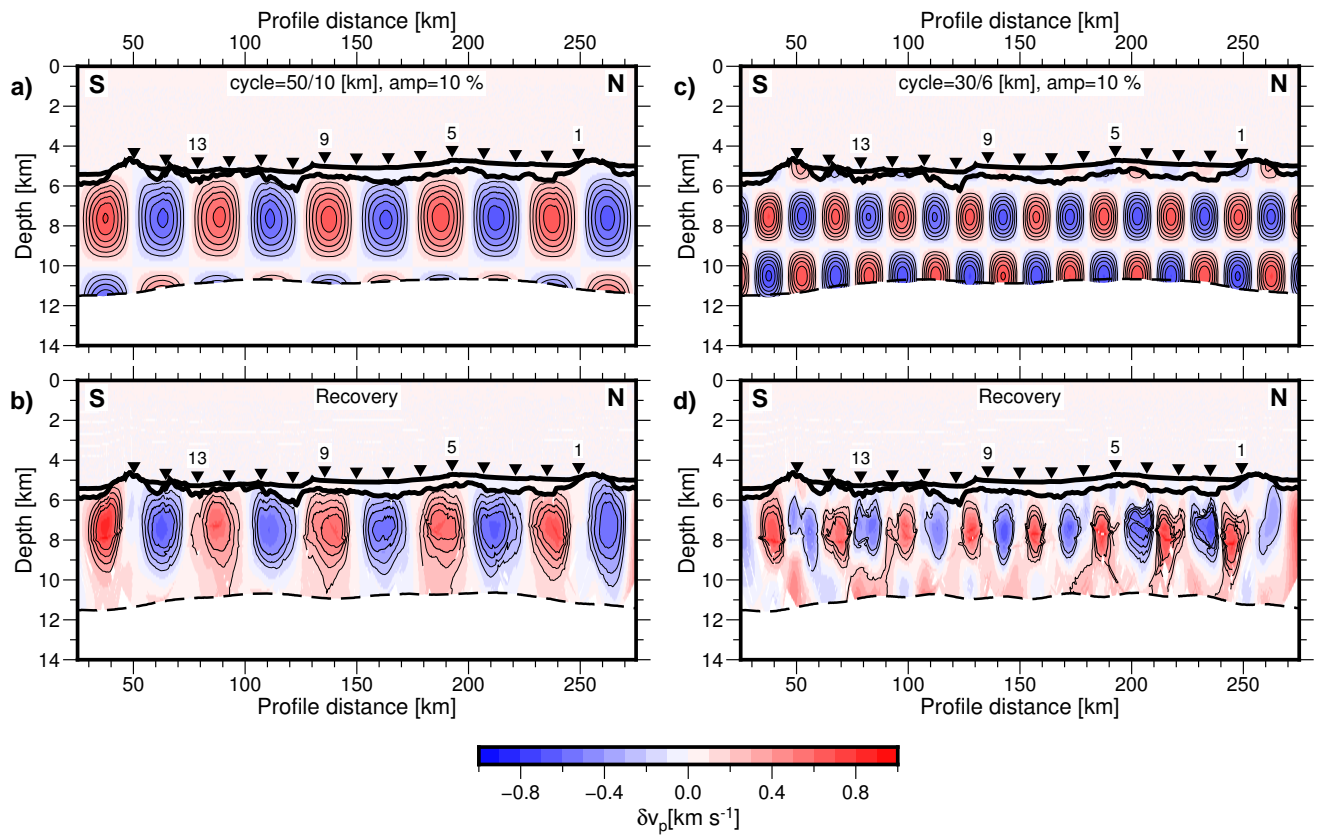
Figure S7. Checkerboard test for IS-01: checkerboard resolution test as in Fig. S6.
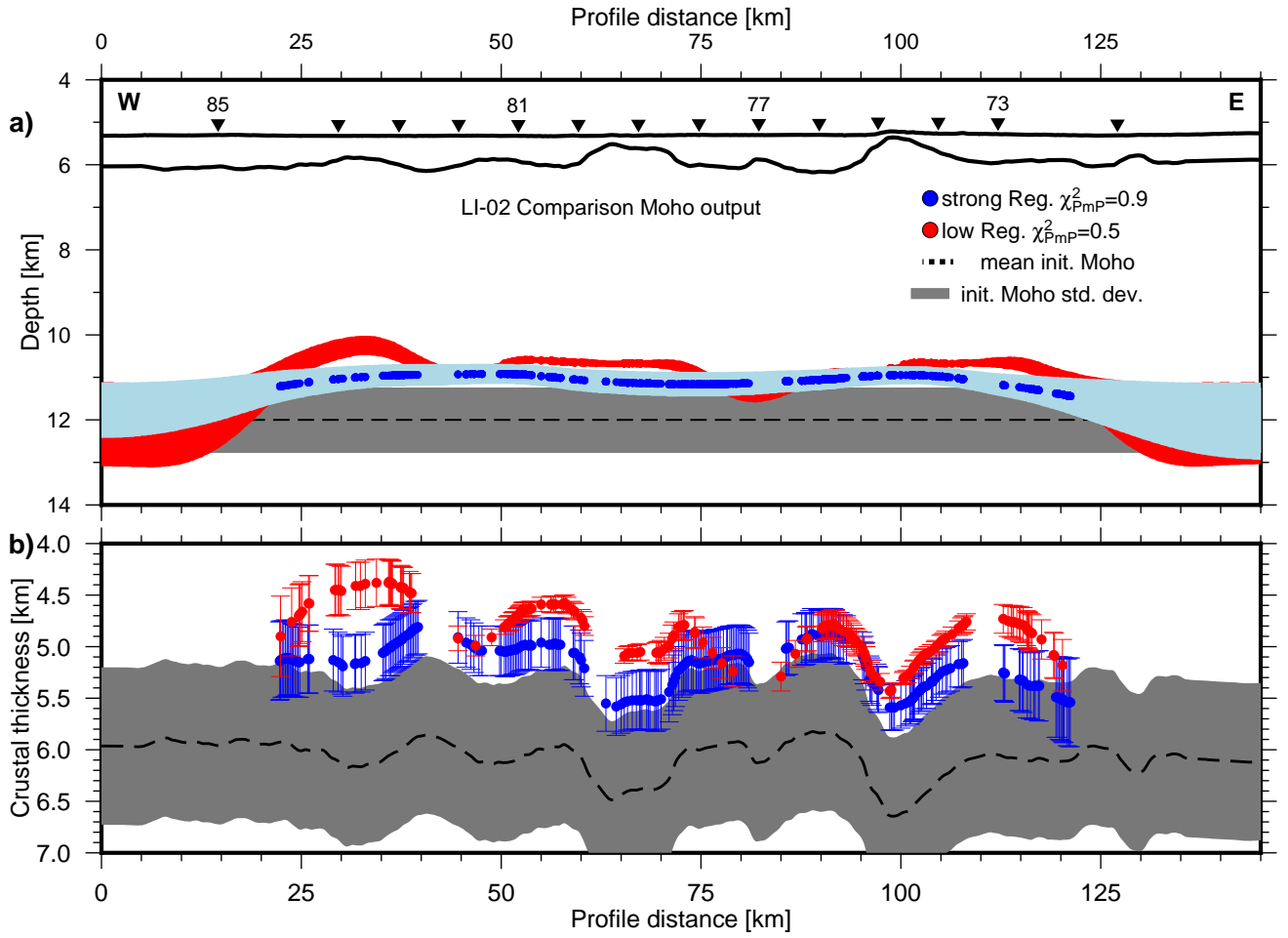
Figure S8. LI-02: **(a)** Comparison of Moho results for line LI-02 from the MCAs using 'strong' (blue) and weak regularization (see Table S3). Dots and shaded areas denote the mean obtained reflection points and the Moho standard deviation from the MCA. Dashed line and gray shading denote the mean initial Moho and the input standard deviation. Solid black lines denote the seafloor and the basement. The inverted black triangles denote the OBS locations. Every fourth OBS is labeled. **(b)** Corresponding crustal thickness along the line. The dots and the error bars represent the modelled PmP reflection points and their standard deviation.
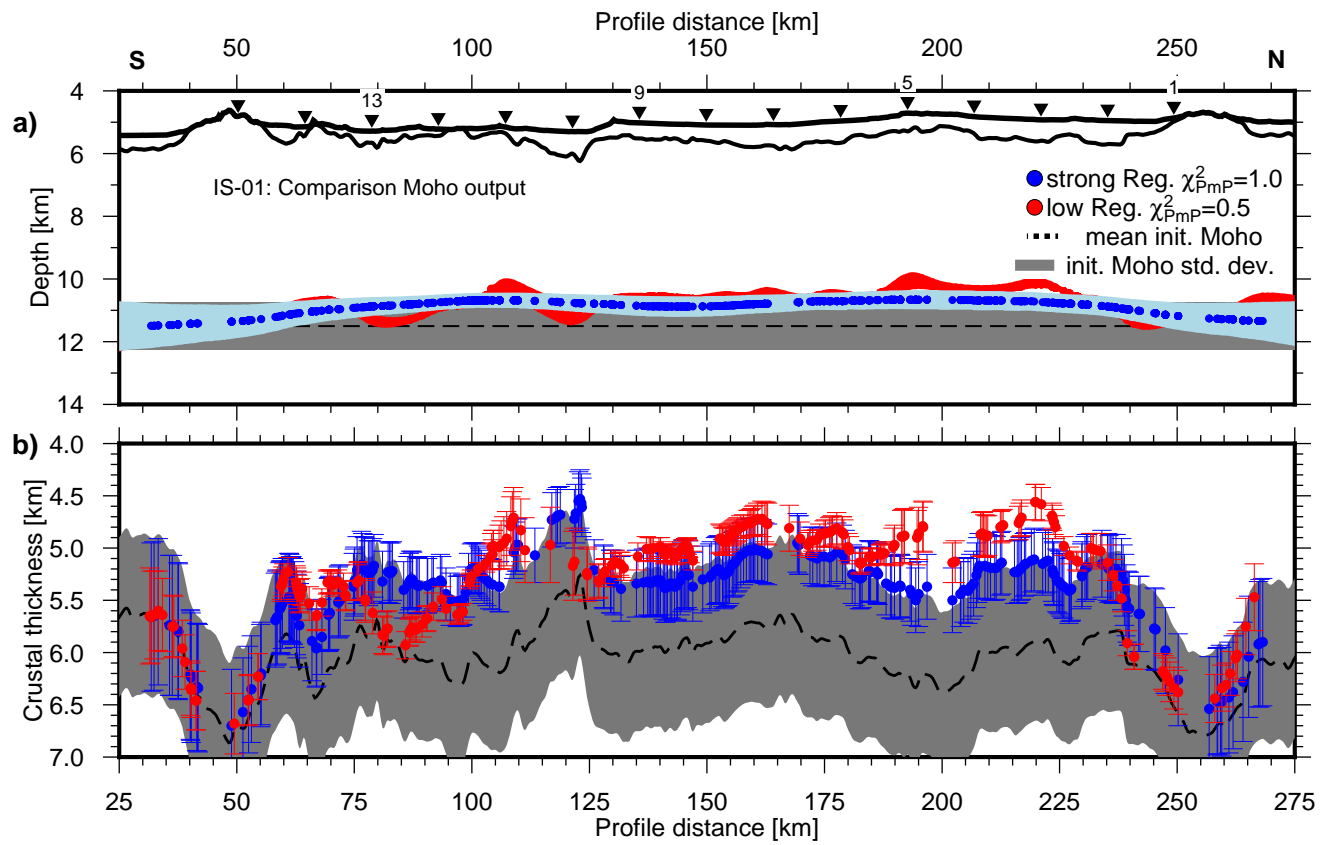
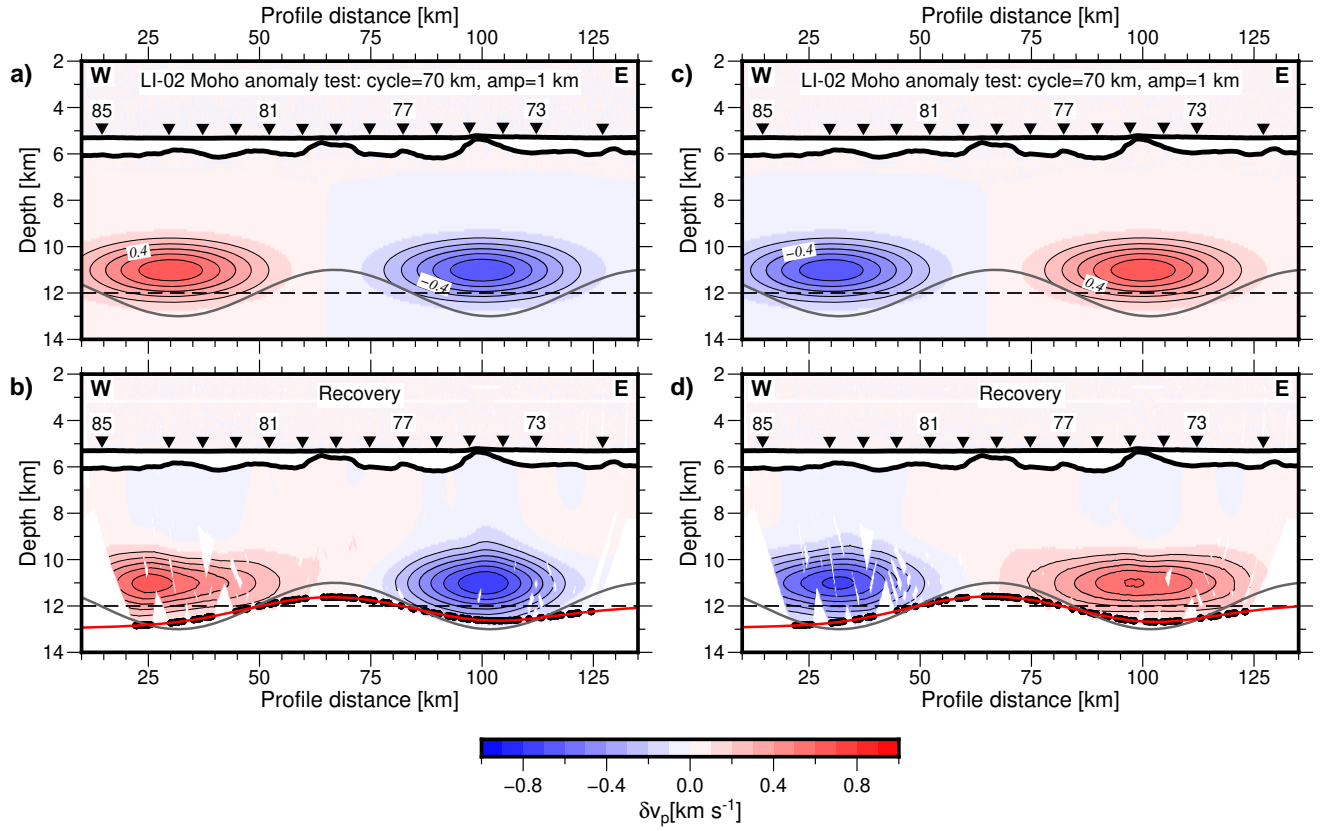**Figure S9.** IS-01: the same comparison as in Fig. S8 but for line IS-01.

Figure S10. LI-02: Resolution test for sinusoidal Moho anomaly with a cycle of 70 km and a perturbation amplitude of 1 km. Additionally, we introduced gaussian velocity anomalies with horizontal radius of 20 km, a vertical radius of 1.25 km and a perturbation amplitude of 10 % above the Moho reflector. Panels (c,d) show the same test with reversed polarity of (a,b). The contour interval is 0.1 km/s starting at 0.2 km/s. The horizontal dashed, the grey and red lines and the black dots denote the mean input reflector, the perturbed input reflector and the recovered reflector with its obtained reflection points, respectively.
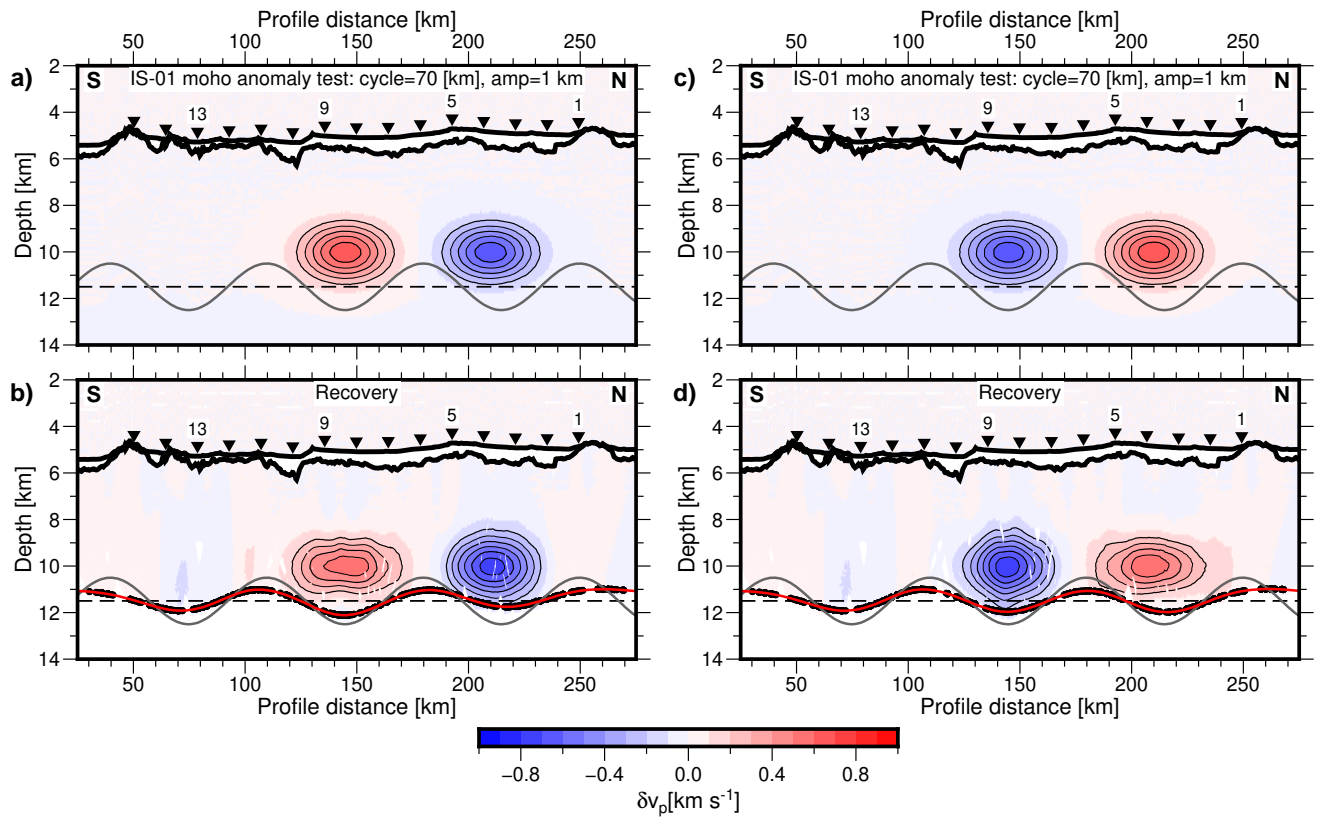
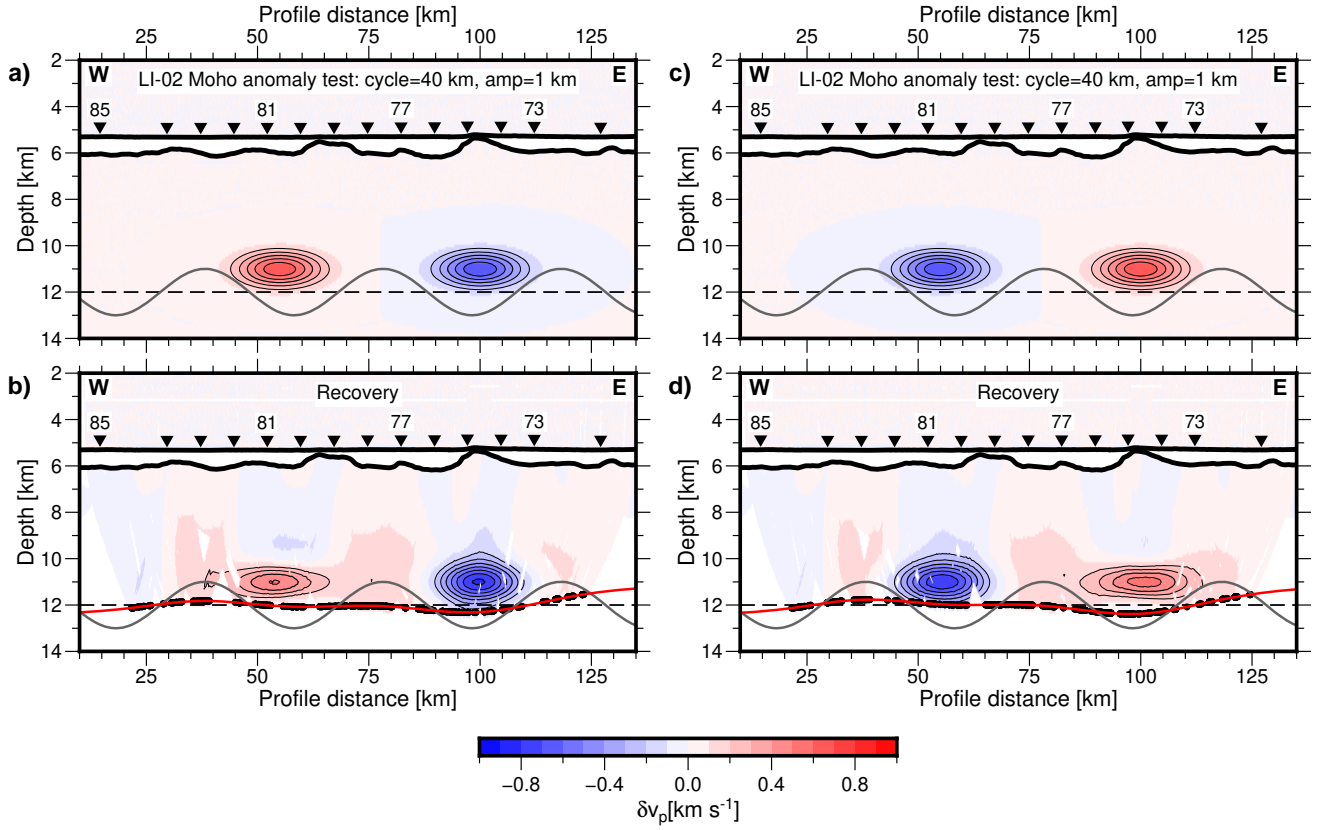**Figure S11.** Moho resolution test for IS-01: the same test procedure and figure elements as in Figure S10.

:

Figure S12.   Moho resolution test for LI-02: the same test as in Fig. S10 but with a reduced reflector perturbation cycle length of 40 km.
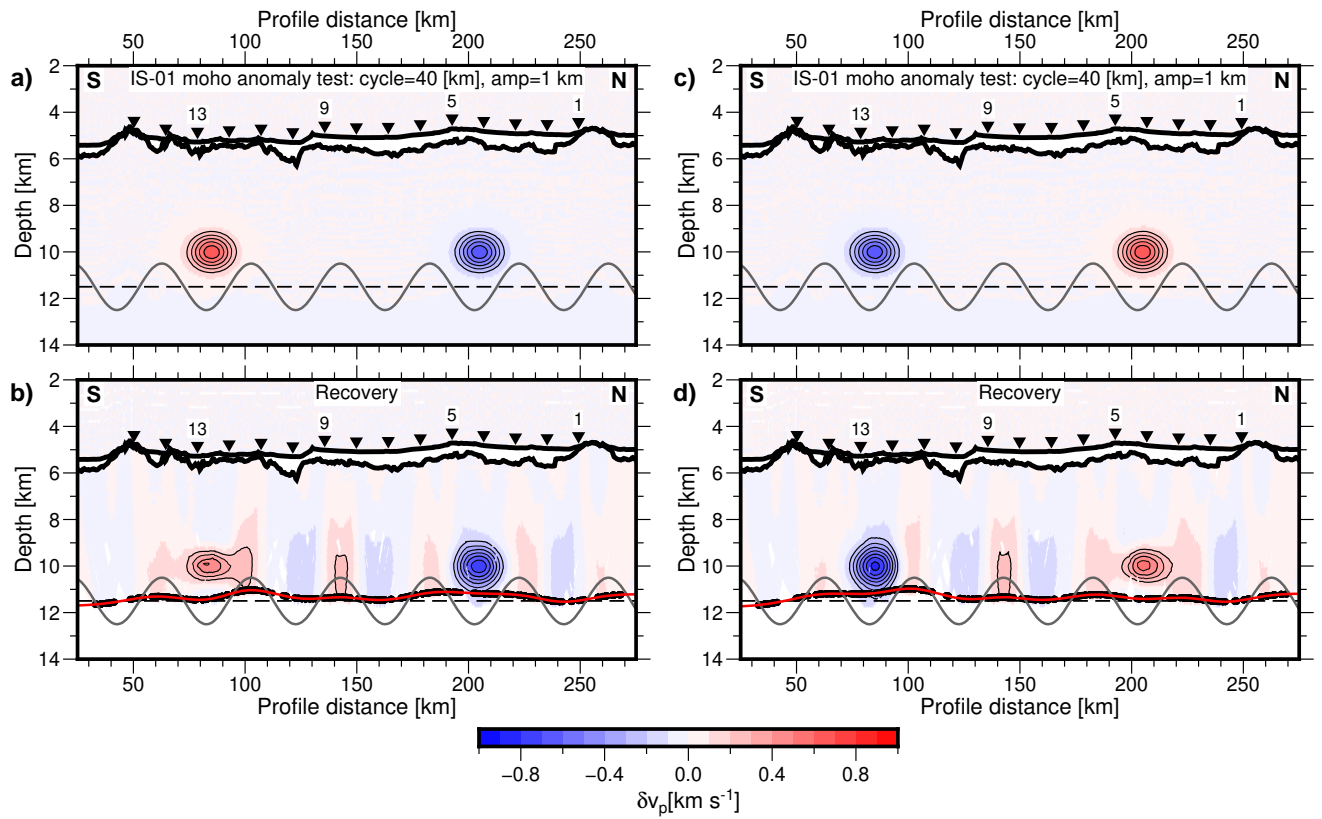
Figure S13.   Moho resolution test for IS-01: the same test as in Fig. S11 but with a reduced reflector perturbation cycle length of 40 km.
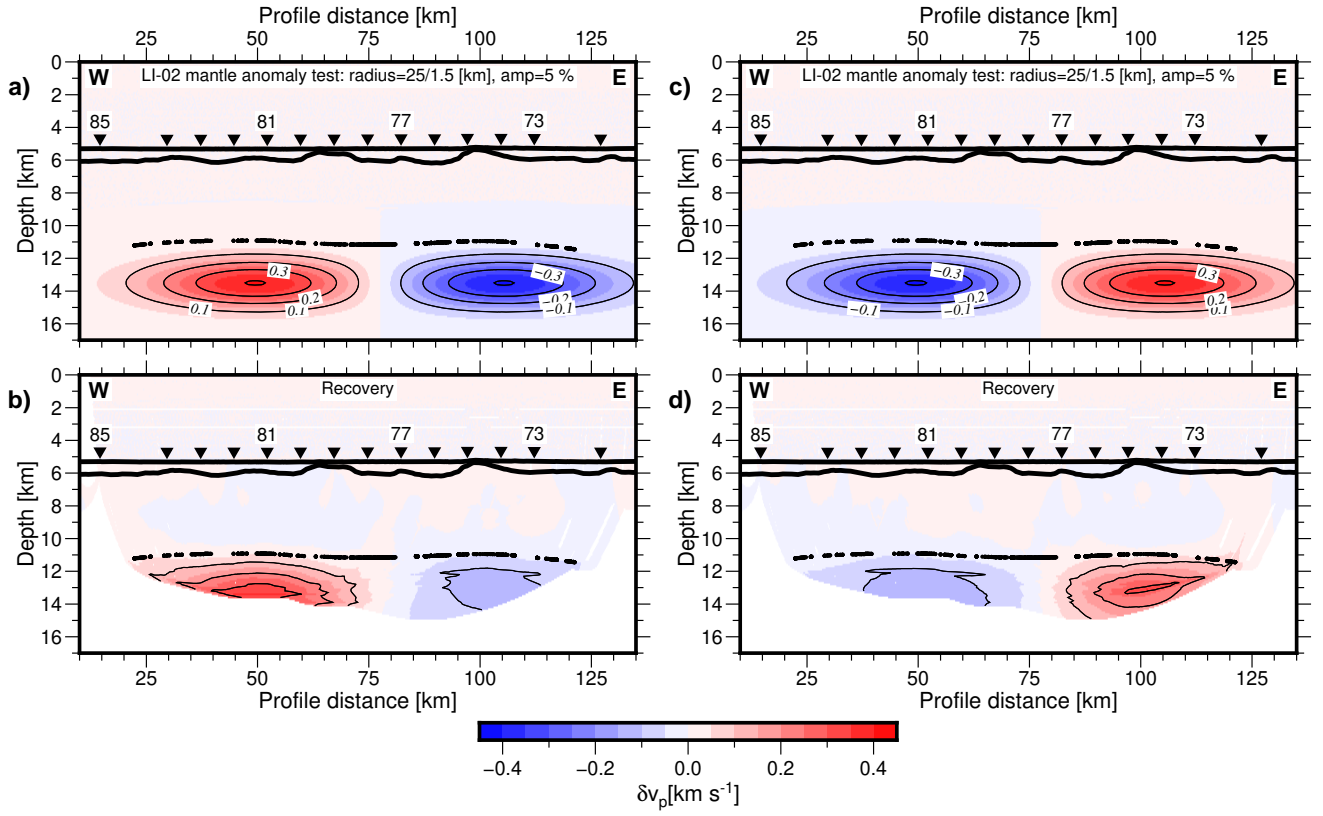
Figure S14. LI-02: mantle anomaly test for gaussian anomaly pattern with horizontal radius of 25 km, a vertical radius of 1.5 km and a perturbation amplitude of 5 %. Panels (c,d) show the same test with reversed polarity of (a,b) The contour interval is 0.1 km/s.
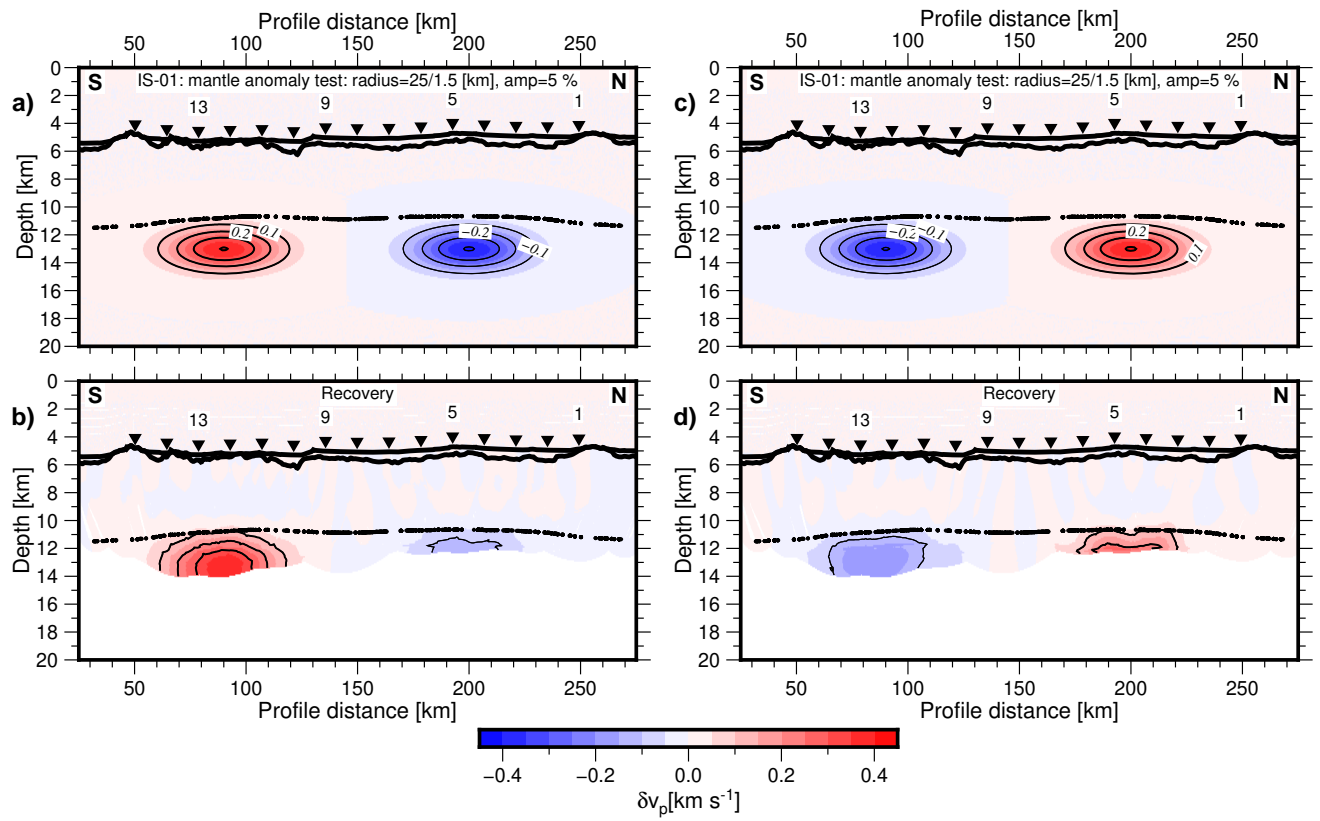
Figure S15. Mantle anomaly test for IS-01: the same testing procedure and figure elements as in Figure S14.

:

Table S2. Discretization, forward and inversion parameters used for the tomographic inversion with TOMO2D.

Parameter / Line	LI-02	IS-01
Discretizing		
profile length [km]	145	350
model depth [km]	20	20
horizontal velocity node spacing [km]	0.2	0.3
vertical velocity node spacing [km]	0.05 – 0.25, increasing with depth	
number of velocity nodes	102366	164547
horizontal reflector node spacing [km]	0.2	0.3
number of reflector nodes	726	1167
Forward modelling		
forward star	10x15	
max ray segment length [km]	1	
number of interpolation points per segment	8	
tolerance for conjugate gradient	4.00E-04	
tolerance for Brent minimization	5.00E-05	
Inversion		
horizontal correlation length for velocity [km]	1.25 – 5	1.5 – 5
vertical correlation length for velocity [km]	0.375 – 3	0.5 – 3
horizontal correlation length for reflector [km]	3	
velocity smoothing weight for Pg	30	30
velocity damping weight for Pg	30	30
velocity smoothing weight for Pg+PmP	50	70
velocity damping weight for Pg+PmP	50	50
reflector depth smoothing weight	50	70
reflector depth damping weight	50	50
depth kernel weighting factor	1	
velocity smoothing weight for Pg+PmP+Pn	100	100
velocity damping weight for Pg+PmP+Pn	500	300
max iteration Pg1	8	
max iteration Pg2	8	
max iteration Pg3	8	
max iteration PmP	8	
max iteration Pn	5	
target $\chi 2$	1.2	
tolerance for LSQR sparse matrix solver	3.00E-03	
number of initial models for MCA	100	
mean initial crustal thickness [km]	6	
velocity input standard deviation [km/s]	0.3 – 0.5	
Moho input standard deviation [km]	0.75	

Table S3.   PmP reflector inversion parameters for strong and weak regularization. If two

values are present, the first one refers to line LI-02 and the second to line IS-01.

Parameter/Line	strong Reg.	weak Reg.
Reflector correlation length [km]	3	1.25
Reflector smoothing weight	50, 70	15
Reflector damping weight	50	10
χ^2_{pmp}	0.9, 1.0	0.5, 0.5